

University of California  
Santa Barbara

**Search for new physics and production of four top  
quarks with final states containing a same-sign  
dilepton pair at a center-of-mass energy of 13 TeV  
with the CMS detector**

A dissertation submitted in partial satisfaction  
of the requirements for the degree

Doctor of Philosophy  
in  
Physics

by

Nick Amin

Committee in charge:

Professor Claudio Campagnari, Chair  
Professor David Stuart  
Professor Nathaniel Craig

September 2020

The Dissertation of Nick Amin is approved.

---

Professor David Stuart

---

Professor Nathaniel Craig

---

Professor Claudio Campagnari, Committee Chair

September 2020

Search for new physics and production of four top quarks with final states containing a same-sign dilepton pair at a center-of-mass energy of 13 TeV with the CMS detector

Copyright © 2020

by

Nick Amin

## **Acknowledgements**

I would like to acknowledge and thank my advisor, Claudio Campagnari, as well as friends, family, and colleagues. I would also like to thank the Vim text editor.

# Curriculum Vitæ

Nick Amin

## Education

2020	Ph.D. in Physics (Expected), University of California, Santa Barbara.
2017	M.Sc. in Physics, University of California, Santa Barbara.
2014	B.Sc. in Physics, Texas A&M University, College Station, TX.

## Publications

- B. Hashemi, N. Amin, K. Datta, D. Olivito, and M. Pierini, *LHC analysis-specific datasets with Generative Adversarial Networks* [arXiv:1901.0528]
- CMS Collaboration, *Search for standard model production of four top quarks in final states with same-sign and multiple leptons in proton-proton collisions at  $\sqrt{s} = 13$  TeV* *Eur. Phys. J.* **C80** (2020) [arXiv:1908.06463]
- CMS Collaboration, *Search for physics beyond the standard model in events with two same-sign leptons or at least three leptons and jets in proton-proton collisions at  $\sqrt{s} = 13$  TeV* *Eur. Phys. J.* **C80** (2020) [arXiv:2001.10086]
- CMS Collaboration, *Search for standard model production of four top quarks with same-sign and multilepton final states in proton-proton collisions at  $\sqrt{s} = 13$  TeV*, *Eur. Phys. J.* **C78** (2018) [arXiv:1710.10614]
- CMS Collaboration, *Search for physics beyond the standard model in events with two leptons of same sign, missing transverse momentum, and jets in proton-proton collisions at  $\sqrt{s} = 13$  TeV* *Eur. Phys. J.* **C77** (2017) [arXiv:1704.07323]

## Abstract

Search for new physics and production of four top quarks with final states containing a same-sign dilepton pair at a center-of-mass energy of 13 TeV with the CMS detector

by

Nick Amin

Two related searches for Standard Model and inclusive beyond the Standard Model physics with a final state containing a pair of same-charged leptons and jets are performed using a sample of  $\sqrt{s} = 13$  TeV data corresponding to an integrated luminosity of  $137 \text{ fb}^{-1}$ , collected by the CMS detector between 2016 and 2018. The inclusive search observes no excess above the Standard Model and thus places constraints on supersymmetric models with pair production of gluinos and squarks. Gluino masses are excluded up to 2.1 TeV, while top and bottom squarks are excluded up to 0.9 TeV. The Standard Model search measures the cross-section of the production of four top quarks using both cut-based and multivariate approaches. The observed (expected) significance of the multivariate approach is 2.6 (2.7) standard deviations, with a measured cross-section of  $12.6_{-5.2}^{+5.8} \text{ fb}$ , consistent with the Standard Model prediction of  $12.0_{-2.5}^{+2.2} \text{ fb}$ . These results are translated into constraints on the Yukawa coupling of the top quark, heavy scalar or pseudoscalar production in a type II 2HDM scenario or models of dark matter, couplings between the top quark and new light particles, and the Higgs boson oblique parameter.

# Contents

<b>Curriculum Vitae</b>	<b>v</b>
<b>Abstract</b>	<b>vi</b>
<b>1 Introduction</b>	<b>1</b>
1.1 Standard model . . . . .	1
1.2 Beyond the standard model . . . . .	2
1.3 Large Hadron Collider . . . . .	4
1.4 Compact Muon Solenoid . . . . .	6
1.4.1 Tracker . . . . .	7
1.4.2 Electromagnetic calorimeter . . . . .	8
1.4.3 Hadronic calorimeter . . . . .	8
1.4.4 Muon system . . . . .	9
1.4.5 Trigger and reconstruction . . . . .	10
<b>2 Same-sign dilepton final state</b>	<b>13</b>
2.1 SUSY processes . . . . .	15
2.2 Contributions to $t\bar{t}t\bar{t}$ production . . . . .	22
2.2.1 On-shell . . . . .	23
2.2.1.1 Two Higgs doublet models . . . . .	23
2.2.1.2 Simplified dark matter models . . . . .	28
2.2.2 Off-shell . . . . .	32
2.2.2.1 Top quark yukawa coupling . . . . .	32
2.2.2.2 Light off-shell mediators . . . . .	35
2.2.2.3 Oblique Higgs parameter . . . . .	37
<b>3 Objects and selections</b>	<b>40</b>
3.1 Jets, MET . . . . .	40
3.1.1 Jets . . . . .	40
3.1.2 B-tagging . . . . .	42
3.1.3 MET . . . . .	43

3.2	Leptons . . . . .	43
3.2.1	Identification . . . . .	43
3.2.2	Isolation . . . . .	46
3.3	Other variables . . . . .	48
3.4	Trigger . . . . .	49
3.5	Baseline selections . . . . .	55
3.6	Event-level BDT . . . . .	56
3.7	Signal regions . . . . .	59
3.7.1	SUSY analysis . . . . .	59
3.7.2	SM $t\bar{t}t\bar{t}$ analysis . . . . .	64
<b>4</b>	<b>Background estimation</b>	<b>66</b>
4.1	Prompt SM . . . . .	68
4.2	Nonprompt leptons . . . . .	71
4.3	Charge misidentification . . . . .	82
4.4	Corrections . . . . .	86
4.4.1	Gluon splitting . . . . .	86
4.4.2	ISR/FSR jet multiplicity . . . . .	87
4.5	Control regions . . . . .	90
4.5.1	SUSY: OS events . . . . .	90
4.5.2	SUSY: SS tight-loose events . . . . .	93
4.5.3	SUSY: Low $p_T^{\text{miss}}$ on-Z multi-lepton events . . . . .	96
4.5.4	SUSY: Low $p_T^{\text{miss}}$ SS events . . . . .	97
4.5.5	SM $t\bar{t}t\bar{t}$ : OS events . . . . .	99
4.5.6	SM $t\bar{t}t\bar{t}$ : SS tight-loose events . . . . .	102
4.5.7	SM $t\bar{t}t\bar{t}$ : Fake-enriched events . . . . .	105
4.6	Systematic uncertainties . . . . .	107
<b>5</b>	<b>Results and interpretations</b>	<b>110</b>
5.1	SUSY results . . . . .	110
5.2	SUSY interpretations . . . . .	116
5.2.1	Model-dependent . . . . .	116
5.2.2	Model-independent . . . . .	125
5.3	SM $t\bar{t}t\bar{t}$ results . . . . .	127
5.4	SM $t\bar{t}t\bar{t}$ interpretations . . . . .	134
5.4.1	Top quark yukawa coupling . . . . .	134
5.4.2	Oblique Higgs parameter . . . . .	137
5.4.3	Off-shell particles . . . . .	137
5.4.4	On-shell particles . . . . .	139
<b>6</b>	<b>Summary and conclusions</b>	<b>143</b>

<b>A Statistics</b>	<b>146</b>
A.1 Profile likelihood . . . . .	146
A.1.1 Terminology . . . . .	146
A.1.2 Toy example . . . . .	147
A.1.3 Upper limits . . . . .	154
<b>Bibliography</b>	<b>156</b>

# Chapter 1

## Introduction

### 1.1 Standard model

The Standard Model (SM) of particle physics is a quantum field theory that describes fundamental particles and most of their interactions [1, 2, 3]. Elementary matter particles in the SM have half-integer spin (fermions) and particles responsible for interactions (force-mediators) have integer spin (bosons).

As shown in Figure 1.1, SM matter particles are either quarks (up, down, charm, strange, top, and bottom) or leptons (electron, muon, tau, and three corresponding neutrinos). Together, the massless photon, the massive charged W bosons, and the massive neutral Z boson mediate electroweak interactions. Massless gluons mediate the strong force. Fermions acquire mass through their interaction with the field associated with the recently-discovered [4, 5] Higgs boson. The SM does not have a mechanism to

account for the gravitational force.

mass → charge → spin →	$\approx 2.3 \text{ MeV}/c^2$ 2/3 1/2 up	$\approx 1.275 \text{ GeV}/c^2$ 2/3 1/2 charm	$\approx 173.07 \text{ GeV}/c^2$ 2/3 1/2 top	0 0 1 gluon	$\approx 126 \text{ GeV}/c^2$ 0 0 0 Higgs boson
<b>QUARKS</b>	<b>u</b>	<b>c</b>	<b>t</b>	<b>g</b>	<b>H</b>
$\approx 4.8 \text{ MeV}/c^2$ -1/3 1/2 down	$\approx 95 \text{ MeV}/c^2$ -1/3 1/2 strange	$\approx 4.18 \text{ GeV}/c^2$ -1/3 1/2 bottom	$\gamma$		
<b>d</b>	<b>s</b>	<b>b</b>	<b>photon</b>		
$0.511 \text{ MeV}/c^2$ -1 1/2 electron	$105.7 \text{ MeV}/c^2$ -1 1/2 muon	$1.777 \text{ GeV}/c^2$ -1 1/2 tau	$91.2 \text{ GeV}/c^2$ 0 1 Z boson		
<b>e</b>	<b><math>\mu</math></b>	<b><math>\tau</math></b>	<b>Z boson</b>		
$<2.2 \text{ eV}/c^2$ 0 1/2 electron neutrino	$<0.17 \text{ MeV}/c^2$ 0 1/2 muon neutrino	$<15.5 \text{ MeV}/c^2$ 0 1/2 tau neutrino	$80.4 \text{ GeV}/c^2$ $\pm 1$ 1 W boson		
<b><math>\nu_e</math></b>	<b><math>\nu_\mu</math></b>	<b><math>\nu_\tau</math></b>	<b>W boson</b>		
				<b>GAUGE BOSONS</b>	

Figure 1.1: Summary table of SM particles and their properties. Image taken from [6].

Many testable predictions of the SM have been overwhelmingly validated over the past half century, making the SM a very successful theory. However, in addition to not accounting for gravity, there are a number of compelling reasons to say that the SM is not a complete theory.

## 1.2 Beyond the standard model

There is variety of evidence that point to beyond the SM (BSM) physics. A notable few concern dark matter, neutrino masses, and the Higgs boson mass.

*Dark matter*

Astronomical observations of velocity of objects around galactic centers have shown a clear deviation[7] from predictions that assume gravitational effects only arose from matter that we can see. This is clear evidence for the existence of “dark” matter (DM) which we cannot directly observe. In fact, about 85% of the mass in the universe is dark [8]. Furthermore, DM explains observed galactic formation and structure as well as gravitational lensing effects [9].

*Neutrino masses*

The current formulation of the SM does not account for neutrino masses, yet oscillations between neutrino flavors have been observed [10], which implies non-zero, albeit very small, neutrino masses.

*Higgs boson mass*

Because the SM does not incorporate quantum gravity, there is an energy (or equivalently, length) scale cutoff above which we do not expect the SM to hold. Such a cutoff, given by the Planck mass, is on the order of  $10^{19}$  GeV, approximately  $10^{17}$  times larger than the electroweak scale. We would then expect the Higgs boson mass, which receives loop corrections from massive particles, to be on the order of the Planck scale. However, the Higgs boson was observed to have a mass of 125 GeV. While inelegant, this is not inherently impossible as parameters in the theory could be “fine-tuned” to have very

large cancellations and result in a light Higgs boson mass. The fine-tuning of the Higgs mass could point toward a new symmetry in the SM.

One popular possible solution to problems with the SM is the theory of Supersymmetry (SUSY), which posits there is a symmetry between fermions and bosons: each SM particle has a corresponding superpartner with spin differing by 1/2 (fermions  $\leftrightarrow$  bosons) [11]. This must not be a perfect symmetry, otherwise we would have observed partner particles with the same mass for the currently known SM particles. These additional SUSY partner particles help to cancel out corrections to the Higgs boson mass, alleviating the issue of fine-tuning (provided the masses of the superpartners are not too much larger than the SM counterparts).

SUSY theories can be chosen to be R-parity conserving [12]. That is, if  $(-1)^R = (-1)^{3B+L+2s}$  where  $B$  is baryon number,  $L$  is lepton number, and  $s$  is spin, then SM particles have  $R = 1$  while SUSY superpartners have  $R = -1$ . For conservation of R-parity, there must be a lightest SUSY particle (LSP) which cannot decay into two SM particles. This stable LSP is an ideal candidate for DM if it is electrically neutral.

### 1.3 Large Hadron Collider

We now turn to a massive machine whose design goal was to discover the Higgs boson and to look for hints of (or, hopefully, discover) BSM physics at TeV-scale energies.

This machine, the Large Hadron Collider (LHC) [13], is the largest and highest-energy

particle collider in the world. Built by the European Organization for Nuclear Research (CERN) through an international collaboration involving over a hundred countries, it first started operation in 2008 after a decade of construction. The collider resides in a tunnel with a 27-kilometer circumference, around 100 meters below ground, and straddles the border of France and Switzerland, near Geneva. With the help of smaller particle accelerators situated near the LHC ring, the LHC accelerates two opposing beams of protons to energies of 6.5 TeV per beam and collides them by magnetically steering the beams to cross at specified points around the ring. Large detectors are built around these specified point to analyze the high energy collision products.

Proton bunches with billions of protons each are injected into the LHC ring and spaced apart such that bunch crossings happen up to a rate of 40 MHz. The billions of proton-proton collisions delivered by the LHC per second allow for many physics processes to take place. The simple formula  $N = \sigma \cdot L_{\text{int}}$ , gives the number of events/occurrences  $N$  of a physics process with cross-section  $\sigma$  (roughly a measure of the quantum mechanical probability of occurrence) in a sample of collision data with integrated luminosity  $L_{\text{int}}$ . The instantaneous luminosity of LHC beams is on the order of  $10^{34} \text{ cm}^{-2} \text{ s}^{-1}$ . A barn (b), the metric unit for area, is commonly used to express cross sections and luminosities, and is equivalent to  $10^{-24} \text{ cm}^2$ . Thus, the LHC instantaneous luminosity can be roughly written as  $1 \text{ fb}^{-1} \text{ day}^{-1}$ . So, a potential new physics process with a cross-section of 1 fb could manifest itself as an event in a day of collected data. That needle would need to be found in the haystack of other more mundane processes. Due to the many protons

per bunch, we expect about 30 proton-proton interaction events per crossing (pileup interactions) to disentangle from exotic signals.

## 1.4 Compact Muon Solenoid

The Compact Muon Solenoid (CMS) detector [14, 15] is one of the general purpose detectors situated on the LHC ring at an interaction/collision point. The CMS detector is 21 meters long and 15 meters tall. Its primary feature is a 3.8 Tesla solenoidal magnet creating a magnetic field oriented along the proton beamline, which causes the trajectories of charged particles to bend in the plane perpendicular to the beamline. The detector uses layered tracking sensors and calorimeters to reconstruct the positions and momenta of particles.

The CMS coordinate system is centered on the central collision point. The x-axis points radially inward toward the center of the LHC, the y-axis points vertically upward, and the z-axis points along the beamline with the positive direction facing the west. The azimuthal angle  $\phi$  around the cylindrical axis of the detector is measured with respect to the LHC plane. The polar angle  $\theta$  is measured with respect to the z-axis; however, a transformation of the polar angle, the pseudorapidity  $\eta \equiv -\ln(\tan(\theta/2))$  is more commonly used to refer to polar angles. The transverse momentum ( $p_T$ ) of particles is measured in the x-y plane.

Let us now turn to the individual subsystems that comprise the CMS detector starting from the center, working our way radially outward. A cutaway view of the CMS detector,

highlighting these subsystems, is shown in Figure 1.2.

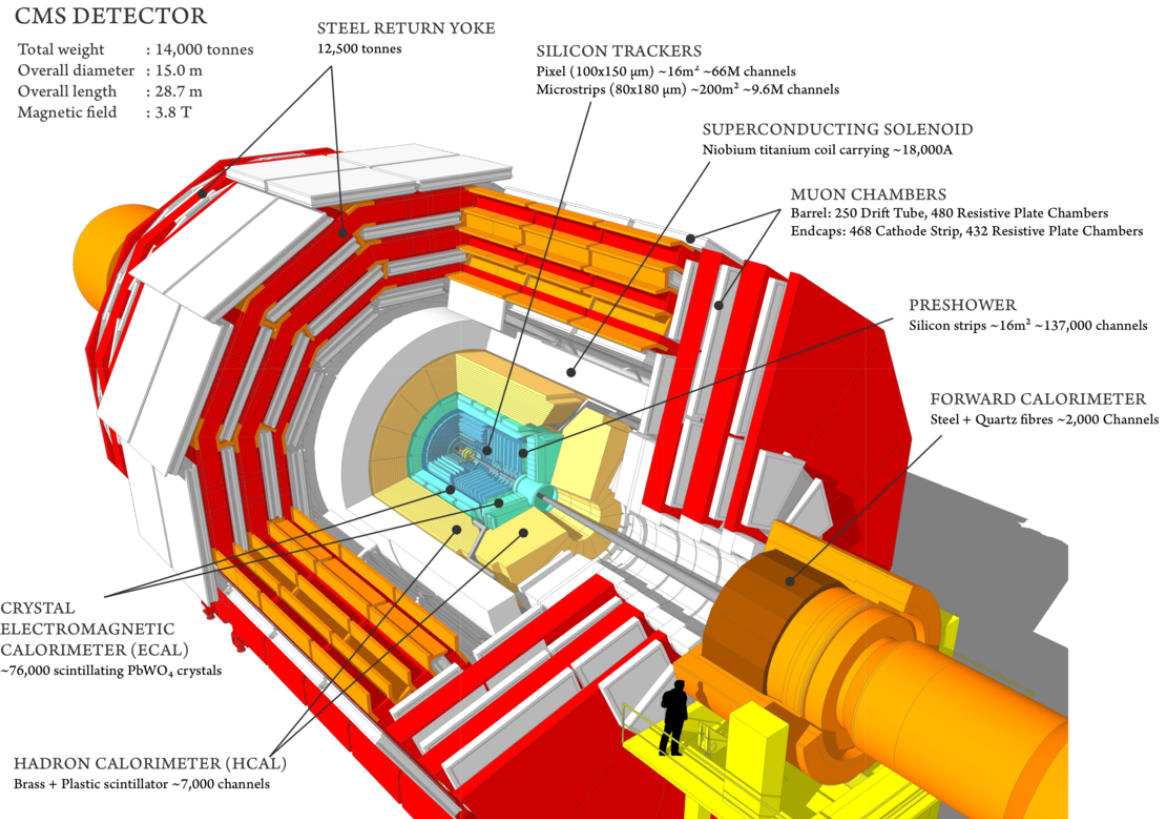


Figure 1.2: A cutaway view of the CMS detector.

### 1.4.1 Tracker

The innermost subdetector is the tracker [16, 17], which is composed of an inner pixel detector and an outer strip tracker. Both use silicon technology which allows for the formation of electron-hole pairs when a charged particle passes through. There are 3 layers of inner pixel detectors with a transverse radial position ranging between 4.4 cm and 10.2 cm. In 2017, these were replaced with 4 layers ranging between 3.0 cm and 16.0 cm. The outer strip tracker consists of 10 layers in the central barrel region, extending out

to 1.1 m. The endcaps consist of 2 disks for the inner pixel detector and 12 disks in the strip tracker.

The tracker allows for precise reconstruction of particle trajectories and vertexing up to  $|\eta| = 2.5$  and for full range of azimuthal angles.

### 1.4.2 Electromagnetic calorimeter

Sitting just outside of the tracker is the electromagnetic calorimeter (ECAL). The ECAL is composed of nearly 80,000 lead tungstate scintillating crystals tiled to form a cylinder, and is split into a barrel section and two endcap sections [18]. Together, these sections provide full azimuthal coverage and coverage up to  $|\eta| = 3.0$ .

The high-density lead tungstate crystals, which are 22 cm in depth and point toward the center of the CMS detector, have a radiation length of 0.85 cm. Consequently, the 25 radiation lengths in each crystal allow electromagnetic showers to be almost completely longitudinally contained within the single layer of crystals. The small Moli  re radius of the electromagnetic showers (2.2 cm), which coincides with the width of the crystals themselves (2.2 cm in the barrel and 2.9 cm in the endcaps), ensures that the transverse profile of showers is mostly contained within just a single crystal.

### 1.4.3 Hadronic calorimeter

Outside of the ECAL is the hadronic calorimeter (HCAL) [15], which is split into four sets of calorimeters to cover different geometrical regions: barrel (HB), endcap

(HE), outer (HO), and forward (HF) calorimeters. Similar to the ECAL, the first three sections collectively coverage of hadronic showers up to  $|\eta| = 3.0$ , and the HF extends the coverage to  $|\eta| = 5.0$ .

The sampling calorimeters of the HCAL are made of alternating layers of absorber (brass or steel) that induce hadronic showers, and plastic scintillators. In the barrel, the brass absorbers have a total of nearly 6 interaction lengths, and along with the plastic scintillators, have transverse segmentation with  $\eta$  and  $\phi$  widths of 0.087.

#### 1.4.4 Muon system

Last, but not least, is the namesake muon system [19] outside of the calorimeters and interspersed between parts of the steel return yoke. The muon system uses three main technologies: Drift Tubes (DTs) in the barrel, Cathode Strip Chambers (CSCs) in the endcaps, and Resistive Plate Chambers (RPCs) in the barrel and endcaps. Together, the muon system covers up to  $|\eta| = 2.4$ .

The barrel DTs are arranged into four stations of concentric cylinders, and use an ionizing gas mixture of Ar/CO<sub>2</sub> and sensitive gold-plated steel wires to detect the ionization of throughgoing muons. Each DT has two or three layers with wires that are either perpendicular to the beam line (to measure the  $z$  coordinate), or parallel (to measure the  $\phi$  coordinate). Cylindrical stacking of DTs provides a measurement of the  $r$  coordinate.

The trapezoidal endcap CSCs cover trajectories at high- $|\eta|$ . Each detector is a multiwire proportional chamber with 6 anode wire planes alternated with 7 cathode strip

panels. Wires are oriented azimuthally and allow the measurement of a trajectory's  $r$  coordinate. Strips are oriented radially and precisely measure the  $\phi$  coordinate. CSCs provide a spatial resolution on the order of  $100\ \mu\text{m}$ .

While not as spatially precise as DTs and CSCs, the gas-filled parallel-plate RPC detectors provide excellent time resolution (several nanoseconds) to help tag the time/bunch crossing of muon hits.

#### 1.4.5 Trigger and reconstruction

With the extremely high rate of collisions delivered to the CMS detector by the LHC, it is not feasible to store and reconstruct collision information for every event. A trigger system provides a solution to this problem by evaluating if an event is potentially useful enough to keep. This is implemented as a two-tiered system: a Level-1 (L1) trigger and a subsequent High-Level Trigger (HLT) [20].

The L1 trigger stage uses custom hardware with FPGAs and look up tables to roughly calculate various particle momenta and positions based on information from different subdetectors as fast as possible, in order to evaluate if an event passes specific quality criteria. The L1 trigger reduces the event rate by a factor of a million, and is designed to output events at less than 100 kHz.

After an event passes the L1 trigger, it is passed through the HLT stage which is implemented in pure software and runs on a farm of computers. Events are partially reconstructed with more precision than with the L1 stage. This HLT stage reduces

the event rate to less than 1 kHz. At this point, events are passed along to be fully reconstructed and persisted at storage facilities.

CMS uses particle-flow (PF) reconstruction algorithms [21] to utilize information from all subdetectors to reconstruct particles within an event. At the lowest level, particle trajectories are reconstructed from hits in sensitive layers of detectors. Reconstruction of certain particles can then be loosely identified with different subdetectors. For example, electrons and photons are reconstructed with information from the tracker and ECAL. Charged and neutral hadrons use information from the ECAL and HCAL. Muons are reconstructed with information from the tracker and muon system. Neutrinos are not reconstructed as they pass through the detector without interacting, but their presence can be inferred from an imbalance of transverse momentum in an event.

The remaining sections of the thesis are structured as follows. Chapter 2 introduces the same-sign dilepton final state, a promising avenue to explore new and rare physics. Chapter 3 discusses analysis objects and selections for two related analyses: one is an inclusive search for BSM, focusing on a variety of SUSY signals; the second is a SM search for the production for four top quarks. Both utilize data delivered by the LHC and collected by the CMS detector from 2016–2018, totaling  $137 \text{ fb}^{-1}$ . Chapter 4 describes the SM backgrounds to these analyses. Chapter 5 presents the final results for each, and a summary with concluding remarks is given in Chapter 6. The results and techniques presented throughout this thesis correspond to the published results in Refs. [22, 23, 24,

25].

# Chapter 2

## Same-sign dilepton final state

Almost every new (or rare SM) physics analysis relies on a “killer” variable or technique to differentiate signal from background and increase the signal-to-noise ratio to a level that is conducive to further interpretation. The technique used in this thesis exploits the fact that seeing a pair of leptons with the same charge as a product of proton-proton collision processes (e.g.,  $W/Z$  production, QCD) is very, very rare, but is quite common in scenarios of new (or rare SM) physics.

We start by examining the rare production of four top quarks ( $t\bar{t}t\bar{t}$ ) in the SM, as SUSY processes follow similar patterns and will be discussed in more detail in the subsequent section. The four top quarks of SM  $t\bar{t}t\bar{t}$  will each decay into a b quark and W boson. A W boson decays into a charged lepton and matching neutrino ( $e\bar{\nu}_e$ ,  $\mu\bar{\nu}_\mu$ ,  $\tau\bar{\nu}_\tau$ ) with approximately 1/3 probability. For four W bosons ( $W^+W^+W^-W^-$ ), the lepton multiplicities and characteristics are summarized in Fig 2.1. Up to 12% of SM  $t\bar{t}t\bar{t}$  can be

selected by requiring a same-sign (SS) dilepton ( $e$  or  $\mu$ ) in the final state, which includes the leptonic branching ratio of  $\tau$  to  $e$  or  $\mu$ .

Turning to background SM processes, to first order, requiring two leptons (SS or not) directly eliminates QCD processes with only quarks/gluons (u, d, s, c, b, g) in the final state. Figure 2.2 summarizes CMS measurements of many other SM processes. Three of the highest cross section processes are  $W$ ,  $Z$ , and  $t\bar{t}$ , which give one lepton or two opposite sign leptons, and would also be eliminated by requiring SS dileptons. In fact, continuing down the mountain of processes, the first process that can give prompt SS dileptons is  $WZ$ . Thus, the SS dilepton selection is an effective “cut” that rejects processes above  $O(10)$  pb. Compared to many other search strategies, which exploit extreme event kinematics, the SS dilepton selection allows probing softer events with less transverse momenta and missing transverse energy.

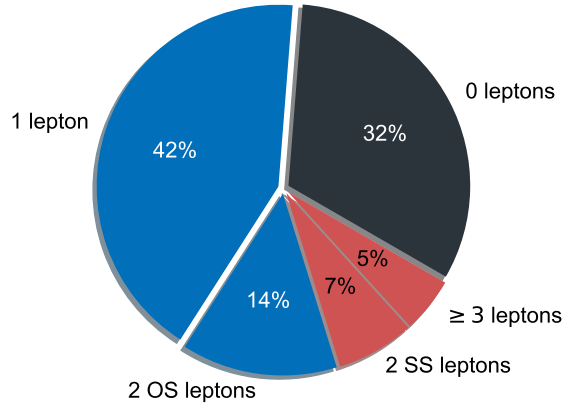


Figure 2.1: Lepton multiplicities of four  $W$  final states.

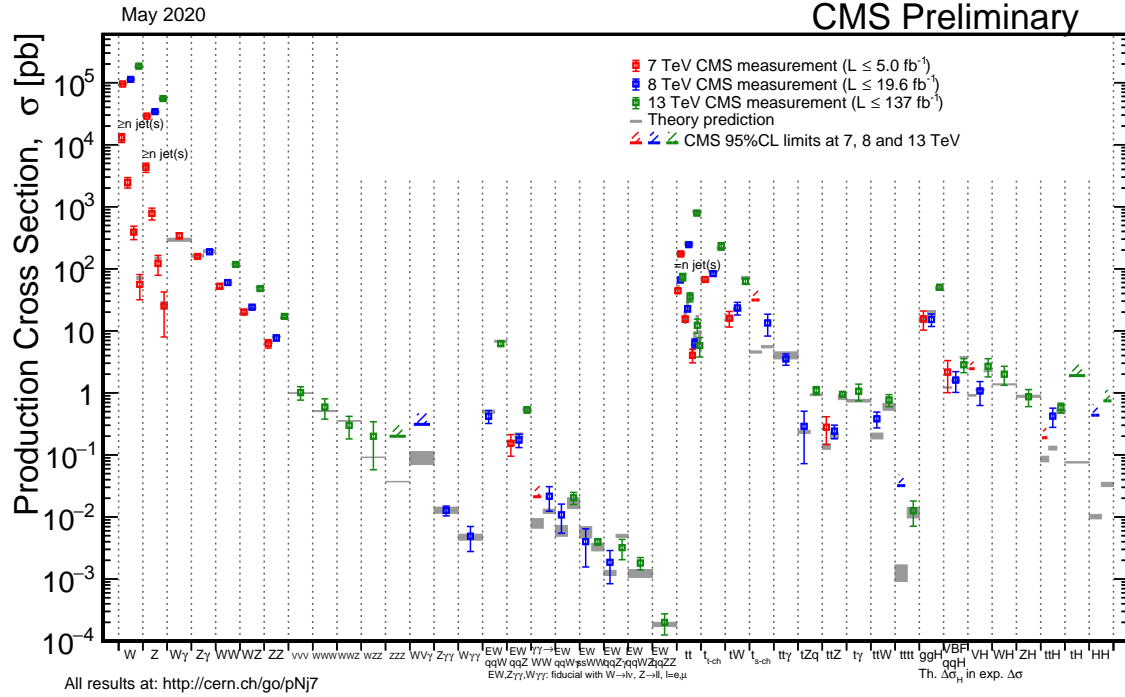


Figure 2.2: Summary of SM cross section measurements at CMS [26]. (Spoiler alert: the results presented later in this thesis correspond to one of the points in this plot!)

## 2.1 SUSY processes

Many SUSY models with strong pair production mechanisms result in final states with a number of leptons, ideal for SS final states. Here, we consider simplified models of SUSY with a reduced number of parameters [?], where signal model hypotheses are specified by a production and decay process with one or two SUSY particle masses fixed to particular masses that are “scanned” over. Cross sections of pair production models with gluinos and squarks are shown in Fig. 2.3, and are as low as a few  $\text{fb}^{-1}$  for gluino/squark masses between 1.5 TeV and 2 TeV.

Gluino pair production models giving rise to signatures with up to four b quarks and W bosons are shown in Fig. 2.4. In these models, the gluino decays to the lightest squark

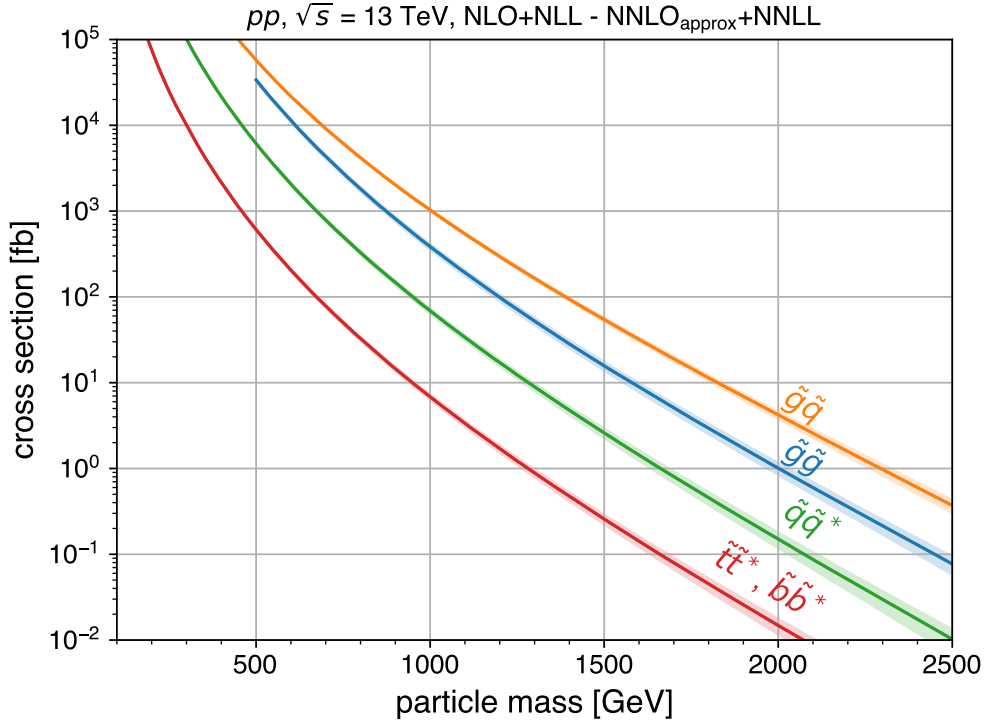


Figure 2.3: Strong production cross sections for SUSY processes at the LHC. Calculations from [27].

$(\tilde{g} \rightarrow \tilde{q}\tilde{q})$ , which then decays to same-flavor ( $\tilde{q} \rightarrow q\tilde{\chi}_1^0$ ) or different-flavor ( $\tilde{q} \rightarrow q'\tilde{\chi}_1^\pm$ ) quarks. The chargino ( $\tilde{\chi}_1^\pm$ ) decays to a W boson and a neutralino ( $\tilde{\chi}_1^0$ ) via  $\tilde{\chi}_1^\pm \rightarrow W^\pm \tilde{\chi}_1^0$ , where the  $\tilde{\chi}_1^0$  is taken to be the lightest stable SUSY (LSP) particle and is not directly detectable.

The first scenario, displayed in Fig. 2.4a and denoted T1tttt, includes an off-shell top squark ( $\tilde{t}$ ) leading to a three-body decay of the gluino,  $\tilde{g} \rightarrow t\bar{t}\tilde{\chi}_1^0$ , and resulting in events with four W bosons and four b quarks. This topology is thus similar to SM  $t\bar{t}t\bar{t}$  with the addition of missing energy from the invisible LSP. Figure 2.4b presents a similar model (T5ttbbWW) but where the gluino decay results in a chargino that decays into a

neutralino and a W boson. The model shown in Fig. 2.4c (T5tttt) is identical to T1tttt except that the intermediate top squark is on-shell. The mass splitting between the  $\tilde{t}$  and the  $\tilde{\chi}_1^0$  is taken to be  $m_{\tilde{t}} - m_{\tilde{\chi}_1^0} = m_t$ , where  $m_t$  is the top quark mass. This mass splitting corresponds to a challenging region of parameter space for the observation of the  $\tilde{t} \rightarrow t\tilde{\chi}_1^0$  decay. The model of Fig. 2.4d (T5ttcc) is identical to T5tttt except that the  $\tilde{t}$  decay involves a c quark. In Fig. 2.4e, the process includes a virtual light-flavor squark, leading to three-body decays of  $\tilde{g} \rightarrow qq'\tilde{\chi}_1^\pm$  or  $\tilde{g} \rightarrow qq'\tilde{\chi}_2^0$ , with a resulting signature of two W bosons, two Z bosons, or one of each (the case shown in Fig. 2.4e), and four light-flavor jets. This model, T5qqqqWZ, with a resulting signature of one W boson and one Z boson, is considered separately for two different assumptions of the chargino mass,  $m_{\tilde{\chi}_1^\pm} = 0.5(m_{\tilde{g}} + m_{\tilde{\chi}_1^0})$ , and  $m_{\tilde{\chi}_1^\pm} = m_{\tilde{\chi}_1^0} + 20\text{GeV}$ , producing on- and off-shell bosons, respectively. The model is also considered with the assumption of decays to two W bosons (T5qqqqWW).

Figure 2.5a shows a model of bottom squark production and decay via  $\tilde{b}_1 \rightarrow t\tilde{\chi}_1^\pm$ , giving two b quarks and four W bosons. This model, T6ttWW, is considered as a function of the the lightest bottom squark,  $\tilde{b}_1$ , and  $\tilde{\chi}_1^\pm$  masses. The  $\tilde{\chi}_1^0$  mass is fixed at 50 GeV, which results in two off-shell W bosons when the  $\tilde{\chi}_1^\pm$  mass is less than approximately 130 GeV. Figure 2.5b displays the T6ttHZ model with top squark pair production and a subsequent decay of  $\tilde{t}_2 \rightarrow \tilde{t}_1 H/Z$ , with  $\tilde{t}_1 \rightarrow t\tilde{\chi}_1^0$ , producing signatures with two H bosons, two Z bosons, or one of each. In this model the  $\tilde{\chi}_1^0$  mass is fixed such that  $m(\tilde{t}_1) - m(\tilde{\chi}_1^0) = m_t$ .

The R parity violating (RPV) decays considered in the SUSY analysis are T1qqqqL (Fig. 2.6a) and T1tbs (Fig. 2.6b). Unlike the previously discussed processes, these RPV processes do not have a stable LSP. In T1qqqqL, the gluino decays to the lightest squark ( $\tilde{g} \rightarrow \tilde{q}q$ ), which decays to a quark ( $\tilde{q} \rightarrow q\tilde{\chi}_1^0$ ) with an off shell  $\tilde{\chi}_1^0$  decaying into two quarks and a charged lepton, giving rise to a prompt 5-body decay of the gluino. In the T1tbs model, the gluinos each decay into three different SM quarks ( $t$ ,  $b$ , and  $s$ ).

A summary of the 14 simplified SUSY models considered in the inclusive SUSY analysis is shown in Table 2.1. The last few columns give final state multiplicities of bosons and b quarks. At a glance, based on the high multiplicity of  $W$  and  $Z$  bosons, it is clear that these models result in SS final states and many jets.

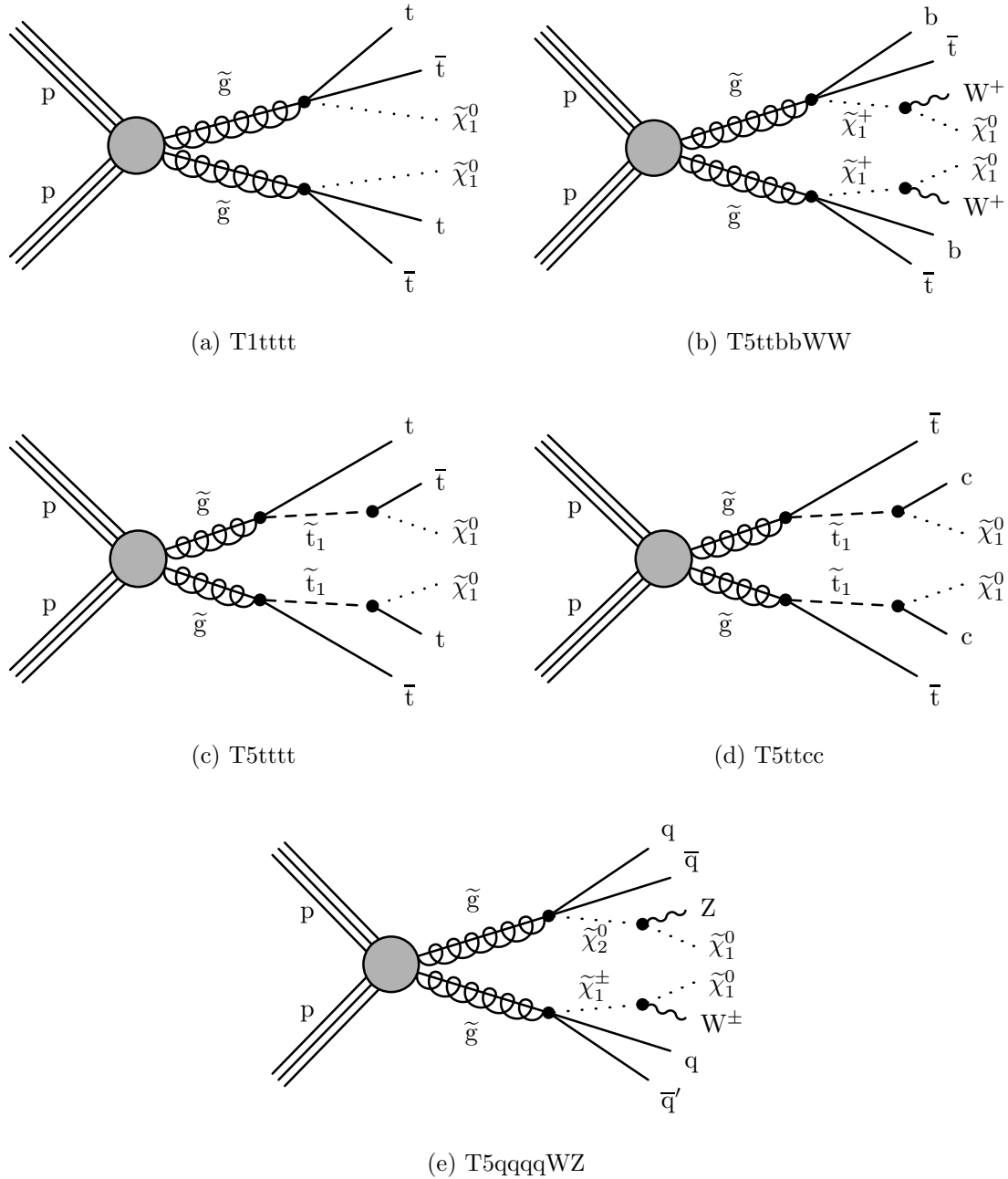


Figure 2.4: Diagrams illustrating the simplified RPC SUSY models with gluino production considered in this analysis.

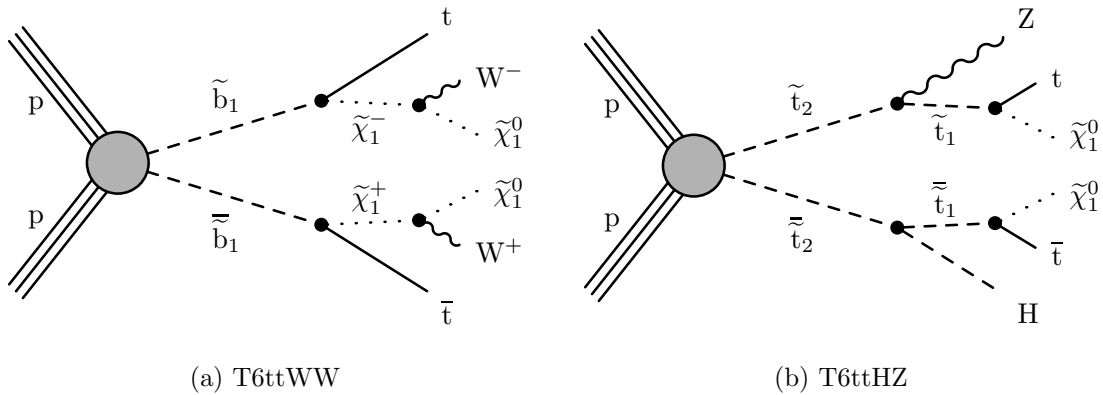


Figure 2.5: Diagrams illustrating the simplified RPC SUSY models with squark production considered in this analysis.

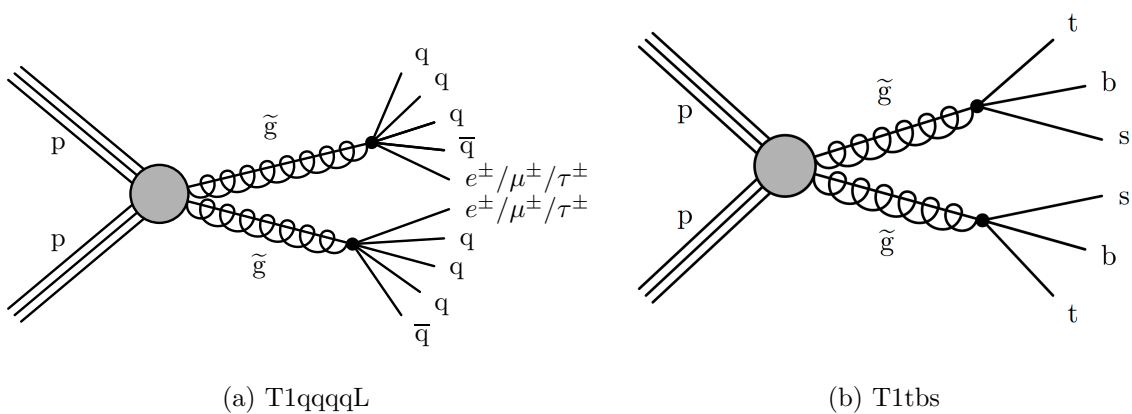


Figure 2.6: Diagrams illustrating the two simplified RPV SUSY models considered in this analysis.

Model	Process	Constraint	Mass 1	Mass 2	RPV	#W	#Z	#H	#b
T1tttt	$\tilde{g} \rightarrow t\bar{t}\tilde{\chi}_1^0$	—	$m_{\tilde{g}}$	$m_{\tilde{\chi}_1^0}$	—	4	0	0	4
T5ttbbWW	$\tilde{g} \rightarrow tb\tilde{\chi}_1^\pm$	$m_{\tilde{\chi}_1^\pm} = m_{\tilde{\chi}_1^0} + 5\text{GeV}$	$m_{\tilde{g}}$	$m_{\tilde{\chi}_1^0}$	—	4	0	0	4
T5tttt	$\tilde{g} \rightarrow \tilde{t}_1 t, \tilde{t}_1 \rightarrow t\tilde{\chi}_1^0$	$m_{\tilde{t}} - m_{\tilde{\chi}_1^0} = m_t$	$m_{\tilde{g}}$	$m_{\tilde{\chi}_1^0}$	—	4	0	0	4
T5ttcc	$\tilde{g} \rightarrow \tilde{t}_1 t, \tilde{t}_1 \rightarrow c\tilde{\chi}_1^0$	$m_{\tilde{t}} - m_{\tilde{\chi}_1^0} = 20\text{GeV}$	$m_{\tilde{g}}$	$m_{\tilde{\chi}_1^0}$	—	2	0	0	2
T5qqqqWW	$\tilde{g} \rightarrow qq'\tilde{\chi}_1^\pm, \tilde{\chi}_1^\pm \rightarrow W^\pm\tilde{\chi}_1^0$	$m_{\tilde{\chi}_1^\pm} = 0.5(m_{\tilde{g}} + m_{\tilde{\chi}_1^0})$	$m_{\tilde{g}}$	$m_{\tilde{\chi}_1^0}$	—	2	0	0	0
T5qqqqWW	$\tilde{g} \rightarrow qq'\tilde{\chi}_1^\pm, \tilde{\chi}_1^\pm \rightarrow W^\pm\tilde{\chi}_1^0$	$m_{\tilde{\chi}_1^\pm} = m_{\tilde{\chi}_1^0} + 20\text{GeV}$	$m_{\tilde{g}}$	$m_{\tilde{\chi}_1^0}$	—	2	0	0	0
T5qqqqWZ	$\tilde{g} \rightarrow qq'(\tilde{\chi}_1^\pm/\tilde{\chi}_2^0), \tilde{\chi}_1^\pm \rightarrow W^\pm\tilde{\chi}_1^0, \tilde{\chi}_2^0 \rightarrow Z\tilde{\chi}_1^0$	$m_{\tilde{\chi}_1^\pm} = 0.5(m_{\tilde{g}} + m_{\tilde{\chi}_1^0})$	$m_{\tilde{g}}$	$m_{\tilde{\chi}_1^0}$	—	1	1	0	0
T5qqqqWZ	$\tilde{g} \rightarrow qq'(\tilde{\chi}_1^\pm/\tilde{\chi}_2^0), \tilde{\chi}_1^\pm \rightarrow W^\pm\tilde{\chi}_1^0, \tilde{\chi}_2^0 \rightarrow Z\tilde{\chi}_1^0$	$m_{\tilde{\chi}_1^\pm} = m_{\tilde{\chi}_1^0} + 20\text{GeV}$	$m_{\tilde{g}}$	$m_{\tilde{\chi}_1^0}$	—	1	1	0	0
T6ttWW	$\tilde{b}_1 \rightarrow t\tilde{\chi}_1^\pm$	$m_{\tilde{\chi}_1^0} = 50\text{GeV}$	$m_{\tilde{b}_1}$	$m_{\tilde{\chi}_1^\pm}$	—	4	0	0	2
T6ttHZ	$\tilde{t}_2 \rightarrow \tilde{t}_1 H, \tilde{t}_1 \rightarrow t\tilde{\chi}_1^0$	$m_{\tilde{t}_1} - m_{\tilde{\chi}_1^0} = 175\text{GeV}$	$m_{\tilde{t}_2}$	$m_{\tilde{t}_1}$	—	0	0	2	2
T6ttHZ	$\tilde{t}_2 \rightarrow \tilde{t}_1(H/Z), \tilde{t}_1 \rightarrow t\tilde{\chi}_1^0$	$m_{\tilde{t}_1} - m_{\tilde{\chi}_1^0} = 175\text{GeV}$	$m_{\tilde{t}_2}$	$m_{\tilde{t}_1}$	—	0	1	2	4
T6ttHZ	$\tilde{t}_2 \rightarrow \tilde{t}_1 Z, \tilde{t}_1 \rightarrow t\tilde{\chi}_1^0$	$m_{\tilde{t}_1} - m_{\tilde{\chi}_1^0} = 175\text{GeV}$	$m_{\tilde{t}_2}$	$m_{\tilde{t}_1}$	—	0	2	0	2
T1qqqqL	$\tilde{g} \rightarrow qq\bar{q}\bar{q} + e/\mu/\tau$	—	$m_{\tilde{g}}$	—	Yes	0	0	0	0
T1tbs	$\tilde{g} \rightarrow tbs$	—	$m_{\tilde{g}}$	—	Yes	2	0	0	4

Table 2.1: Summary of simplified SUSY models considered in this thesis. The fourth and fifth columns give the one or two masses which are scanned over for simplified interpretations. The sixth column marks processes with R parity violation. The remaining columns give the final state multiplicities of  $W$ ,  $Z$ , and Higgs bosons, and b quarks, respectively.

## 2.2 Contributions to $t\bar{t}t\bar{t}$ production

SM  $t\bar{t}t\bar{t}$  production has a next-to-leading-order (NLO) cross section of  $\sigma(pp \rightarrow t\bar{t}t\bar{t}) = 12.0^{+2.2}_{-2.5}$  fb at 13 TeV, calculated in Ref. [28], with representative leading-order Feynman diagrams shown in Fig. 2.7. While it is interesting in its own right to measure a rare SM process, searching for SM  $t\bar{t}t\bar{t}$  could provide hints of BSM physics. Contributions from BSM physics to  $t\bar{t}t\bar{t}$  production at CMS can be broadly categorized as on-shell (usually involving heavy BSM intermediate particles coupling to  $t\bar{t}$ ), or off-shell (usually involving light BSM intermediate particles, or modifications to the SM Higgs boson propagator or couplings).

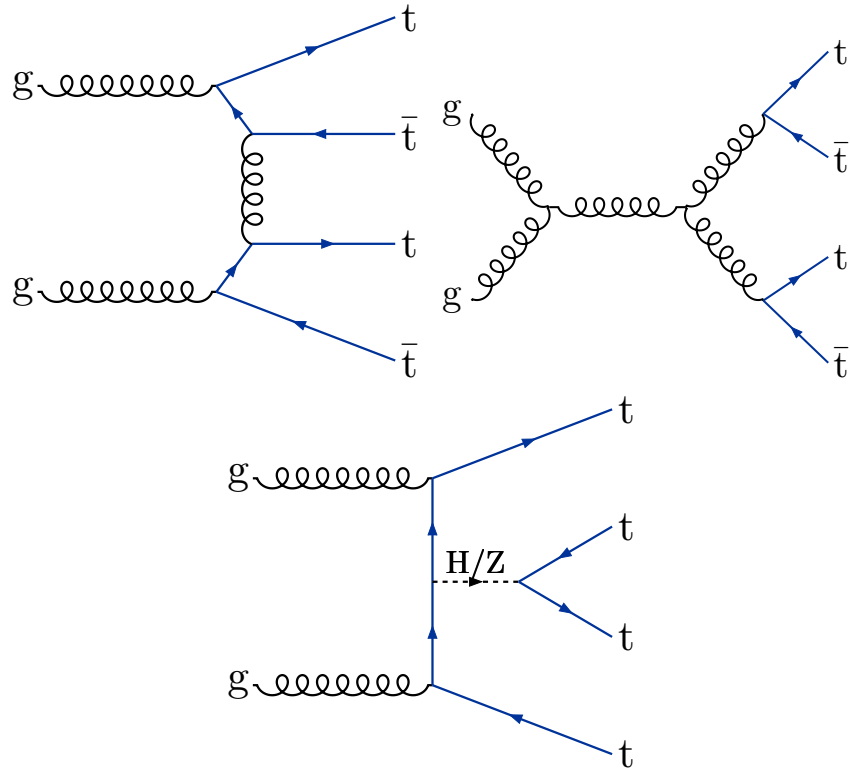


Figure 2.7: Typical Feynman diagrams for  $t\bar{t}t\bar{t}$  production at leasting order in the SM.

## 2.2.1 On-shell

### 2.2.1.1 Two Higgs doublet models

In the spirit of generality, a simple possible extension of the SM is the two Higgs doublet model (2HDM) [29]. For example, the Minimal Supersymmetric Standard Model (MSSM) has two Higgs doublets instead of the SM's single doublet. Two doublets provides for five physical states: a light scalar boson  $h$ , a heavy scalar boson  $H$ , a heavy pseudoscalar boson  $A$ , and two charged bosons  $H^\pm$ . Their masses  $(m_h, m_H, m_A, m_{H^\pm})$  constitute four of the six parameters used in the 2HDM. The other two are  $\tan \beta$ , which is the ratio of vacuum expectation values of the two Higgs doublets, and  $\alpha$ , which is the rotation angle that diagonalizes the mass matrix of the two CP-even scalar states  $h$  and  $H$ .

Given the observation of a new boson in 2012 [4, 5], which has since been shown to have very SM Higgs-like properties, there should be a phenomenological constraint on 2HDM theories to account for this. Fortunately, in a Type-II 2HDM in the alignment limit,  $\sin(\beta - \alpha) \rightarrow 1$ , the CP-even scalar  $h$  has couplings which are SM-like, meaning it can be identified with the discovered particle, and other states constitute new physics to be discovered.

In Type-II 2HDM, the couplings of the heavy scalar and pseudoscalar to SM vector bosons are also suppressed, and vanish as  $\cos(\beta - \alpha) \rightarrow 0$ . In this limit, production happens mainly through gluon-fusion. However, the direct search for such new physics via resonant  $t\bar{t}$  production is hampered by interference with the large SM production of

$t\bar{t}$  [30, 31]. As an alternative to direct production, since the branching ratio of the heavy scalar state  $H$  to up-type quarks (e.g., the top quark) is proportional to  $1/\tan\beta$ , at low  $\tan\beta$ , associated production with three and four top quark final states provide a relatively clean handle to probe Type-II 2HDM scenarios [32, 33]. The one or two top quark associated production modes are shown in Fig. 2.8, where the intermediate heavy boson decays into  $t\bar{t}$  at low  $\tan\beta$ , resulting in final states of  $t\bar{t}t\bar{t}$ ,  $t\bar{t}W$ , and  $t\bar{t}q\bar{q}$ , respectively. Heavy boson with masses above twice that of the top quark ( $m_{H/A} > 350$  GeV) almost exclusively decay into  $t\bar{t}$ . Thus, a SM search for  $t\bar{t}t\bar{t}$  would be optimized to directly probe the first of these three final states, while still retaining sensitivity to the latter two, for sufficiently massive scalar and pseudoscalar bosons to allow for on-shell decays into  $t\bar{t}$ .

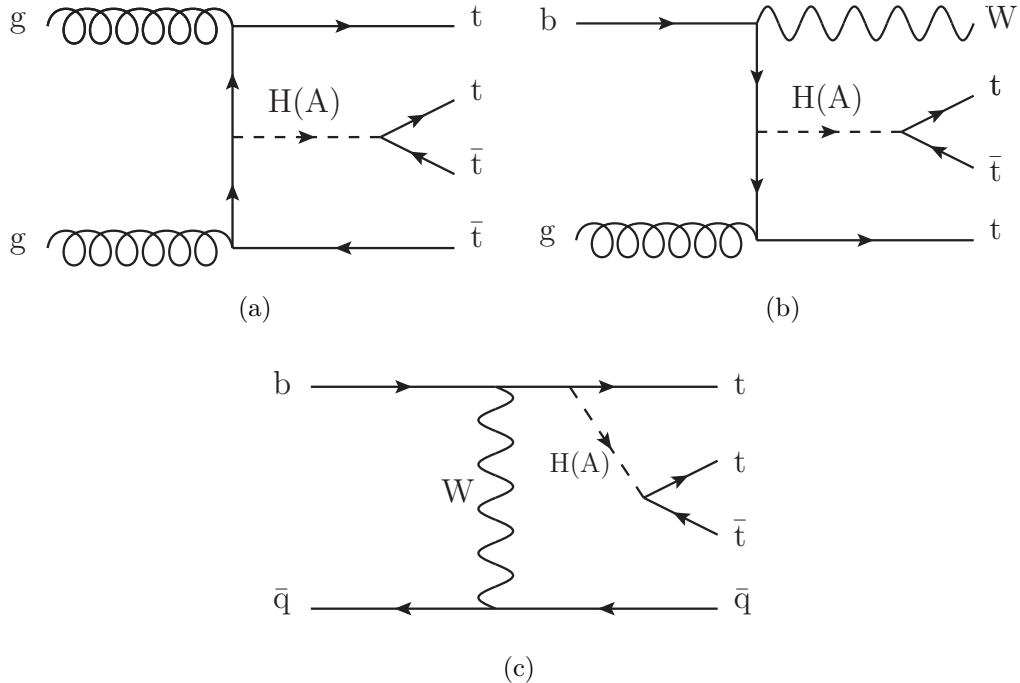


Figure 2.8: Diagrams for scalar (pseudoscalar) production in association with one or two top quarks.

Leading order cross sections (times branching ratio into  $t\bar{t}$ ), obtained similarly to Ref. [33], for a Type-II 2HDM scenario in the exact alignment limit are shown in Fig. 2.9, as a function of mediator mass and  $\tan \beta$ . Processes with  $H$  and  $A$  mediators are considered separately and the charged bosons  $H^\pm$  are decoupled by setting their masses to 10 TeV. Cross sections are generally slowly falling as a function of increasing mass and sharply falling for increasing  $\tan \beta$ . One dimensional cross section plots for three particular values of  $\tan \beta$  are shown in Fig. 2.10, and range from approximately 45 fb at the  $2m_t$  threshold to 9 fb at  $m_H = 650$  GeV for  $\tan \beta = 1$ .

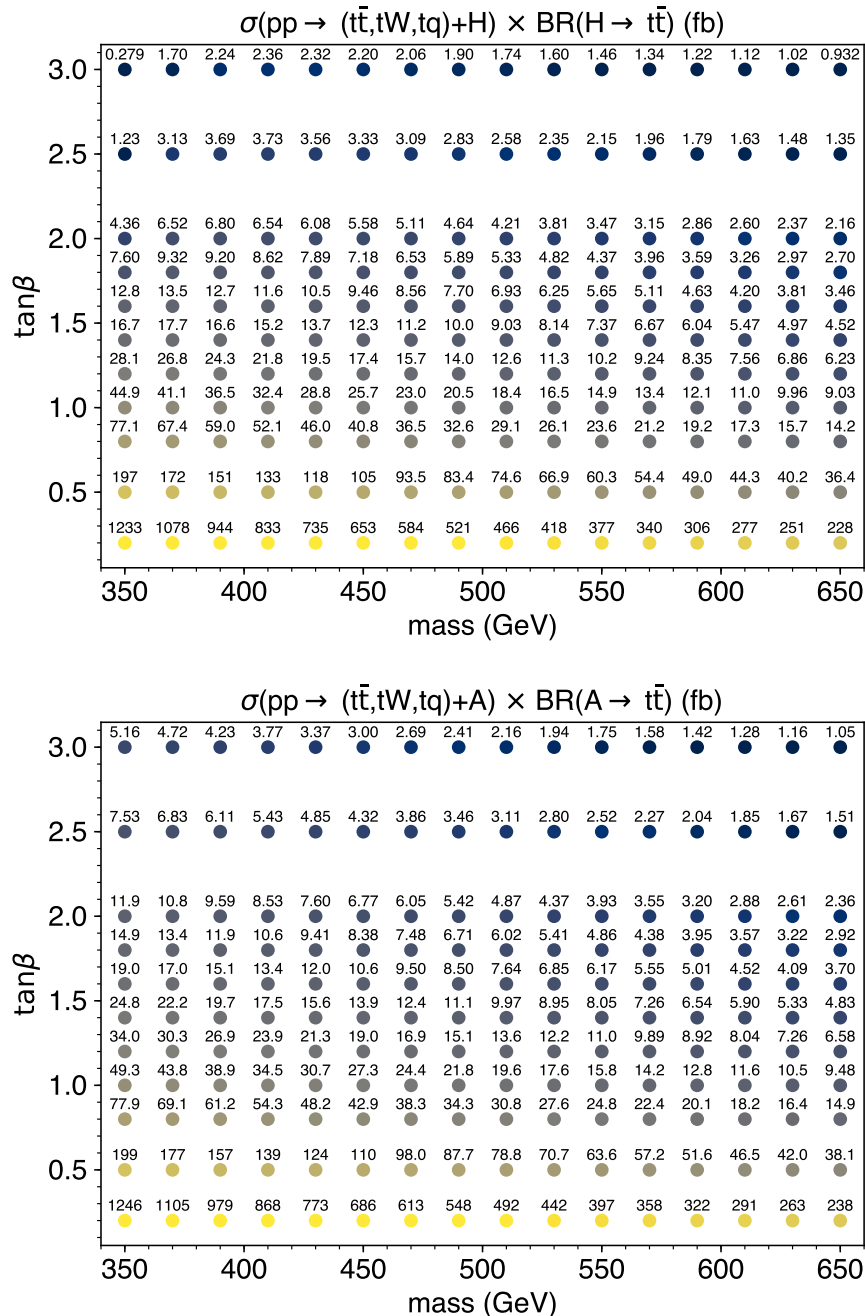


Figure 2.9: Cross sections times branching ratio into  $t\bar{t}$  for a heavy scalar boson  $H$  (top) or heavy pseudoscalar boson  $A$  (bottom) as a function of boson mass and  $\tan\beta$ .

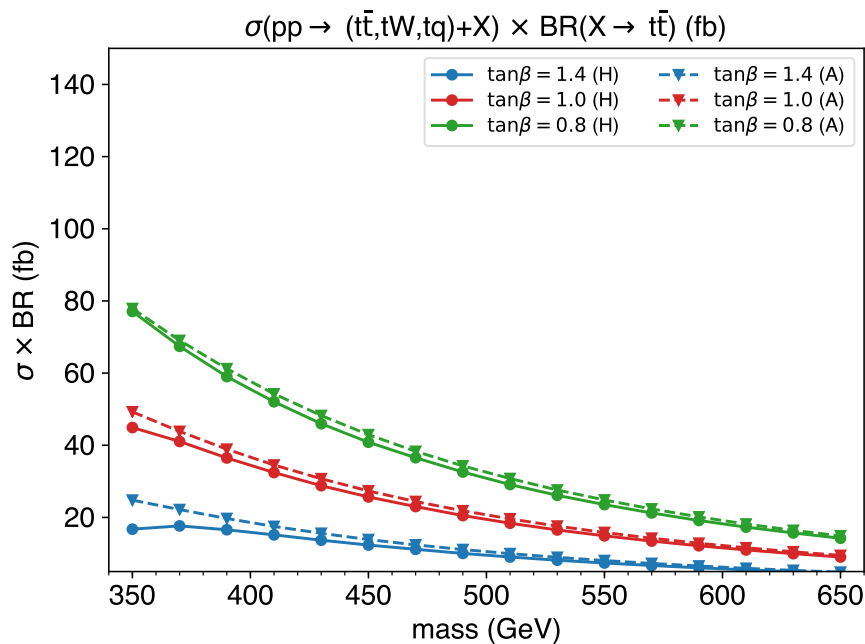


Figure 2.10: Cross sections times branching ratio into  $t\bar{t}$  for a heavy scalar boson  $H$  or heavy pseudoscalar boson  $A$  as a function of boson mass for three assumptions of  $\tan\beta$  (0.8, 1.0, 1.4).

### 2.2.1.2 Simplified dark matter models

Similarly to 2HDM, simplified dark matter (DM) models with scalar or pseudoscalar mediators decaying into a pair of dark matter or SM particles can be probed [34]. The production of these mediators, and subsequent decay into invisible dark matter particles, in association with a one or two top quarks, was performed by CMS with the 2016 dataset Ref.[35, 36]. The production diagrams are shown in Fig. 2.11.

In the framework of a simplified dark matter model, where the scalar ( $\phi$ ) or pseudoscalar (a) mediator couples dark matter and SM particles, the relevant terms of the interaction lagrangian are of the form

$$\mathcal{L}_\phi = g_\chi \phi \bar{\chi} \chi + \frac{g_q \phi}{\sqrt{2}} \sum_f y_f \bar{f} f \quad \mathcal{L}_a = i g_\chi a \bar{\chi} \gamma^5 \chi + \frac{i g_q a}{\sqrt{2}} \sum_f y_f \bar{f} \gamma^5 f$$

where  $y_f$  are the fermionic yukawa couplings. The coupling constants  $g_\chi$  and  $g_q$  give the relative strengths of the mediator coupling to dark matter and SM particles, and are used interchangeably with  $g_{\text{DM}}$  and  $g_{\text{SM}}$ , respectively. The model has four free parameters ( $g_\chi$ ,  $g_q$ ,  $m_\chi$ , and  $m_a$ ) which are reduced to two with the assumption of  $g_\chi = g_q = 1$ .

When the mediator mass is above  $2m_t \approx 350\text{GeV}$ , on-shell decay to  $t\bar{t}$  becomes kinematically accessible, resulting in three or four top quark final states, so we instead consider a version of the diagrams of Fig. 2.11 with a decay of the mediator into  $t\bar{t}$  rather than a pair of (invisible) dark matter particles  $\chi\bar{\chi}$ . Consequently, the production diagrams and kinematics are identical to those of the Type-II 2HDM for certain assumptions

of mediator mass, dark matter mass, and  $\tan \beta$ , and  $\phi/a$  can be identified as  $H/A$ .

In this way, the three or four top quark final states allow complementarity with the CMS analysis from Ref. [35] which relied on a final state with  $t\bar{t}$  and missing transverse energy, provided that the mediator mass is sufficiently large to allow for on-shell decays of the mediator into  $t\bar{t}$ . Lower mediator masses are more effectively probed by Ref. [35].

The product of cross section and branching ratio of the mediators into  $t\bar{t}$ , under the assumption of  $g_{\text{DM}} = g_{\text{SM}} = 1$ , calculated as in Ref. [35], is shown in Fig. 2.12. Note that when  $2m_\chi > m_{H/A}$ , the decay of the mediators into DM is suppressed in favor of the next-leading mode,  $t\bar{t}$ , and thus the cross sections become independent of  $m_\chi$  above the marked diagonals. The cross sections at large  $m_\chi$  are nearly identical to those of the 2HDM with  $\tan \beta = 1$  shown previously. However, below the diagonal, the mediator prefers to decay into  $\chi\bar{\chi}$  and a search for three or four top quark final states loses sensitivity.

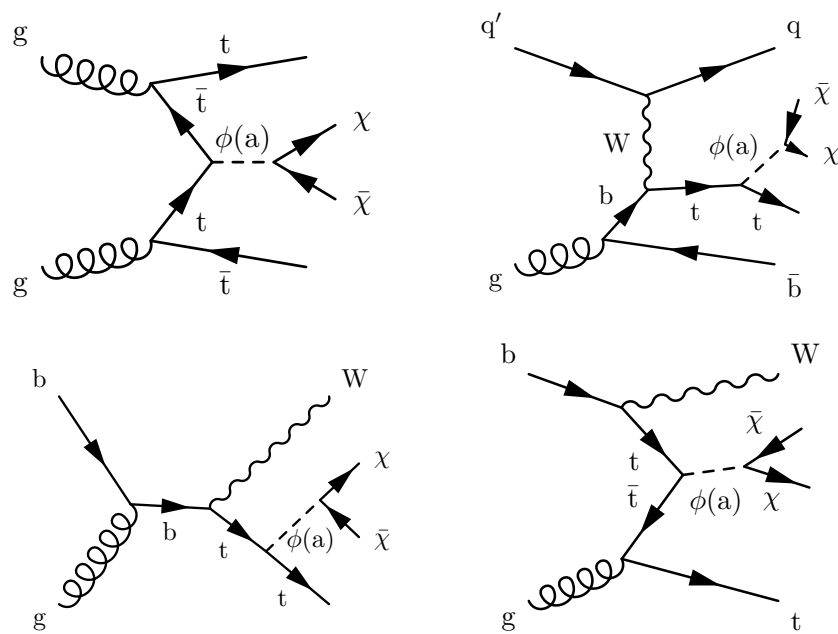


Figure 2.11: Diagrams for scalar (pseudoscalar) production in association with a  $t\bar{t}$  pair (top left), associated t-channel single top (top right), associated  $tW$  (bottom row). The mediator subsequently decays into a pair of invisible DM particles  $\chi\bar{\chi}$ .

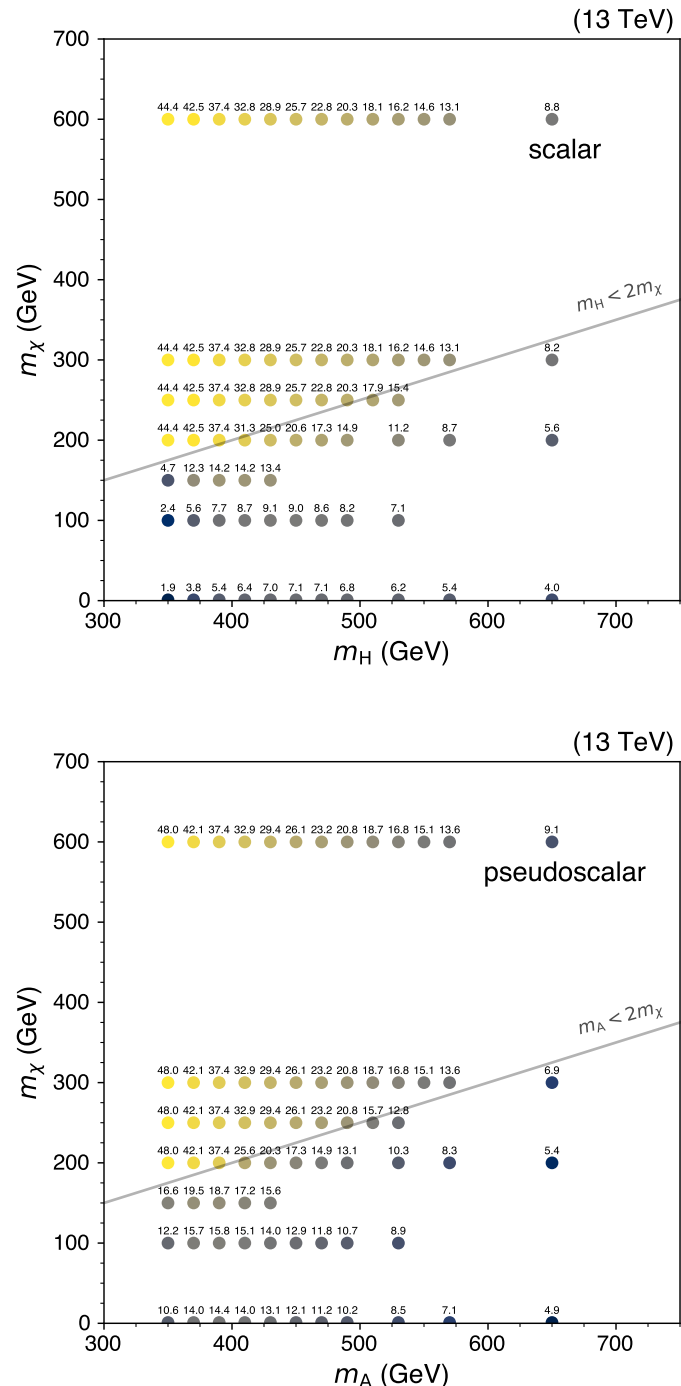


Figure 2.12: Cross sections (times branching ratio into  $t\bar{t}$ ), in units of fb, assuming  $g_{DM} = g_{SM} = 1$ , in the plane of  $m_\chi$  versus  $m_{H/A}$  (top/bottom).

## 2.2.2 Off-shell

### 2.2.2.1 Top quark yukawa coupling

The SM  $pp \rightarrow t\bar{t}t\bar{t}$  process includes diagrams with virtual Higgs bosons, as shown in Fig. 2.13. The amplitude corresponding to these diagrams is proportional to the square of the top Yukawa coupling, and thus, the cross section of SM  $t\bar{t}t\bar{t}$  provides a probe of the top quark Yukawa coupling.

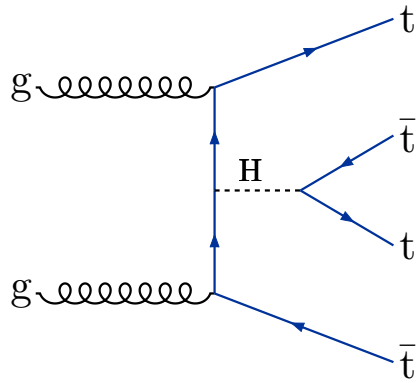


Figure 2.13: One of the Feynman diagrams for  $t\bar{t}t\bar{t}$  including a virtual Higgs.

Using the notation of Reference [37] the  $t\bar{t}t\bar{t}$  cross section can be written as

$$\sigma(t\bar{t}t\bar{t}) = \sigma^{\text{SM}}(t\bar{t}t\bar{t})_{g+Z/\gamma} + k_t^4 \sigma^{\text{SM}}(t\bar{t}t\bar{t})_H + k_t^2 \sigma_{\text{int}}^{\text{SM}} \quad (2.1)$$

where  $k_t \equiv y_t/y_t^{\text{SM}}$ ,  $y_t$  is the top Yukawa coupling, and  $y_t^{\text{SM}}$  is its SM value. In equation 2.1 the first term on the right hand side corresponds to the SM contribution to the cross section from diagrams with gluons or  $Z/\gamma$ , the second term is the contribution from diagrams with virtual Higgs bosons, and the third term is the interference between the two previous terms. Therefore, given a theoretical calculation and a measurement of

$\sigma(t\bar{t}t\bar{t})$ , one can put constraints on  $|y_t/y_t^{\text{SM}}|$ .

The authors of Reference [37] have calculated the cross section terms at LO. These are given in Table 2.2 and are shown in Fig. 2.14, where the figure shows a curve normalized such that the prediction matches the NLO calculation of the  $t\bar{t}t\bar{t}$  cross section of  $12.0^{+2.2}_{-2.5}$  fb. The upper and lower values given in Table 2.2 correspond to variations of the renormalization and factorization scale up and down by a factor of two, respectively.

	lower	central	upper
$\sigma^{\text{SM}}(t\bar{t}t\bar{t})_{g+Z/\gamma}$	14.104 fb	9.997 fb	6.378 fb
$\sigma^{\text{SM}}(t\bar{t}t\bar{t})_H$	1.625 fb	1.167 fb	0.7655 fb
$\sigma_{\text{int}}^{\text{SM}}$	-2.152 fb	-1.547 fb	-0.999 fb

Table 2.2: LO calculation of the terms in equation 2.1 from Reference [37]. The uncertainties are from private communications with the authors.

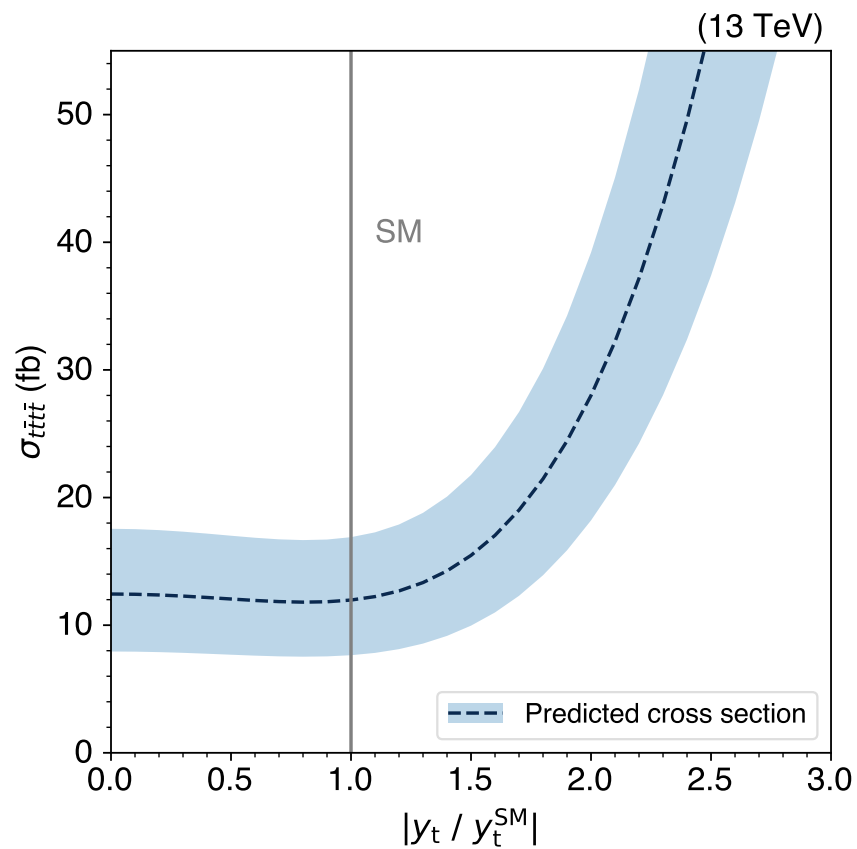


Figure 2.14: Predicted  $t\bar{t}t\bar{t}$  cross section as a function of  $|y_t/y_t^{\text{SM}}|$ .

### 2.2.2.2 Light off-shell mediators

The production of  $t\bar{t}t\bar{t}$  may also be influenced by a neutral scalar mediator ( $\phi$ ) or neutral vector mediator ( $Z'$ ) which couple to top quarks and have masses less than twice the mass of the top quark, distinguishing them from similar processes within the 2HDM framework, for example. The off-shell contributions to the SM  $t\bar{t}t\bar{t}$  production can be large, as shown in Ref. [38]. For a large range of masses, kinematics are identical when considering these additional processes, so that the total  $t\bar{t}t\bar{t}$  cross section is subject to a simple rescaling. Corresponding coupling terms in the lagrangian are of the form

$$\mathcal{L}_{Z'} = -g_{tZ'} \bar{t}_R Z' t_R \quad \mathcal{L}_\phi = -g_{t\phi} \bar{t}_L \phi t_R \quad (2.2)$$

There is an approximate independence of kinematics on the coupling strength and mediator mass [38], so a single upper limit on the  $t\bar{t}t\bar{t}$  cross section can be used to place constraints on couplings  $g_{tZ'}$  and  $g_{t\phi}$  as a function of masses  $m_{Z'}$  and  $m_\phi$ , respectively. Cross sections of  $t\bar{t}t\bar{t}$  (normalized to SM, and calculated as in Ref. [38]) as a function of  $g_{tZ'}$  and  $g_{t\phi}$ , for different assumptions of  $m_{Z'}$  and  $m_\phi$ , are shown in Fig. 2.15. To illustrate a particular example, the horizontal dotted line in the figures represents excluding cross sections more than double that of the SM. These are translated into exclusions on  $g_{tZ'}$  and  $g_{t\phi}$  via crossing points that are projected onto the x axis.

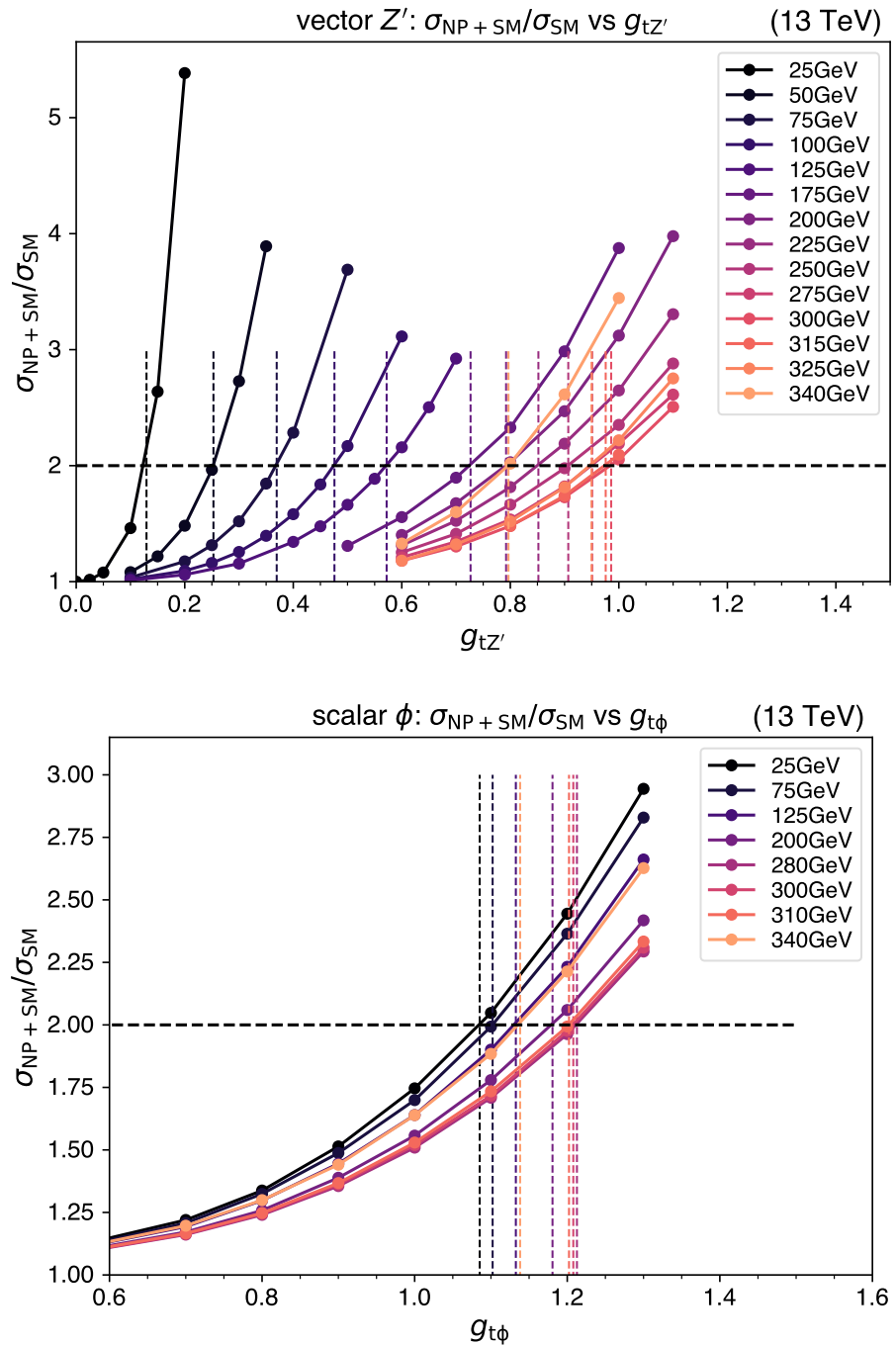


Figure 2.15: Cross sections of  $t\bar{t}t\bar{t}$  (normalized to SM) as a function of  $g_{tZ'}$  (upper) and  $g_{t\phi}$  (lower) for different assumptions of  $m_{Z'}$  and  $m_\phi$ , respectively.

### 2.2.2.3 Oblique Higgs parameter

In a universal effective field theory framework, the Higgs oblique parameter  $\hat{H}$ , defined as the Wilson coefficient of the dimension-6 operator modifying the Higgs boson propagator, can result in deviations of the SM  $t\bar{t}t\bar{t}$  cross section, as shown in Ref. [39]. These (off-shell) deviations can be constrained to a level which is competitive with constraints from on-shell processes.

The two main characteristic effects of this oblique parameter are an additional term in the SM Higgs boson propagator

$$P_h(p^2) \approx \frac{i}{p^2 - m_h^2} - \frac{i\hat{H}}{m_h^2}, \quad (2.3)$$

and a rescaling of the fermionic higgs couplings

$$\kappa_f = 1 - \hat{H}. \quad (2.4)$$

Using the latest combined fits from the ATLAS experiment for the (on-shell) fermionic couplings, with  $80\text{fb}^{-1}$  of 13 TeV data, Ref. [39] finds a constraint on the oblique parameter of  $\hat{H} < 0.16$  at 95% CL.

Ref. [39] also calculates that the cross section of (off-shell)  $t\bar{t}t\bar{t}$  is subject to a fractional

modification (with respect to the SM cross section) at 14 TeV, given by,

$$\frac{\sigma_{\hat{H}+\text{SM}}}{\sigma_{\text{SM}}} = 1 + 0.03 \left( \frac{\hat{H}}{0.04} \right) + 0.15 \left( \frac{\hat{H}}{0.04} \right)^2. \quad (2.5)$$

For an oblique parameter value of 0.1, the formula predicts a doubling of the SM cross section of  $t\bar{t}t\bar{t}$ .

The SM model within the MadGraph [40] generator was modified to take into account the extra term in the propagator, as well as the rescaling of the top-yukawa coupling, and the calculation is repeated at 13 TeV. The resulting curve is shown in Fig. 2.16.

When searching for SM  $t\bar{t}t\bar{t}$  and placing upper limits on the production cross section, one can use the relative size of the upper limit with respect to the SM prediction to exclude  $\hat{H}$  values above a threshold. For example, excluding cross sections more than double that of the SM,  $\hat{H}$  values above approximately 0.14 can be excluded. There are two important caveats that will need to be taken into account when performing an interpretation for  $\hat{H}$ . First, the kinematics of  $t\bar{t}t\bar{t}$  will be slightly different depending on the value of  $\hat{H}$ . Second, the SM process  $t\bar{t}H$ , which is relevant for the  $t\bar{t}t\bar{t}$  search, is proportional to  $y_t^2 = (1 - \hat{H})^2$  ( $\approx 0.74$  at  $\hat{H} = 0.14$ ).

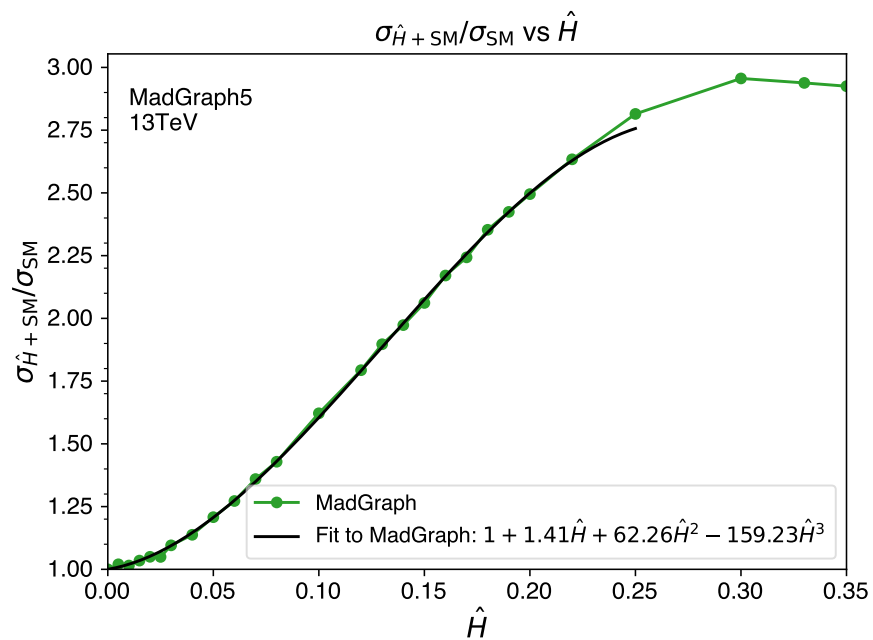


Figure 2.16: Cross section (normalized to SM) as a function of oblique parameter  $\hat{H}$ . The green curve is a calculation from MadGraph at 13 TeV, and the solid black curve is a cubic fit to the calculation.

# Chapter 3

## Objects and selections

### 3.1 Jets, MET

#### 3.1.1 Jets

Jets are reconstructed from charged PF candidates clustered with the anti- $k_t$  algorithm [41, 42] using a distance parameter of 0.4. Charged particles not originating from the primary vertex (PV), taken to be the reconstructed vertex with the largest value of  $\Sigma p_T^2$ , are removed before clustering the jets. While this is a direct mitigation of the effect of pileup, the jet  $p_T$ , calculated as the vector sum of the constituent PF candidates, is susceptible to further contributions from pileup and detector effects. However, jet energy corrections, primarily parameterized by jet  $p_T$  and  $\eta$ , are derived using data and simulation to counteract these effects on a jet-by-jet basis [43, 44].

Additional jet selections (tight jet identification) are applied to reject pathological

jets. For data collected during 2016, they are

- neutral hadronic energy fraction  $< 0.99$
- neutral electromagnetic energy fraction  $< 0.99$
- number of constituents  $> 1$
- charged hadronic energy fraction  $> 0$
- charged multiplicity  $> 0$
- charged electromagnetic energy fraction  $> 0$

and for data collected during 2017 and 2018, the selections are

- neutral hadronic energy fraction  $< 0.9$
- neutral electromagnetic energy fraction  $< 0.9$
- number of constituents  $> 1$
- charged hadronic energy fraction  $> 0$
- charged multiplicity  $> 0$

To avoid double counting of objects, selected jets are those that do not overlap with analysis leptons (within a cone of  $\Delta R \equiv \sqrt{\Delta\eta^2 + \Delta\phi^2} = 0.4$ ), and have  $p_T > 40\text{GeV}$  and  $|\eta| < 2.4$ . The multiplicity of selected jets is defined to be  $N_{\text{jets}}$ . The scalar sum of selected jet  $p_T$  is called  $H_T$ .

### 3.1.2 B-tagging

Many of the SUSY models probed in this analysis have a high multiplicity of top quarks; SM four top quark production has four. Each top quark decays into a b quark and W boson, so jets arising from b quarks are an important object to efficiently identify. Hadrons containing b quarks have lifetimes that allow them to travel on the order of a millimeter from the collision before decaying, creating tracks pointing to a secondary vertex. We use a deep neural network algorithm, DeepCSV [45], which makes use of information such as tracks and secondary vertices to produce a discriminating value for b jets. A threshold value (the medium working point) on this discriminant is set such that the efficiency to correctly identify a b jet is approximately 65% for jet  $p_T$  around 40 GeV while maintaining a misidentification rate of 1% for light-flavor jets (udsg). While they are not directly used here, there are two additional working points for the b-tagging, loose and tight, which have 10% and 0.1% misidentification rates for light-flavor jets, respectively.

This  $N_b$  variable is defined as the multiplicity of b-tagged jets with  $p_T > 25\text{GeV}$  and  $|\eta| < 2.4$  which are not overlapping with leptons. The lower threshold compared to nominal jets above allows for increased signal acceptance for softer event topologies.

On top of the jet-by-jet corrections, event-level weights, known as b tag scale factors, are applied to bring data and simulation  $N_b$  into agreement, and they are derived by effectively reshaping the DeepCSV discriminator distribution [46].

### 3.1.3 MET

The missing transverse energy, equivalently referred to as MET,  $\vec{E}_T$ , or  $p_T^{\text{miss}}$ , is defined as the magnitude of the negative of the vectorial sum of the  $\vec{p}_T$  of PF candidates in an event [47].

The MET has a Type-I correction applied, which fully propagates the jet energy corrections into the computation:

$$\vec{E}_T = \vec{E}_T^{\text{raw}} - \sum_{\text{jets}} \left( \vec{p}_{T,\text{jet}}^{\text{corr}} - \vec{p}_{T,\text{jet}} \right) \quad (3.1)$$

Additional event-level filters detailed in [48] are applied to reject pathological events associated with misreconstruction, or sources of detector noise.

## 3.2 Leptons

### 3.2.1 Identification

Muons are reconstructed by combining information from tracker hits with those in the muon system to form a global fit. The base identification criteria for reconstructed muons is encapsulated in the “medium muon ID” [49] and requires a certain level of quality in the tracker and muon system track matching.

Analysis muons must have  $p_T > 10\text{GeV}$  and  $|\eta| < 2.4$ . We require that muons have a relative uncertainty less than 20% on the reconstructed momentum ( $\delta p_T/p_T < 0.2$ ). This helps ensure that the charge of the muon track has not been misreconstructed.

Analysis electrons must have  $p_T > 15\text{GeV}$  and  $|\eta| < 2.5$ . Electrons are identified by constructing a boosted decision tree (BDT) with a variety of variables tied to the track and ECAL deposits used to reconstruct the electron [18]. These include

- ECAL shower-shape variables
  - $\sigma_{i\eta i\eta}$  (weighted width of shower along  $\eta$ )
  - $\sigma_{i\phi i\phi}$  (weighted width of shower along  $\phi$ )
  - cluster circularity
  - cluster  $\eta, \phi$  widths
  - $R_9$ , the ratio of energy in 3x3 to 5x5 set of towers surrounding the seed crystal
  - H/E, the ratio of (adjacent) HCAL energy to ECAL deposits
- track-cluster matching variables
  - $E/p_{\text{in}}, E/p_{\text{out}}$ , where  $p_{\text{in/out}}$  is the innermost/outermost track momentum
  - $\Delta\eta_{\text{in}}$  ( $\eta$  difference between cluster and inner track)
  - $\Delta\eta_{\text{out}}$
  - $\Delta\phi_{\text{in}}$  ( $\phi$  difference between cluster and inner track)
  - $|1/E_{\text{clust}} - 1/p|$
- track variables
  - $\chi^2$  quality of combinatorial track finder (CTF) and Gaussian-sum filter (GSF) tracks

- number of CTF and GSF hits
- $(p_{\text{in}} - p_{\text{out}})/p_{\text{in}}$ , fraction of energy lost through Bremsstrahlung

The BDT discriminant is converted into a boolean decision per lepton with working points depending on the year and  $p_T$ , which will not be shown here for the sake of brevity. We simply take and refer to two boolean decisions as the “loose” and “tight” working points, where the tight WP has relatively lower efficiency to select electrons, but also a lower efficiency to misidentify other objects as electrons.

For electrons, we additionally consider a conversion veto that locates and rejects  $\gamma \rightarrow e^+e^-$ , and a “number of expected missing inner hits” variable, which is the number of detector hits in the inner tracker which should have registered a hit but did not. Electrons must have no such missing hits. Electrons must also have agreement between three different methods used to compute the charge [50].

For both electrons and muons, we require  $|d_{xy}| < 0.05 \text{ cm}$ ,  $|d_z| < 0.1 \text{ cm}$ ,  $\text{SIP}_{3D} < 4$ . The variables  $|d_{xy}|$  and  $|d_z|$  are the transverse and longitudinal displacements between the PV and the point of closest approach (PCA) of the lepton’s track, respectively. The 3D impact parameter significance,  $\text{SIP}_{3D}$ , is defined as the 3D displacement between the PCA and PV divided by the measurement uncertainty. These variables and selections make sure the leptons are produced in a prompt fashion.

The final lepton reconstruction and identification efficiency is between 45% and 70% for electrons with  $p_T > 25 \text{ GeV}$ , and between 70% and 90% for muons in the same momentum range. In the lower momentum range of 15-25 GeV for electrons, the efficiency

is 40%, and in the range of 10-25 GeV for muons, the efficiency is 55%.

### 3.2.2 Isolation

Conceptually, a lepton can be labeled isolated if the ratio of energy in a cone surrounding the lepton to the energy of the lepton itself (“relative isolation”) is below a certain threshold. However, we instead use three more sophisticated variables, improving upon this concept for robustness, to classify leptons as isolated:

- “mini-isolation”  $I_{\text{mini}}$ :

$$I_{\text{mini}} = \frac{\sum_R p_T(h^\pm) - \max(0, \sum_R p_T(h^0) + p_T(\gamma) - \rho \mathcal{A} (R/0.3)^2)}{p_T(\ell)}. \quad (3.2)$$

where  $\rho$  is the event-level energy density from pileup, and  $\sum_R p_T(h^\pm)$ ,  $\sum_R p_T(h^0)$ ,  $\sum_R p_T(\gamma)$  are the sums of the  $p_T$  of charged hadrons, neutral hadrons, and photons, respectively. The sum is performed within a lepton  $p_T$ -dependent cone of radius  $R$ , decreasing in size for higher lepton  $p_T$ :

$$R = \frac{10}{\min(\max(p_T(\ell), 50), 200)} \quad (3.3)$$

The effective areas  $\mathcal{A}$  are constants calculated in coarse bins of lepton  $\eta$  such that the last term of the numerator represents the contribution from pileup and is subtracted off. Requiring  $I_{\text{mini}}$  to be below a particular value ensures that the lepton is isolated.

- $p_T^{\text{ratio}}$ , defined as the ratio of the lepton  $p_T$  to the  $p_T$  of the jet geometrically closest to, or containing, the lepton:

$$p_T^{\text{ratio}} = \frac{p_T(\ell)}{p_T(\text{jet})} \quad (3.4)$$

In order to avoid an over-correction on prompt leptons, the application of the jet energy correction to mitigate is only applied on the hadronic part of the jet. That is, the denominator of  $p_T^{\text{ratio}}$  is corrected for pileup effects after the lepton is subtracted out, and the lepton is subsequently added back.

- $p_T^{\text{rel}}$ :

$$p_T^{\text{rel}} = \frac{\left| (\vec{p}(\text{jet}) - \vec{p}(\ell)) \times \vec{p}(\ell) \right|}{|\vec{p}(\text{jet}) - \vec{p}(\ell)|} \quad (3.5)$$

This variable is a measure of the relative transverse separation between the lepton and matching jet. For leptons arising from the decay of B mesons, for example, this quantity exhibits a kinematic cutoff of a few GeV. For leptons that happen to overlap accidentally with jets,  $p_T^{\text{rel}}$  compares two uncorrelated quantities and exhibits no kinematic cutoff, so this quantity can be large. This property allows us to recover leptons that would be labeled non-isolated by the previous two variables.

Using the above three variables, we classify a lepton as isolated if the following boolean condition is satisfied:

$$I_{\text{mini}} < I_1 \wedge (p_T^{\text{ratio}} > I_2 \vee p_T^{\text{rel}} > I_3) \quad (3.6)$$

where  $I_i$  threshold values depend on the lepton flavor and PU conditions of the flavor of the lepton. These values are tabulated in Table 3.2.2.

	e/ $\mu$ loose WP	$\mu$ tight WP	e tight WP
$I_1$	0.4	0.16 (2016), 0.11 (2017/2018)	0.12 (2016), 0.07 (2017/2018)
$I_2$	0	0.76 (2016), 0.74 (2017/2018)	0.80 (2016), 0.78 (2017/2018)
$I_3$ (GeV)	0	7.2 (2016), 6.8 (2017/2018)	7.2 (2016), 8.0 (2017/2018)

Table 3.1: Isolation working points

### 3.3 Other variables

We make use of the minimum transverse mass ( $m_T^{\min}$ ) which is defined as:

$$m_T^{\min} = \min \left[ m_T(\ell_1, E_T^{\text{miss}}), m_T(\ell_2, E_T^{\text{miss}}) \right] \quad (3.7)$$

where a single transverse mass term is given by

$$m_T^{\min} = \sqrt{2p_T(\ell)E_T^{\text{miss}}(1 - \cos \Delta\phi_{\ell, E_T^{\text{miss}}})} \quad (3.8)$$

and  $\Delta\phi_{\ell, E_T^{\text{miss}}}$  is the azimuthal separation between the lepton and the  $p_T^{\text{miss}}$  vector.

For events where  $p_T^{\text{miss}}$  arises primarily from neutrinos from W boson decays, as is the case with the pervasive  $t\bar{t}$  and  $W$  processes, this variable has a kinematic cutoff at the W boson mass,  $m_W$ . Signal events where the  $p_T^{\text{miss}}$  is generated from an energetic  $\tilde{\chi}_1^0$  particle will not exhibit such a kinematic cutoff.

Figure 3.1 shows the distribution of  $m_T^{\min}$  for a signal hypothesis T1tttt and the  $t\bar{t}$  background, with the W boson mass marked as a vertical line. It is clear that the  $t\bar{t}$  background is almost completely bounded by the W mass, while the signal has a large tail extending beyond the W mass.

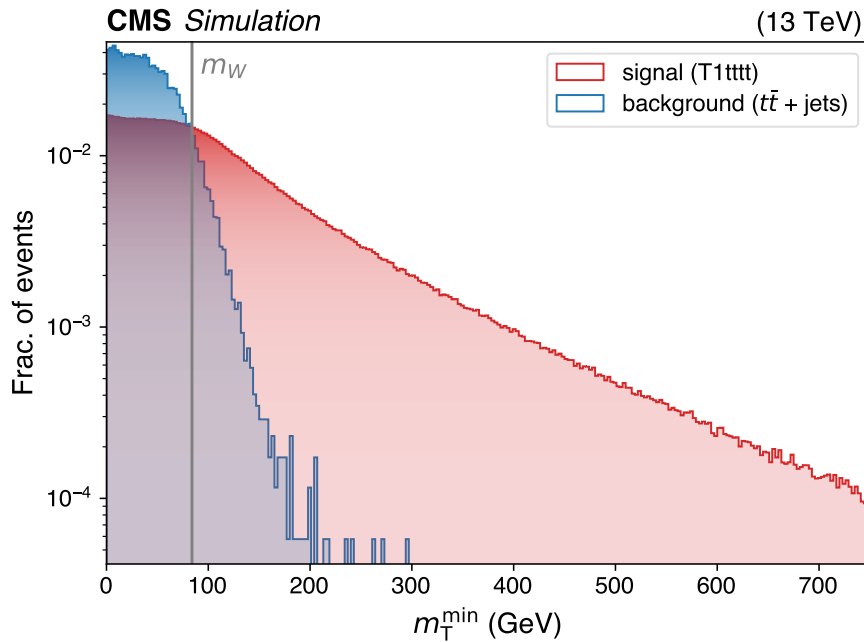


Figure 3.1: Normalized distribution of  $m_T^{\min}$  shown for signal hypothesis T1tttt and  $t\bar{t}$  background.

## 3.4 Trigger

Clearly before one can analyze events, one must have collected them with the detector first. Triggers are meant to identify and save interesting events in data while making sure to not overwhelm the readout hardware, reconstruction software, and storage used by CMS. Same-sign searches make use of dilepton triggers which require at least two leptons

at trigger level of a given  $p_T$ , usually along with some isolation quantities or  $H_T$ . For a given trigger rate, the more stringent the requirements on isolation or  $H_T$ , the lower the thresholds on lepton  $p_T$ .

In the SUSY analysis, based on trigger thresholds, we only consider muons (electrons) with  $p_T$  of at least 10 (15) GeV. For events with lepton  $p_T < 25$  GeV for both SS leptons, the set of signal triggers, depending on year and SS lepton pair flavor, is given in Table 3.4, otherwise, the signal triggers in Table 3.4 are used. For example, the HLT\_Ele23\_Ele12\_CaloIdL\_TrackIdL\_IsoVL\_DZ trigger requires at least one electron with  $p_T > 23$  GeV and another with  $p_T > 12$  GeV, which meet some loose amount of identification and isolation criteria and a cut on  $d_z$ . For other triggers, the substring “PFHT350” specifies a requirement of  $H_T > 350$  GeV at the HLT. Note that there is no pair charge enforced by the trigger, so both opposite- and same-sign pairs can pass these dilepton triggers.

The SM  $t\bar{t}t\bar{t}$  analysis considers muons and electrons with  $p_T$  of at least 20 GeV. As a result, the modified signal trigger strategy summarized in Table 3.4 is used.

A set of single lepton triggers, listed in Table 3.4, is used for the estimation of the fake rate, which will be discussed in the following chapter.

Final state	2016 Trigger Name
Same sign $\mu\mu$	HLT_DoubleMu8_Mass8_PFHT300
Same sign $ee$	HLT_DoubleEle8_CaloIdM_TrackIdM_Mass8_PFHT300
Same sign $e\mu$	HLT_Mu8_Ele8_CaloIdM_TrackIdM_Mass8_PFHT300
Final state	2017 Trigger Name
Same sign $\mu\mu$	HLT_DoubleMu4_Mass8_DZ_PFHT350
Same sign $ee$	HLT_DoubleEle8_CaloIdM_TrackIdM_DZ_Mass8_PFHT350
Same sign $e\mu$	HLT_Mu8_Ele8_CaloIdM_TrackIdM_Mass8_PFHT350_DZ
Final state	2018 Trigger Name
Same sign $\mu\mu$	HLT_DoubleMu4_Mass8/3p8_DZ_PFHT350
Same sign $ee$	HLT_DoubleEle8_CaloIdM_TrackIdM_DZ_Mass8_PFHT350
Same sign $e\mu$	HLT_Mu8_Ele8_CaloIdM_TrackIdM_Mass8_PFHT350_DZ

Table 3.2: Summary of the signal triggers for the SUSY analysis with low lepton  $p_T$ 

Final state	2016 Trigger Name
Same sign $\mu\mu$	HLT_(Tk)Mu17_TrkIsoVVL_(Tk)Mu8_TrkIsoVVL(_DZ)
Same sign $ee$	HLT_Ele23_Ele12_CaloIdL_TrackIdL_IsoVL_DZ
Same sign $e\mu$	HLT_Mu23/8_TrkIsoVVL_Ele12/23_CaloIdL_TrackIdL_IsoVL_DZ
Final state	2017 Trigger Name
Same sign $\mu\mu$	HLT_Mu17_TrkIsoVVL_Mu8_TrkIsoVVL_DZ(_Mass3p8)
Same sign $ee$	HLT_Ele23_Ele12_CaloIdL_TrackIdL_IsoVL
Same sign $e\mu$	HLT_Mu23/8_TrkIsoVVL_Ele12/23_CaloIdL_TrackIdL_IsoVL_DZ
Final state	2018 Trigger Name
Same sign $\mu\mu$	HLT_Mu17_TrkIsoVVL_Mu8_TrkIsoVVL_DZ_Mass3p8
Same sign $ee$	HLT_Ele23_Ele12_CaloIdL_TrackIdL_IsoVL
Same sign $e\mu$	HLT_Mu23/8_TrkIsoVVL_Ele12/23_CaloIdL_TrackIdL_IsoVL_DZ

Table 3.3: Summary of the signal triggers for the SUSY analysis with high lepton  $p_T$

Final state	2016 Trigger Name
Same sign $\mu\mu$	HLT_DoubleMu8_Mass8_PFHT300
Same sign $ee$	HLT_DoubleEle8_CaloIdM_TrackIdM_Mass8_PFHT300
Same sign $e\mu$	HLT_Mu8_Ele8_CaloIdM_TrackIdM_Mass8_PFHT300
Final state	2017 Trigger Name
Same sign $\mu\mu$	HLT_Mu17_TrkIsoVVL_Mu8_TrkIsoVVL_DZ(_Mass8)
Same sign $ee$	HLT_Ele23_Ele12_CaloIdL_TrackIdL_IsoVL
Same sign $e\mu$	HLT_Mu23/8_TrkIsoVVL_Ele12/23_CaloIdL_TrackIdL_IsoVL_DZ
Final state	2018 Trigger Name
Same sign $\mu\mu$	HLT_Mu17_TrkIsoVVL_Mu8_TrkIsoVVL_DZ_Mass3p8
Same sign $ee$	HLT_Ele23_Ele12_CaloIdL_TrackIdL_IsoVL
Same sign $e\mu$	HLT_Mu23/8_TrkIsoVVL_Ele12/23_CaloIdL_TrackIdL_IsoVL_DZ

Table 3.4: Summary of the signal triggers for the SM  $t\bar{t}t\bar{t}$  analysis

Final state	Trigger Name
$\mu$ (isolated trigger leg)	HLT_Mu8/17_TrkIsoVVL
$\mu$ (non isolated trigger leg)	HLT_Mu8/17
$e$ (isolated trigger leg)	HLT_Ele12/23_CaloIdL_TrackIdL_IsoVL_PFJet30
$e$ (non isolated trigger leg)	HLT_Ele8/17_CaloIdM_TrackIdM_PFJet30

Table 3.5: Summary of the control triggers used for the fake rate measurement

Triggers are required for all events in data and simulation, and residual differences are corrected via trigger scale factors, which are applied to simulation to bring agreement with data. These scale factors are computed via the tag and probe method [51] to measure the efficiencies in data and simulation before taking the ratio. Efficiencies for dilepton triggers are the product of efficiencies for individual lepton selections (“lepton legs”). The tag and probe method defines the efficiency for a lepton leg as the number of events where the probed lepton candidate matches the studied lepton leg within  $\Delta R$  of 0.4, divided by the total number of selected events.

For example, to measure the efficiency for the isolated Mu17 leg of the dimuon trigger in 2018 data from Table 3.4, we first select events firing the HLT\_IsoMu27 trigger in the single muon dataset. Tag and probe pairs within the Z boson mass window are required to pass the offline analysis lepton selection to reduce the fake contribution and eliminate the need for parametric fits. The efficiency for the trigger leg is then calculated as the probability for the probe to pass the Mu17 leg selections. These efficiencies in data and simulation are shown as a function of muon  $p_T$  in Fig. 3.2. Their ratio, in the bottom panel, is the trigger efficiency for this lepton leg and is within 1% of unity in the plateau region of muon  $p_T > 20\text{GeV}$ . The actual scale factors are derived in bins of  $p_T$  and  $\eta$ , for each of the three years, and each of the triggers.

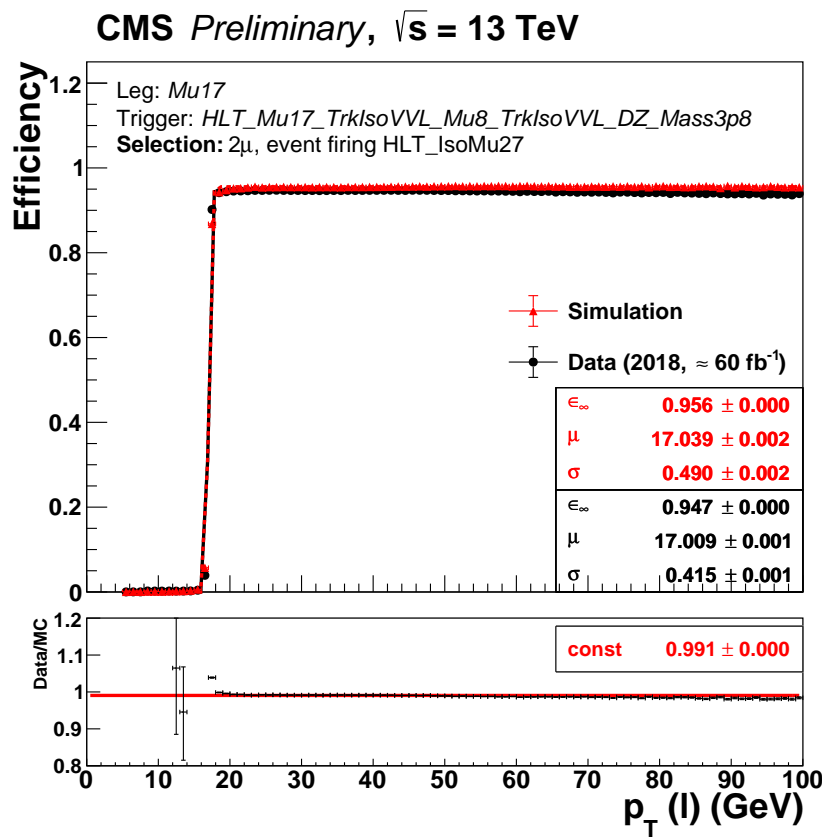


Figure 3.2: Efficiencies for the leading Mu17 leg of the high  $p_T$  isolated dimuon trigger used in 2018, separately for data and simulation.

### 3.5 Baseline selections

With the objects in place, we can now discuss the baseline selections used for the inclusive SUSY analysis and the more restricted SM  $t\bar{t}t\bar{t}$  analysis. As the title of this thesis suggests, both require the presence of at least two leptons (electrons or muons) with the same charge. Appropriate triggers are required for data and all simulation. Subsequent requirements on  $H_T$ ,  $N_{\text{jets}}$ ,  $N_b$ ,  $p_T^{\text{miss}}$ , and the leading/trailing lepton  $p_T$  are listed in Table 3.5.

Table 3.6: Summary of baseline selections

variable	SUSY analysis	SM $t\bar{t}t\bar{t}$ analysis
$N_{\text{jets}}$	$\geq 2$	$\geq 2$
$N_b$	$\geq 0$	$\geq 2$
$H_T$	$\geq 80 \text{ GeV}$	$\geq 300 \text{ GeV}$
$p_T^{\text{miss}}$	$> 0 \text{ GeV}$	$> 50 \text{ GeV}$
$p_T(\ell_1)$	$> 15/10 \text{ GeV (e}/\mu\text{)}$	$> 25 \text{ GeV}$
$p_T(\ell_2)$	$> 15/10 \text{ GeV (e}/\mu\text{)}$	$> 20 \text{ GeV}$

To reduce the background from production of low-mass resonances with charge-misidentified electrons, events that have a same-sign electron pair with invariant mass lower than 12 GeV are rejected.

For the SUSY analysis, we reject events with same-flavor lepton pairs that have an invariant mass ( $m_{\ell\ell}$ ) less than 12 GeV. Such a selection reduces backgrounds arising from decays of b-hadrons, c-hadrons, and the Drell-Yan (DY) process ( $Z/\gamma^* \rightarrow \ell^\pm \ell^\mp$ ).

For the SM  $t\bar{t}t\bar{t}$  analysis, events where a third lepton is identified with  $p_T > 7 \text{ GeV}$  for electrons or  $p_T > 5 \text{ GeV}$  for muons and which forms an opposite-sign (OS) same-

flavor pair with  $m_{\ell\ell} < 12\text{GeV}$  or in the range of 76-106 GeV are also rejected. However, for events with invariant mass in the range of 76-106 GeV where the  $p_T > 20\text{GeV}$  for the third lepton, this resonance veto is inverted and these events are instead used for a background control region enriched in  $t\bar{t}Z$  (CRZ) to be discussed in more detail in the next section. If a Z candidate is not found, a third tight lepton present in an event with  $p_T > 20\text{GeV}$  contributes to the lepton multiplicity,  $N_\ell$ , which starts at a value of 2 by virtue of the same-sign selection.

### 3.6 Event-level BDT

For the more targeted SM four top quark analysis, a BDT is used to increase the signal to background ratio.

The BDT classifier utilizes a gradient boosting algorithm implemented using the xgboost framework [52] to train 500 trees with a depth of 4 using simulation, and is based on the following 19 variables:

1.  $N_{\text{jets}}$
2.  $N_b$  (nominal, medium WP)
3.  $N_\ell$
4.  $p_T^{\text{miss}}$
5.  $N_b$  (calculated with the loose WP)

6.  $N_b$  (calculated with the tight WP)
7. scalar  $p_T$  sum of b-tagged jets
8.  $p_T(\ell_1)$
9.  $p_T(\ell_2)$
10.  $p_T(\ell_3)$
11.  $p_T(j_1)$  (leading jet)
12.  $p_T(j_6)$  (jet with sixth highest  $p_T$ )
13.  $p_T(j_7)$  (jet with seventh highest  $p_T$ )
14.  $p_T(j_8)$  (jet with eighth highest  $p_T$ )
15.  $\Delta\phi(\ell_1, \ell_2)$
16.  $\Delta\eta(\ell_1, \ell_2)$
17.  $m(\ell_1, j_1)$
18.  $q(\ell_1)$  (charge of the leading lepton)
19.  $\max(m(j_i)/p_T(j_i))$  over all selected jets in an event

The charge of the leading lepton provides a discrimination handle against SM processes which are charge asymmetric due to the LHC preferring positive charge initial

states. The maximum ratio of jet mass to  $p_T$  allows a handle to find jets which clustered together multiple decay products of a top quark, for example.

The variables were iteratively chosen from a larger pool of kinematic variables by selecting the most performant variables and retraining until the performance started to suffer.

Training was performed on simulation with a loosened SM  $t\bar{t}t\bar{t}$  baseline selection to prevent issues with training by increasing statistics:

- $N_b \geq 2$
- $H_T \geq 300$  GeV
- $p_T^{\text{miss}} > 50$  GeV
- $p_T(\ell_1) > 15$  GeV
- $p_T(\ell_2) > 15$  GeV

The raw discriminant values for signal and background separated into test and train sets is shown in Fig. 3.3. There is little to no overtraining observed.

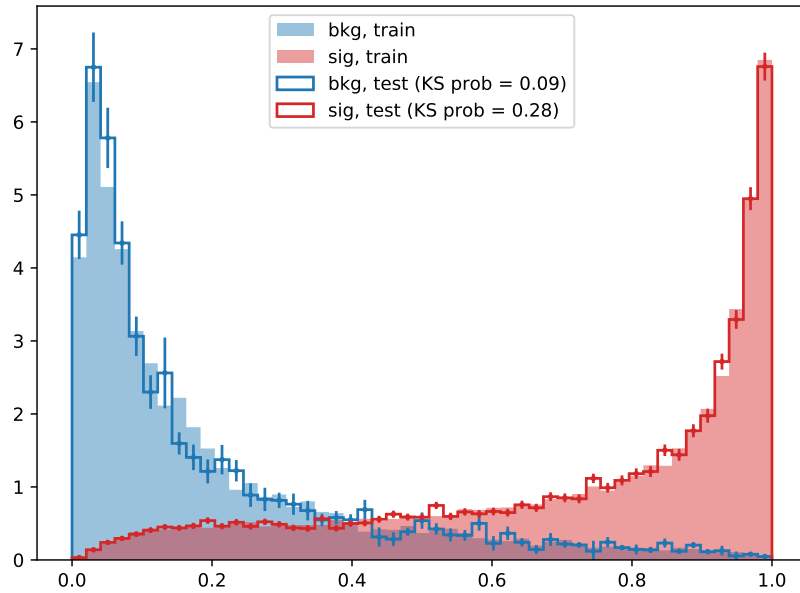


Figure 3.3: Raw discriminant values for training and testing sets.

## 3.7 Signal regions

### 3.7.1 SUSY analysis

Following the SUSY analysis baseline selection, we define six exclusive categories depending on the kinematics of event and the leptons:

- High-High SS pair (HH): exactly 2 leptons, both with  $p_T > 25\text{GeV}$ , and  $p_T^{\text{miss}} > 50\text{GeV}$ ;
- High-Low SS pair (HL): exactly 2 leptons, one with  $p_T > 25\text{GeV}$ , one with  $p_T < 25\text{GeV}$ , and  $p_T^{\text{miss}} > 50\text{GeV}$ ;
- Low-Low SS pair (LL): exactly 2 leptons, both with  $p_T < 25\text{GeV}$  and  $p_T^{\text{miss}} > 50\text{GeV}$ ;

- Low  $p_T^{\text{miss}}$  (LM): exactly 2 leptons, both with  $p_T > 25\text{GeV}$ , and  $p_T^{\text{miss}} < 50\text{GeV}$ ; and
- Multilepton with an on-shell Z boson (on-Z ML):  $\geq 3$  leptons, at least one with  $p_T > 25\text{GeV}$ ,  $p_T^{\text{miss}} > 50\text{GeV}$ ,  $\geq 1$  Z boson candidate formed by a pair of OS, same-flavor leptons with  $76 < m_{\ell\ell} < 106\text{GeV}$ .
- Multilepton without an on-shell Z boson (off-Z ML): same as on-Z ML but without a Z boson candidate.

For the on-Z ML category, the calculation of  $m_T^{\text{min}}$  uses leptons not forming the Z candidate.

The categories are structured to be generally sensitive to different SUSY models considered in the analysis. For example, the HH category gives sensitivity to many of the scenarios with large mass splittings between the gluino and lightest neutralino (T1tttt, T5ttbbWW, T5tttt, T5qqqqWW). Lower  $p_T$  threshold categories, HL and LL, provide sensitivity to smaller mass splittings, resulting in less energetic leptons. Models with Z bosons in the final state, such as T5qqqqWZ and T6ttHZ, will typically fall into the ML categories. The LM category captures events that otherwise would be lost due to the  $p_T^{\text{miss}} > 50\text{GeV}$  requirement in the HH, HL, and LL regions, and is particularly relevant for the T1qqqqL and T1tbs RPV models.

Within each category, many signal regions (SRs) are formed based on  $N_{\text{jets}}$ ,  $N_b$ ,  $H_T$ ,  $p_T^{\text{miss}}$ , SS charge,  $m_T^{\text{min}}$ . The SRs within the six categories, HH, HL, LL, LM, on-Z ML, and off-Z ML, are summarized in Tables 3.7, 3.8, 3.9, 3.10, 3.11 and 3.12, respectively.

$N_b$	$m_T^{\min}$	$p_T^{\text{miss}}$	$N_{\text{jets}}$	$H_T < 300$	[300, 1125]	[1125, 1300]	[1300, 1600]	> 1600			
0	<120	50–200	2–4	SR1	SR2	SR54 $N_{\text{jets}} < 5$	SR55 $N_{\text{jets}} < 5$	SR56 $N_{\text{jets}} < 5$			
			$\geq 5$	SR3	SR4						
		200–300	2–4		SR5 (++) / SR6 (--)						
			$\geq 5$		SR7						
			2–4		SR8 (++) / SR9 (--)						
	>120	50–200	$\geq 5$		SR10						
			2–4								
		200–300	$\geq 5$								
			2–4	SR13 (++) / SR14 (--)							
			$\geq 5$	SR11	SR12	SR57 $N_{\text{jets}} = 5, 6$	SR58 $N_{\text{jets}} = 5, 6$				
1	<120	50–200	2–4	SR15 (++) / SR16 (--)							
			$\geq 5$	SR17 (++) / SR18 (--)							
		200–300	2–4	SR19							
			$\geq 5$	SR20 (++) / SR21 (--)							
			2–4	SR22							
	>120	50–200	$\geq 5$								
			2–4								
		200–300	$\geq 5$								
2	<120	50–200	2–4	SR23	SR24	SR60 $N_{\text{jets}} > 6$	SR61 $N_{\text{jets}} > 6$	SR62 $N_{\text{jets}} > 6$			
			$\geq 5$	SR25 (++) / SR26 (--)	SR27 (++) / SR28 (--)						
		200–300	2–4		SR29 (++) / SR30 (--)						
			$\geq 5$		SR31						
			2–4		SR32 (++) / SR33 (--)						
	>120	50–200	$\geq 5$		SR34						
			2–4								
		200–300	$\geq 5$								
$\geq 3$	<120	50–200	2–4	SR35 (++) / SR36 (--)	SR37 (++) / SR38 (--)	SR60 $N_{\text{jets}} > 6$	SR61 $N_{\text{jets}} > 6$	SR62 $N_{\text{jets}} > 6$			
			$\geq 5$		SR39 (++) / SR40 (--)						
		200–300	2–4		SR37 (++) / SR38 (--)						
			$\geq 5$		SR39 (++) / SR40 (--)						
		>120	50–300	SR41	SR42 (++) / SR43 (--)						
			2–4		SR44 (++) / SR45 (--)						
			$\geq 5$		SR46 (++) / SR47 (--)						
			2–4	–	SR48 (++) / SR49 (--)						
			$\geq 5$		SR50 (++) / SR51 (--)						
Incl.	Incl.	300–500	2–4		SR52 (++) / SR53 (--)						
		>500	–								
		300–500	$\geq 5$								
		>500	–								

Table 3.7: The SR definitions for the HH category. Charge-split regions are indicated with (++) and (--) . The rightmost five columns represent a splitting in the  $H_T$  variable. The three highest  $H_T$  regions are split only by  $N_{\text{jets}}$ , resulting in 62 regions in total. Quantities are specified in units of GeV where applicable.

$N_b$	$m_T^{\min}$	$p_T^{\text{miss}}$	$N_{\text{jets}}$	$H_T < 300$	$H_T \in [300, 1125]$	$H_T \in [1125, 1300]$	$H_T > 1300$
0	<120	50–200	2–4	SR1	SR2	SR40 (++) / SR41 (--)	SR42 (++) / SR43 (--)
			$\geq 5$	SR3	SR4		
		200–300	2–4		SR5 (++) / SR6 (--)		
			$\geq 5$		SR7		
	1	50–200	2–4	SR8	SR9		
			$\geq 5$	SR10 (++) / SR11 (--)	SR12 (++) / SR13 (--)		
		200–300	2–4		SR14		
			$\geq 5$		SR15 (++) / SR16 (--)		
2	<120	50–200	2–4	SR17	SR18	SR40 (++) / SR41 (--)	SR42 (++) / SR43 (--)
			$\geq 5$	SR19 (++) / SR20 (--)	SR21 (++) / SR22 (--)		
		200–300	2–4		SR23 (++) / SR24 (--)		
			$\geq 5$		SR25		
$\geq 3$	<120	50–200	$\geq 2$	SR26 (++) / SR27 (--)	SR28 (++) / SR29 (--)	SR33 (++) / SR34 (--)	SR35 (++) / SR36 (--)
		200–300	$\geq 2$		SR30		
Inclusive	>120	50–300	$\geq 2$	SR31	SR32		
Inclusive	Inclusive	300–500	2–4	–	SR33 (++) / SR34 (--)		
		>500			SR35 (++) / SR36 (--)		
		300–500	$\geq 5$	–	SR37 (++) / SR38 (--)		
		>500			SR39		

Table 3.8: The SR definitions for the HL category. Charge-split regions are indicated with (++) and (--) . There are 43 regions in total. Quantities are specified in units of GeV where applicable.

$N_b$	$m_T^{\min}$	$H_T$	$p_T^{\text{miss}} \in [50, 200]$	$p_T^{\text{miss}} > 200$
0	<120	>400	SR1	SR2
1			SR3	SR4
2			SR5	SR6
$\geq 3$			SR7	
Inclusive	>120		SR8	

Table 3.9: The SR definitions for the LL category. All SRs in this category require  $N_{\text{jets}} \geq 2$ . There are 8 regions in total. Quantities are specified in units of GeV where applicable.

$N_b$	$N_{\text{jets}}$	$H_T \in [300, 1125]$	$H_T \in [1125, 1300]$	$H_T > 1300$
0	2–4	SR1	SR8 ( $N_{\text{jets}} < 5$ )	SR10 ( $N_{\text{jets}} < 5$ )
	$\geq 5$	SR2		
1	2–4	SR3	SR9 ( $N_{\text{jets}} \geq 5$ )	SR11 ( $N_{\text{jets}} \geq 5$ )
	$\geq 5$	SR4		
2	2–4	SR5		
	$\geq 5$	SR6		
$\geq 3$	$\geq 2$	SR7		

Table 3.10: The SR definitions for the LM category. All SRs in this category require  $p_T^{\text{miss}} < 50\text{GeV}$  and  $H_T > 300\text{GeV}$ . The two high- $H_T$  regions are split only by  $N_{\text{jets}}$ , resulting in 11 regions in total. Quantities are specified in units of GeV where applicable.

$N_b$	$H_T$	$p_T^{\text{miss}} \in [50, 150]$	$p_T^{\text{miss}} \in [150, 300]$	$p_T^{\text{miss}} \geq 300$
0	<400	SR1/SR2 <sup>†</sup>	SR3/SR4 <sup>†</sup>	SR22/SR23 <sup>†</sup>
	400–600	SR5/SR6 <sup>†</sup>	SR7/SR8 <sup>†</sup>	
1	<400	SR9	SR10	SR22/SR23 <sup>†</sup>
	400–600	SR11	SR12	
2	<400	SR13	SR14	
	400–600	SR15	SR16	
$\geq 3$	<600	SR17		
Inclusive	$\geq 600$	SR18/SR19 <sup>†</sup>	SR20/SR21 <sup>†</sup>	

Table 3.11: The SR definitions for the on-Z ML category. All SRs in these categories require  $N_{\text{jets}} \geq 2$ . Regions marked with <sup>†</sup> are split by  $m_T^{\text{min}} = 120\text{GeV}$ , with the high- $m_T^{\text{min}}$  region specified by the second SR label. There are 23 regions in total. Quantities are specified in units of GeV where applicable.

$N_b$	$H_T$	$p_T^{\text{miss}} \in [50, 150]$	$p_T^{\text{miss}} \in [150, 300]$	$p_T^{\text{miss}} \geq 300$
0	<400	SR1/SR2 <sup>†</sup>	SR3/SR4 <sup>†</sup>	SR20/SR21 <sup>†</sup>
	400–600	SR5	SR6	
1	<400	SR7	SR8	SR20/SR21 <sup>†</sup>
	400–600	SR9	SR10	
2	<400	SR11	SR12	SR20/SR21 <sup>†</sup>
	400–600	SR13	SR14	
$\geq 3$	<600	SR15		
Inclusive	$\geq 600$	SR16/SR17 <sup>†</sup>	SR18/SR19 <sup>†</sup>	

Table 3.12: The SR definitions for the off-Z category. All SRs in these categories require  $N_{\text{jets}} \geq 2$ . Regions marked with <sup>†</sup> are split by  $m_T^{\text{min}} = 120\text{GeV}$ , with the high- $m_T^{\text{min}}$  region specified by the second SR label. There are 21 regions in total. Quantities are specified in units of GeV where applicable.

### 3.7.2 SM $t\bar{t}t\bar{t}$ analysis

Events passing the SM  $t\bar{t}t\bar{t}$  baseline selection are split into several signal and control regions, following two independent approaches. In the first approach, the variables  $N_{\text{jets}}$ ,  $N_b$ , and  $N_\ell$  are used to subdivide events into 14 mutually exclusive SRs and a CR enriched in  $t\bar{t}W$  background (CRW), to complement the CRZ, as detailed in Table 3.13.

In the BDT approach, the CRZ is the only control region, and the remaining events are subdivided into 17 SRs by discretizing the discriminant output of the BDT trained to separate  $t\bar{t}t\bar{t}$  events from the sum of the SM backgrounds.

At this point, it's worth noting that three of the most performant input variables for the BDT,  $N_{\text{jets}}$ ,  $N_b$ , and  $N_\ell$ , already correspond to the variables used for the cut-based analysis.

$N_\ell$	$N_b$	$N_{\text{jets}}$	Region
2	2	$\leq 5$	CRW
		6	SR1
		7	SR2
		$\geq 8$	SR3
	3	5	SR4
		6	SR5
		7	SR6
		$\geq 8$	SR7
	$\geq 4$	$\geq 5$	SR8
$\geq 3$	2	5	SR9
		6	SR10
		$\geq 7$	SR11
	$\geq 3$	4	SR12
		5	SR13
		$\geq 6$	SR14
Inverted resonance veto			CRZ

Table 3.13: Definition of the 14 SRs and two CRs for the cut-based analysis.

# Chapter 4

## Background estimation

There are three main classes of backgrounds that survive the inclusive SUSY or SM  $t\bar{t}t\bar{t}$  analysis baseline selections: backgrounds with two or more prompt leptons in the final state (giving a real SS pair), backgrounds with at least one nonprompt lepton, and backgrounds that actually have an OS pair with one lepton having misreconstructed charge.

The first class of backgrounds produce prompt leptons but are relatively “rare” (have low cross section) and are estimated from simulation, with appropriate correction factors and uncertainties to be discussed in the next sections. This class can be further subdivided by the physical process:

- **Diboson:**

$WZ$ ,  $ZZ$ ,  $WW$ ,  $WH$ ,  $ZH$ ,  $Z\gamma$ ,  $W\gamma$ , and  $W^\pm W^\pm$

- **Triboson:**

$WWW$ ,  $WWZ$ ,  $WZZ$ ,  $ZZZ$ ,  $WW\gamma$ , and  $WZ\gamma$

- **Single top quark and bosons:**

$t\gamma$ ,  $tZ\gamma$ , and  $tWZ$

- **Top quark pair and one boson:**

$t\bar{t}W$ ,  $t\bar{t}Z$ ,  $t\bar{t}H$ , and  $t\bar{t}\gamma$

- **Top quark pair and two bosons:**

$t\bar{t}WW$ ,  $t\bar{t}WZ$ ,  $t\bar{t}ZZ$ ,  $t\bar{t}WH$ ,  $t\bar{t}ZH$ , and  $t\bar{t}HH$

- **Triple top quark:**

$t\bar{t}t$  and  $t\bar{t}tW$

- **Four top quarks:**

$t\bar{t}t\bar{t}$

In the SM  $t\bar{t}t\bar{t}$  analysis,  $t\bar{t}t\bar{t}$  is, of course, considered a signal instead of a background.

Contributions from the first two categories of physical processes are negligible for the SM  $t\bar{t}t\bar{t}$  analysis due to the  $N_b \geq 2$  requirement in the baseline selections.

The second class of background events consist of events where one of the leptons is “nonprompt”, or more colloquially, “fake”. That is, the fake lepton is either a real lepton which is a decay product of a heavy flavor hadron (b or c quark), or simply a misidentified hadron. The dominant sources of fake leptons are the large cross section processes of  $t\bar{t}+{\rm jets}$  and  $W+{\rm jets}$ . This class is more tricky to only use simulation, and a data-driven method is used instead.

The last class of backgrounds consists of those with a charge-misidentified lepton, or, more colloquially “flips”, which essentially converts an OS pair into a SS pair. Thus, the biggest source of this background is the highest cross-section OS process: DY. Similarly to the nonprompt background, this background uses a data-driven method instead of relying completely on simulation.

## 4.1 Prompt SM

The large set of physics processes listed in the previous section as prompt SM processes are estimated from simulation and are grouped into larger categories, singling out specific processes which are important to either the inclusive SUSY analysis or the SM  $t\bar{t}t\bar{t}$  analysis. The process categories and constituent physics processes/simulations are:

- “ $t\bar{t}W$ ”:  $t\bar{t}W$
- “ $t\bar{t}Z$ ”:  $t\bar{t}Z$
- “ $t\bar{t}H$ ”:  $t\bar{t}H$
- “ $X\gamma$ ”:  $W\gamma$ ,  $Z\gamma$ ,  $t\bar{t}\gamma$ , and  $t\gamma$

And for the SM  $t\bar{t}t\bar{t}$  analysis, there are two additional categories:

- “**Rare**”:  $t\bar{t}t$ ,  $t\bar{t}tW$ ,  $ZZ$ ,  $WH$ ,  $ZH$ ,  $WZ\gamma$ ,  $WW\gamma$ ,  $tZ\gamma$ ,  $tWZ$ ,  $W^\pm W^\pm$ ,  $WZ$ , and  $WW$
- “ $t\bar{t}VV$ ”:  $t\bar{t}WW$ ,  $t\bar{t}WZ$ ,  $t\bar{t}ZZ$ ,  $t\bar{t}WH$ ,  $t\bar{t}ZH$ , and  $t\bar{t}HH$

Or, for the inclusive SUSY analysis, there are three additional categories:

- “**Rare**”:  $t\bar{t}t$ ,  $t\bar{t}tW$ ,  $ZZ$ ,  $WW$ ,  $WH$ ,  $ZH$ ,  $WZ\gamma$ ,  $WW\gamma$ ,  $tZ\gamma$ ,  $tWZ$ ,  $t\bar{t}WW$ ,  $t\bar{t}WZ$ ,  $t\bar{t}ZZ$ ,  $t\bar{t}WH$ ,  $t\bar{t}ZH$ ,  $t\bar{t}HH$ , and  $t\bar{t}t\bar{t}$
- “**WZ**”:  $WZ$
- “**WW**”:  $W^\pm W^\pm$

Two important processes for the SM  $t\bar{t}t\bar{t}$  search are  $t\bar{t}W$  and  $t\bar{t}Z$ , which have cross sections of  $630 \text{ fb}^{-1}$  and  $840 \text{ fb}^{-1}$  [53], respectively, almost a couple orders of magnitude larger than that of  $t\bar{t}t\bar{t}$  ( $12 \text{ fb}^{-1}$ ).

A breakdown of the individual processes of the “Rare” category in the SM  $t\bar{t}t\bar{t}$  analysis signal regions is shown in Figure 4.1, split into multi-top quark and multi-boson processes.

Since many of these processes have not been experimentally observed or measured, we apply conservative normalization uncertainties based on theoretical calculations of 50% on Rare and  $X\gamma$  categories for the SUSY analysis, or 30% for other categories.

For the SM  $t\bar{t}t\bar{t}$  analysis, we apply uncertainties of 20%, 11%, and 11% for Rare,  $X\gamma$ , and  $t\bar{t}VV$  categories, respectively, and 40% for the  $t\bar{t}W$  and  $t\bar{t}Z$  categories. Also in the SM  $t\bar{t}t\bar{t}$  analysis, the  $t\bar{t}H$  category is assigned an uncertainty of 25% to reflect the CMS  $t\bar{t}H$  measurement [54] which obtained a signal strength  $\mu_{t\bar{t}H}$ , defined as the ratio between the measured  $t\bar{t}H$  cross section and its SM expectation, of  $1.26^{+0.31}_{-0.26}$ .

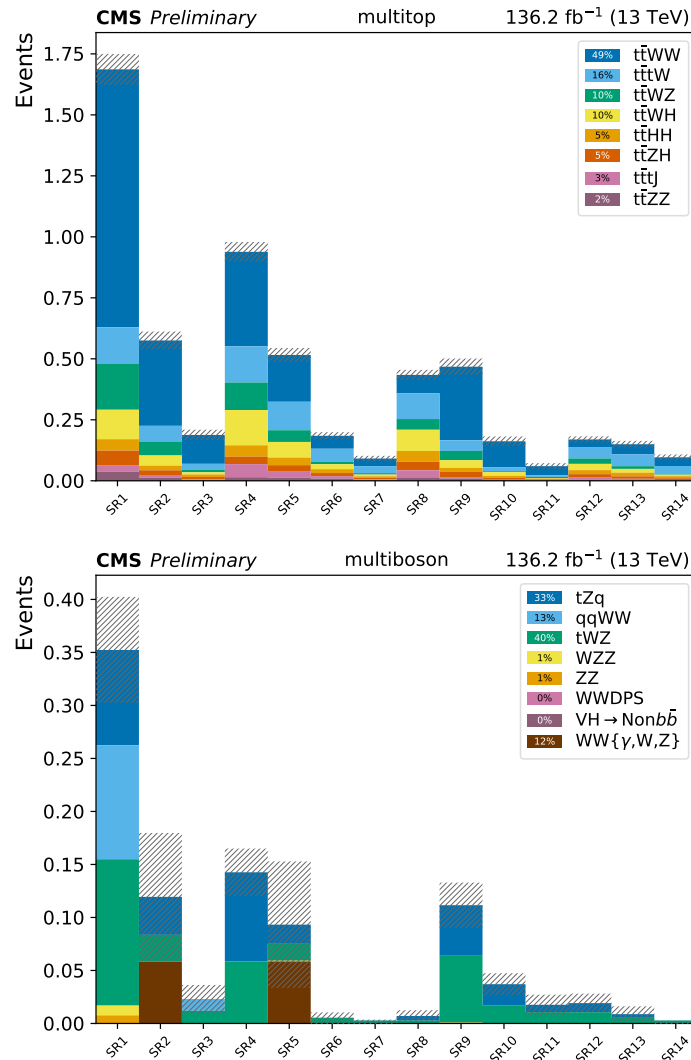


Figure 4.1: Relative composition of multi-top (top) and multi-boson (bottom) rare backgrounds in the signal regions for all MC using the kinematic selection and signal region definitions from Section 3.7.2.

## 4.2 Nonprompt leptons

Estimating the background from fake leptons requires care as simply using fake leptons out of the box from simulation makes heavy assumptions on the accuracy of the simulation. It is better to somehow use data itself to estimate the fake leptons from data. We use the “fake rate”, or “tight-loose”, method to estimate this background in a data-driven fashion via an extrapolation.

Recalling the two working points for lepton identification/isolation, loose and tight, we use an orthogonal sideband (“application region”) of tight-loose-not-tight SS dilepton events (where one lepton is tight and the other is loose but not tight) to estimate the fake contribution in the SRs (tight-tight SS dilepton events).

The application region events can be weighted by a “tight-to-loose” ratio (the probability for a loose non-prompt lepton to also pass the tight lepton selections) to form the SR prediction. Defining  $f$  as this probability, the fake contribution in the SRs,  $N_{\text{TT, fake}}$  is given by

$$N_{\text{TT, fake}} = \left( \frac{f}{1-f} \right) N_{\text{TL}} - \left( \frac{f}{1-f} \right)^2 N_{\text{LL}} \quad (4.1)$$

where  $N_{\text{TL}}$  represents the number of events in the application region and  $N_{\text{LL}}$  represents a similar, but smaller, application region where both leptons pass the loose lepton selections but not the tight selections. The probability  $f$  is parameterized by a modified lepton  $p_T$  ( $p_T^{\text{corr}}$ ), lepton  $\eta$ , lepton flavor ( $e$  or  $\mu$ ), data collection year, and trigger strategy (isolated, non-isolated). The minus sign is needed for this “double fake” contribution

to avoid overcounting (since both tight-loose and loose-tight events are present in the application region and are extrapolated to the signal regions).

Now, unsurprisingly,  $f \equiv f(p_T^{\text{corr}}, \eta)$  is measured in the “measurement region”. The measurement region is a sample of QCD multijet events, and thus, enriched in non-prompt leptons, with an event selection of

- specific auxiliary trigger, listed in Table 3.4
- only one loose/denominator lepton (“fakeable object”/“FO”)
- at least one jet with  $\Delta R(\text{jet}, \text{FO}) > 1$
- $p_T^{\text{miss}} < 20\text{GeV}$
- $M_T < 20\text{GeV}$

to make sure we select as much QCD in data in possible while minimizing the amount of prompt leptons leaking into the measurement region. Due to different trigger requirements and data collection periods, we derive a total of 12 versions of the 2-dimensional  $p_T$ - $\eta$ -binned fake rate (electrons/muons, isolated triggers/non-isolated triggers, 2016/2017/2018)

We use a corrected lepton  $p_T$ ,  $p_T^{\text{corr}}$ , to parameterize the fake rate estimation in the fake rate estimation in order to reduce the dependency to the mother parton  $p_T$  and the flavor composition of the sample [55]:

$$p_T^{\text{corr}} = \begin{cases} p_T \cdot (1 + \max(0, I_{\text{mini}} - I_1)) & \text{if } p_T^{\text{rel}} > I_3 \\ \max(p_T, p_T(\text{jet}) \cdot I_2) & \text{if } p_T^{\text{rel}} \leq I_3 \end{cases} \quad (4.2)$$

While the requirements on  $p_T^{\text{miss}}$  and  $M_T$  suppress the contribution from prompt leptons in the measurement region, residual contributions from DY/ $W+\text{jets}/t\bar{t}+\text{jets}$  (electroweak contamination) need to be estimated and subtracted properly from the fake rate. For this, we use simulation, but normalize in a high  $M_T/p_T^{\text{miss}}$  region. Since the fake rate  $f$  is the ratio of the number of tight leptons to the number of loose leptons ( $f = N_T/N_L$ ) in the measurement region, we need to calculate  $k$  for this region ( $M_T > 30\text{GeV}$ ,  $p_T^{\text{miss}} > 30\text{GeV}$ ) region and subtract from the numerator and denominator:

$$f = \frac{N_T - k \cdot N_T^{\text{EWK}}}{N_L - k \cdot N_L^{\text{EWK}}} \quad (4.3)$$

where  $N^{\text{EWK}}$  represents the electroweak contamination. These correction factors,  $k$ , are obtained by fitting the sum of two templates derived from MC, one for QCD and one for the sum of electroweak processes (DY,  $W+\text{jets}$ ,  $t\bar{t}+\text{jets}$ ). The normalization of the electroweak processes is extracted from the fit and yields  $k$ . Since the shape of the non-prompt component might not be well-modeled, we perform a cross-check by repeating the fit and replacing the QCD MC template with a data-drive template from events failing the isolation requirements. The nominal and alternative fits for electrons and muons are shown in Fig. 4.2 for 2017 data with isolated triggers, for example. The resulting normalization corrections for the full set of years and both trigger types are shown in Table 4.1.

Two-dimensional fake rate maps for isolated triggers for 2017 data and QCD simulation are shown in Fig. 4.3. One can see that prior to the electroweak subtraction, the

fake rates increase drastically at high lepton  $p_T$ . This is expected, as the probability for true/prompt leptons from electroweak processes to pass the tight selection is large (Otherwise our lepton selections would not be doing their job in the first place.) To better visualize the fake rates, one-dimensional projections onto the  $p_T^{\text{corr}}$  axis for each of the three years are shown in Figs. 4.4, 4.5, and 4.6. One sees good agreement between the data-driven fake rate and fake rate calculated directly with QCD MC, though this is not at all expected or needed. Also note the large uncertainties at high  $p_T^{\text{corr}}$ , which is due to the uncertainty associated with the electroweak subtraction procedure.

		isolated triggers		non-isolated triggers	
		$e$	$\mu$	$e$	$\mu$
2016	MC template	1.240	1.189	1.258	1.164
	data template	1.294	1.154	1.337	1.131
2017	MC template	1.215	1.222	1.208	1.202
	data template	1.277	1.195	1.298	1.178
2018	MC template	1.216	1.277	1.195	1.286
	data template	1.285	1.247	1.300	1.249

Table 4.1: Normalization scale factors for electroweak samples derived with two different  $M_T$  templates for QCD: MC and data (the data template refers to the inverted isolation region).

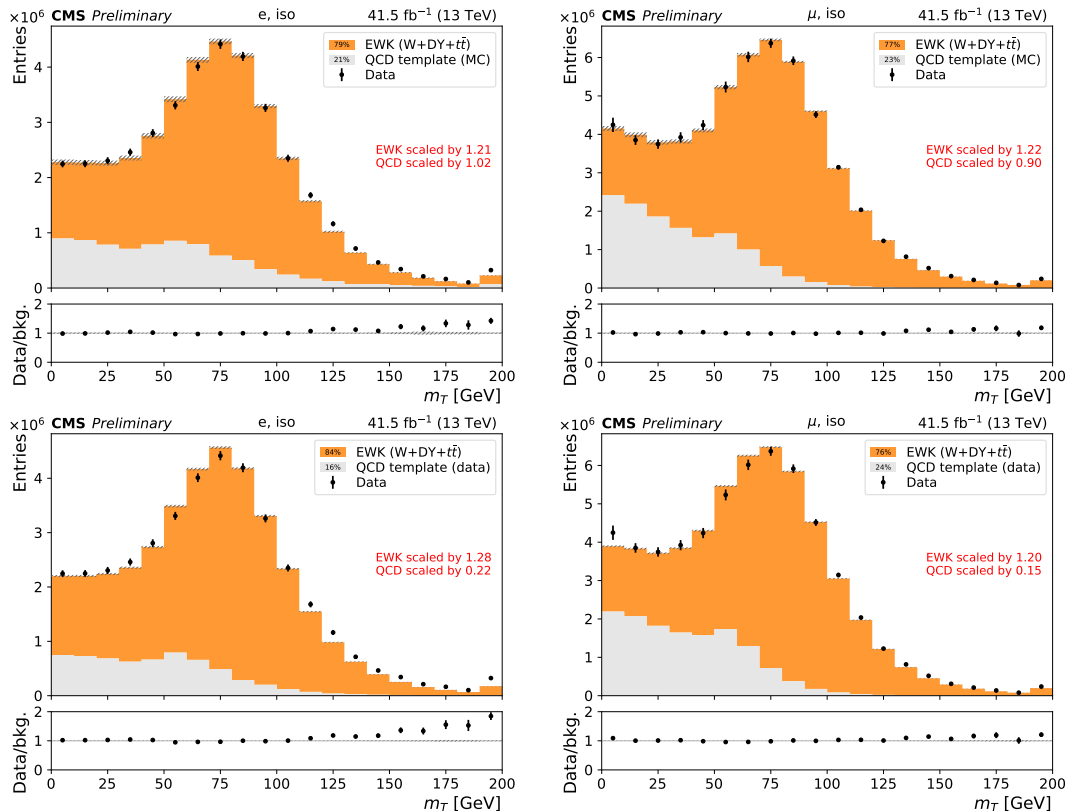


Figure 4.2: Fitted  $M_T$  distribution used to derive the normalization of electroweak samples (DY,  $W+\text{jets}$ ,  $t\bar{t}+\text{jets}$ ) in the fake rate measurement region. Electrons are shown on the left, muons on the right. From top to bottom, the results from the nominal selection ( $p_T^{\text{miss}} > 30 \text{ GeV}$  and lepton  $p_T > 20 \text{ GeV}$ ) with the QCD MC template and alternative data QCD template are shown. Data and MC conditions correspond to isolated triggers in 2017.

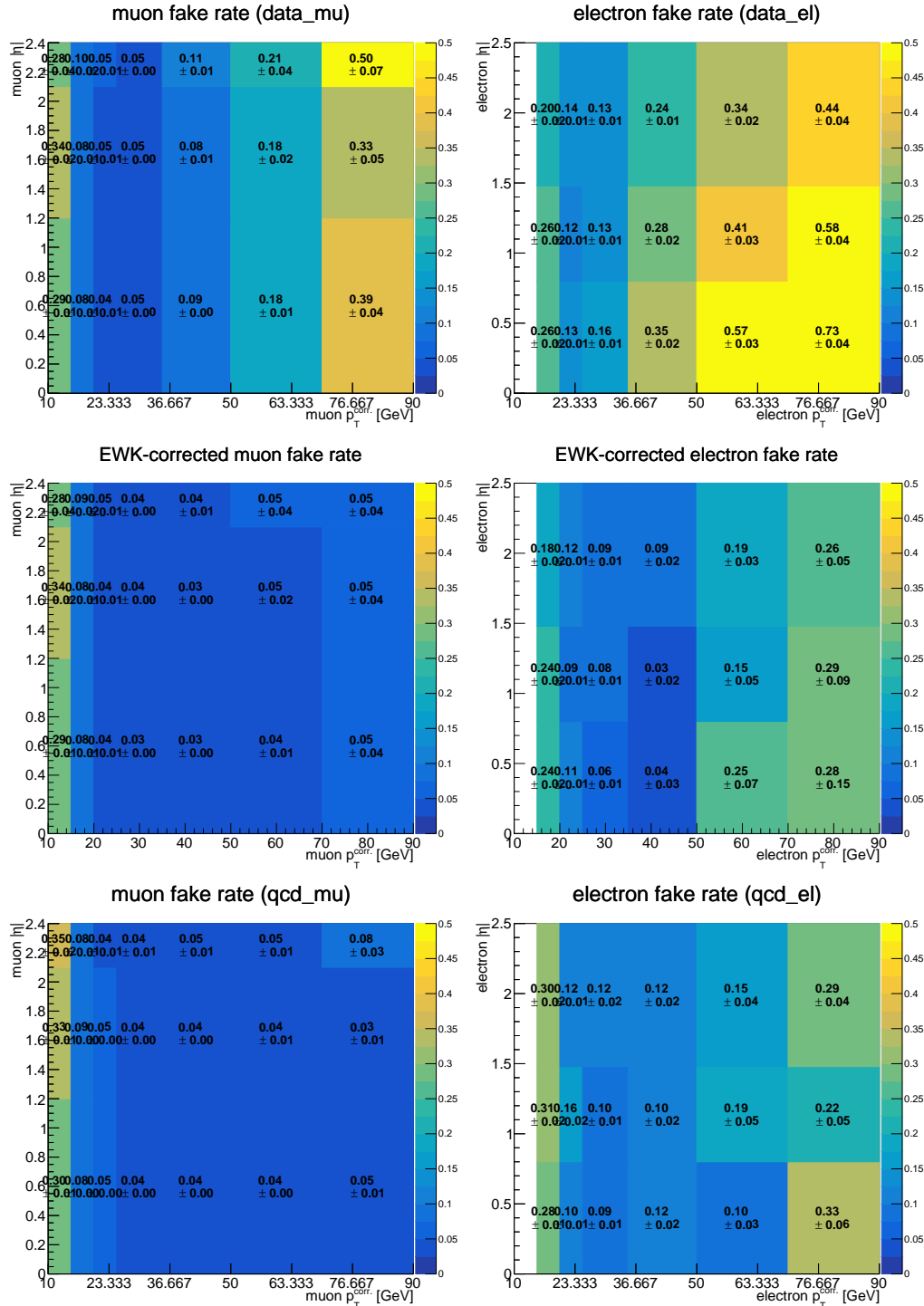


Figure 4.3: Two-dimensional fake rate maps for isolated triggers for muons (left) and electrons (right), for 2017 data uncorrected (top), 2017 data corrected for electroweak contamination (middle) and 2017 QCD simulation (bottom).

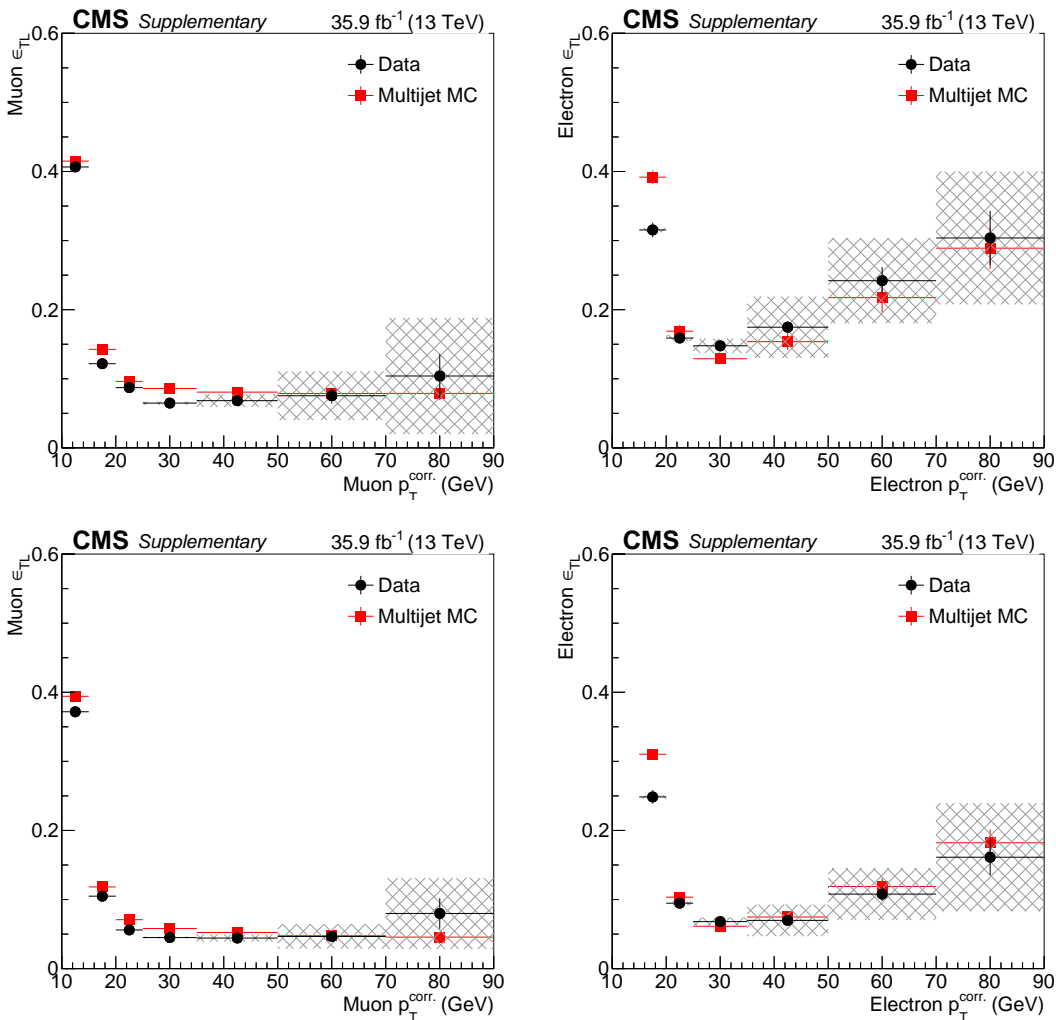


Figure 4.4: Electroweak contamination-corrected data fake rate projected vs  $p_T$  for 2016 data (black) and 2016 QCD simulation (red), for muons (left) and electrons (right). Isolated triggers are on top and non-isolated triggers on bottom. The shaded band in the projection is the systematic uncertainty related to the electroweak contamination.

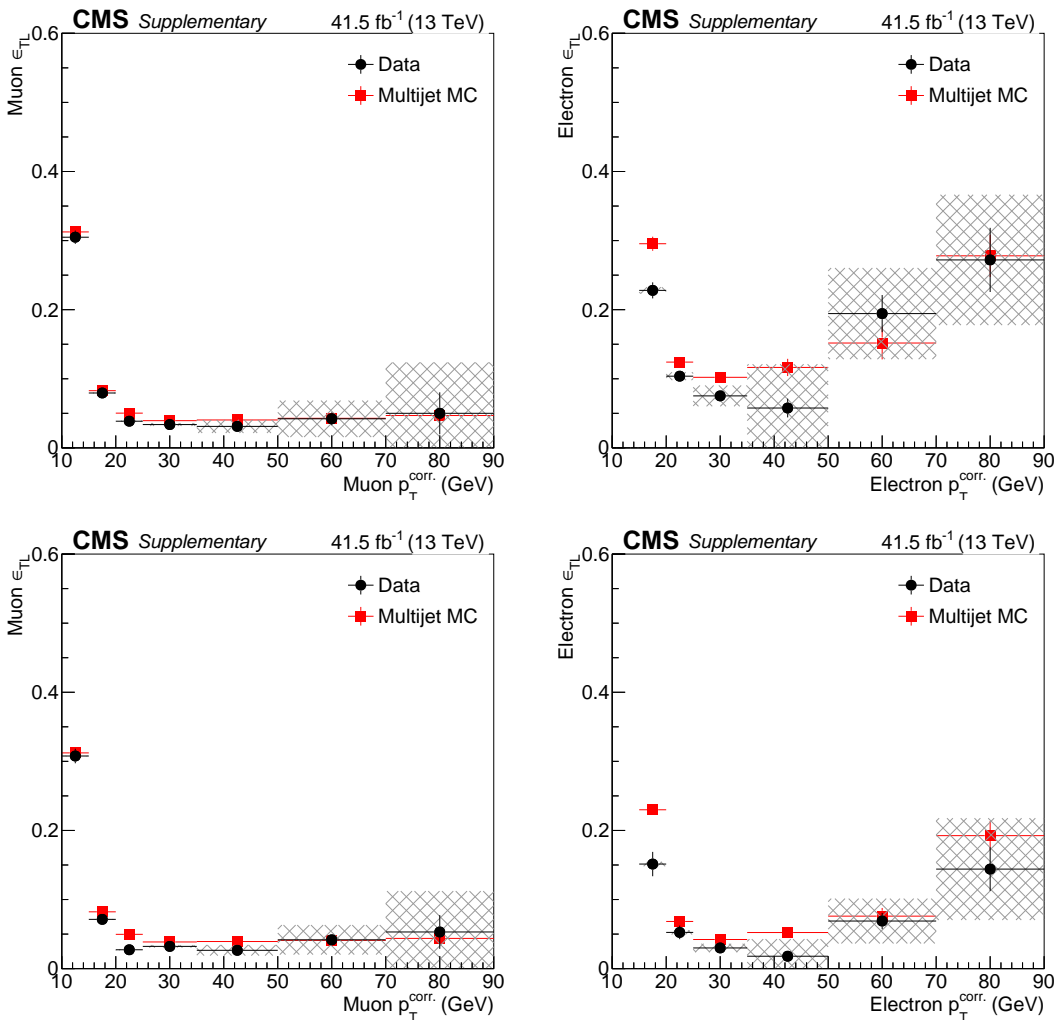


Figure 4.5: Electroweak contamination-corrected data fake rate projected vs  $p_{\text{T}}$  for 2017 data (black) and 2017 QCD simulation (red), for muons (left) and electrons (right). Isolated triggers are on top and non-isolated triggers on bottom. The shaded band in the projection is the systematic uncertainty related to the electroweak contamination.

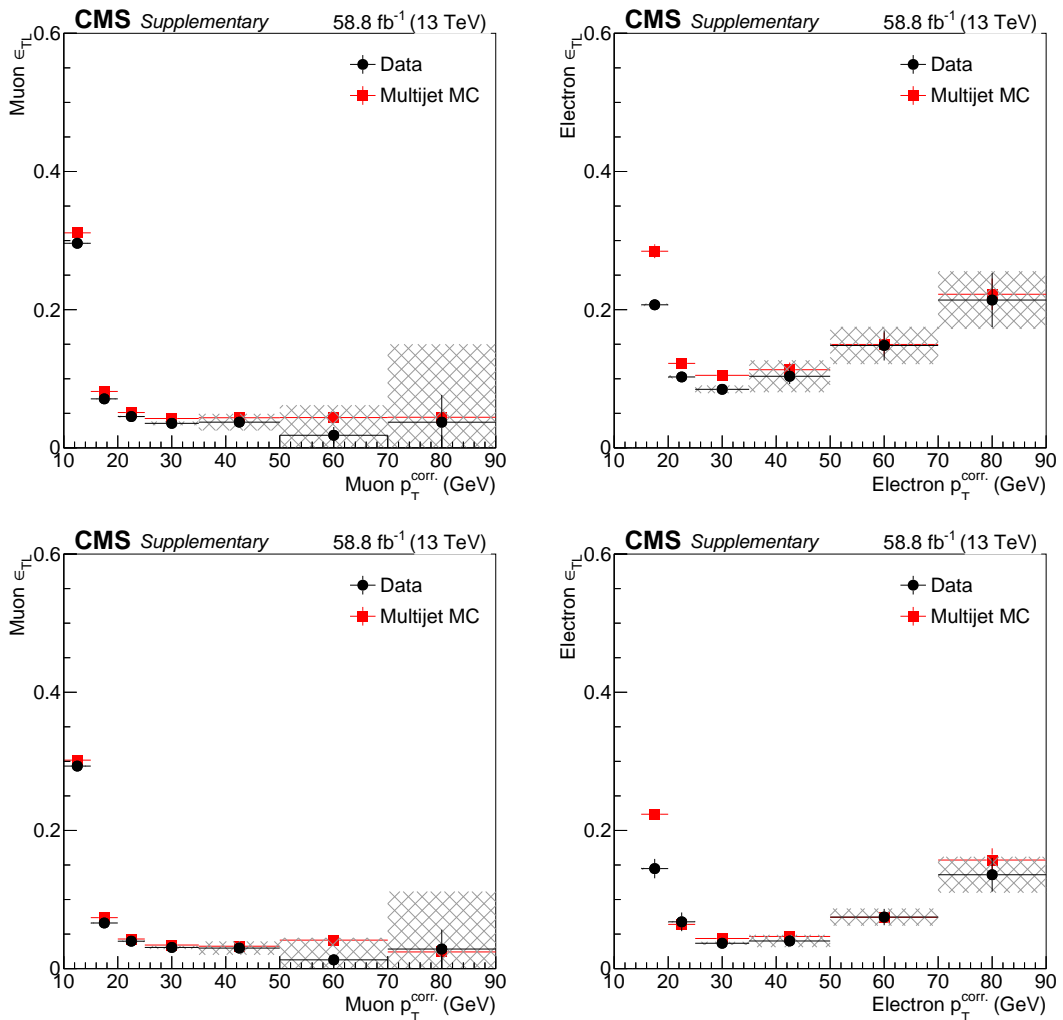


Figure 4.6: Electroweak contamination-corrected data fake rate projected vs  $p_T$  for 2018 data (black) and 2018 QCD simulation (red), for muons (left) and electrons (right). Isolated triggers are on top and non-isolated triggers on bottom. The shaded band in the projection is the systematic uncertainty related to the electroweak contamination.

We test the closure of this method in simulation after making the inclusive SUSY analysis baseline selection for various kinematic distributions in Fig. 4.7. The filled histograms are events with one lepton matched to a prompt lepton at generator lepton and another lepton not matched to a prompt lepton (prompt-nonprompt events), separately for  $t\bar{t}$ +jets and  $W$ +jets simulation samples. The histogram with black points represents application region events (one tight lepton and one loose-not-tight lepton, at reconstruction-level) which are reweighted by the fake rate transfer factor to form a prediction. The level of closure observed in the plots is typically at 30% or better, motivating a corresponding 30% normalization systematic uncertainty on the nonprompt lepton background.

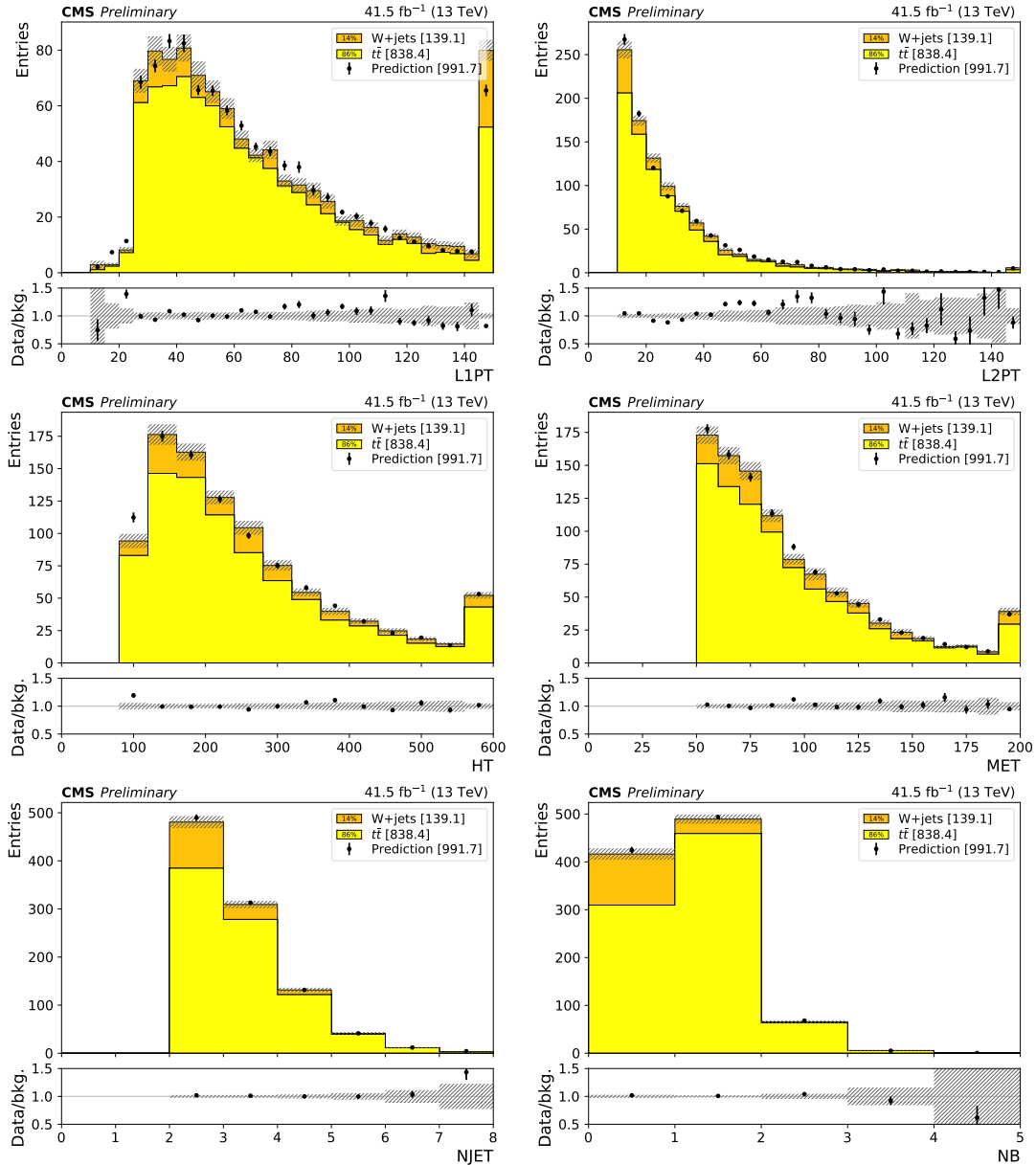


Figure 4.7: Electron+muon fake rate closure for QCD measurement in simulation. From left to right and top to bottom, the distributions are leading lepton  $p_T$ , sub-leading lepton  $p_T$ ,  $H_T$ ,  $p_T^{\text{miss}}$ ,  $N_{\text{jets}}$ , and  $N_b$ .

## 4.3 Charge misidentification

The charge misidentification/flip background results from events that have isolated OS leptons where the charge of one of the leptons is misidentified due to mismeasurement (typical at high  $p_T$ ) or bremsstrahlung. Muons are relatively well-measured and less susceptible to radiation due to their mass, so charge flips of muons are neglected compared to electrons.

The charge flip background is estimated by selecting OS  $ee$  or  $e\mu$  events which pass the appropriate baseline selection depending on analysis, and then weighting the events by the  $p_T$  and  $\eta$ -dependent probability of electron charge mismeasurement, which is calculated from simulation.

The two-dimensional probability maps, shown for each of the three years of data collection in Fig. 4.8, are obtained from a combination of  $t\bar{t}$  and DY simulation. The probabilities are then validated using a control sample in data of SS  $Z \rightarrow e^\pm e^\pm$  baseline events, instead using a  $p_T^{\text{miss}} < 50\text{GeV}$  requirement to be orthogonal to the signal regions. The level of disagreement in this control region is used to assess the associated systematic uncertainty and to derive a correction to the MC-based rate estimation. In the 2016 data sample, we find good agreement between prediction and data in the control region. However, in the 2017 and 2018 data samples, the MC-based flip rate is significantly lower than for 2016 due to the upgraded pixel detector (which added an extra inner pixel layer), so the observed number of events in the SS  $Z \rightarrow e^\pm e^\pm$  region is found to be nearly 40% higher than the predicted number of events. Consequently, the 2017 and 2018 charge flip

predictions are scaled up by approximately 40%, as seen in Figure 4.9. These year-by-year correction factors are summarized in Table 4.2. Since we do not observe significant trends in the lepton kinematics, we do not consider  $p_T$  and  $\eta$ -binned corrections on top of the tabulated flat correction factors. In addition to the statistical uncertainties, we apply a 20% systematic uncertainty on this background prediction for all years. In MC, the flip rate for muons is found to be an order of magnitude smaller than for electrons and is therefore neglected, as it would in any case be covered by the systematic uncertainty of 20% on this background.

year	observation/prediction
2016	1.01
2017	1.44
2018	1.41

Table 4.2: Ratio of observed flip rate in data to the flip rate prediction from simulation. These are the multiplicative correction to the MC-based charge flip probabilities.

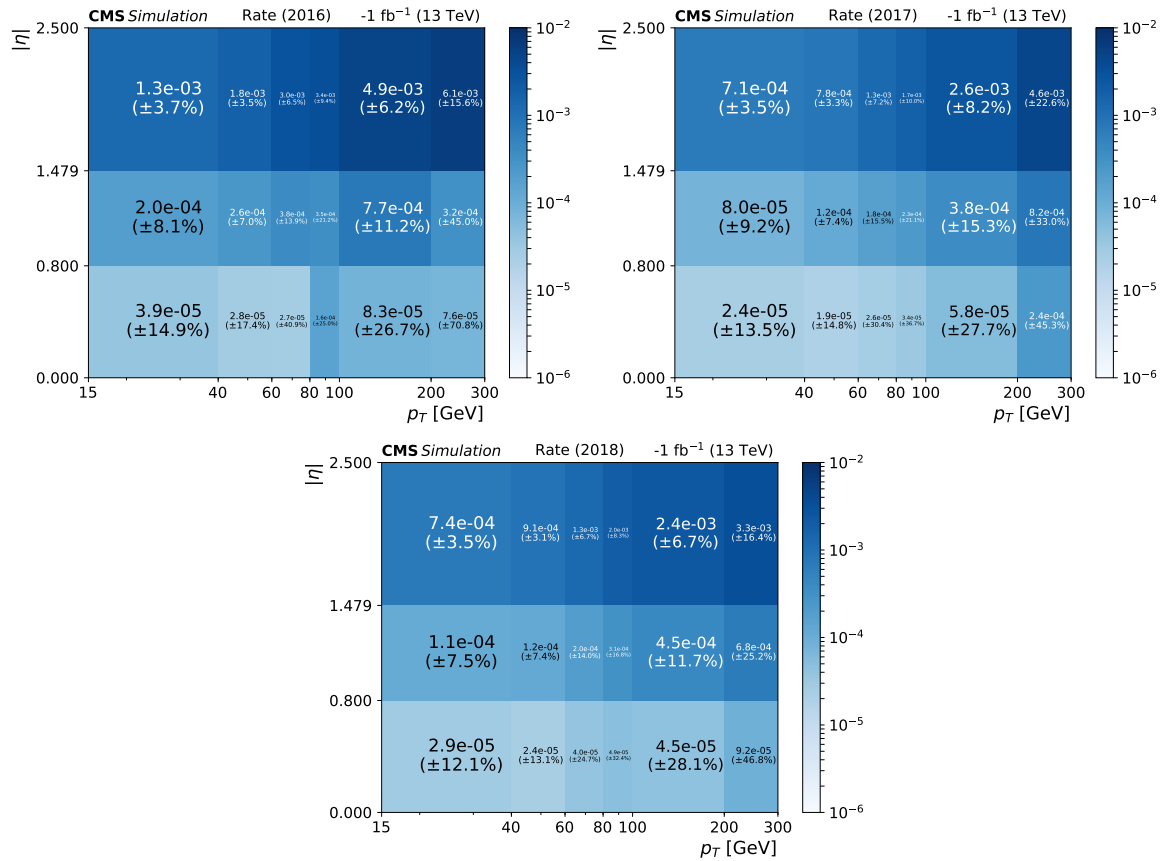


Figure 4.8: Electron charge flip rate for 2016, 2017, and 2018.

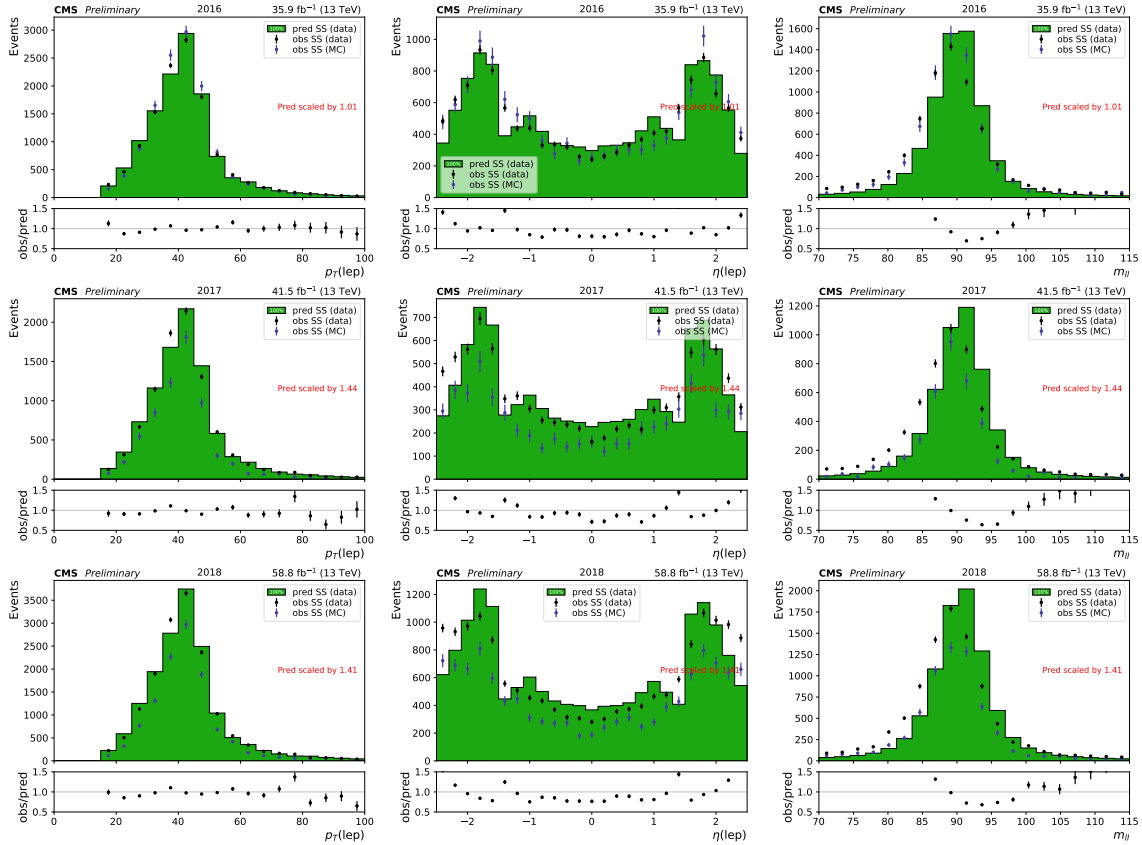


Figure 4.9: Predicted and observed lepton  $p_T$  (left) and  $\eta$  (middle) and  $m_{\ell\ell}$  (right) in a SS  $Z \rightarrow e^\pm e^\pm$  peak for the years 2016, 2017, and 2018, from top to bottom. The prediction is normalized to the observed data with the normalization factor inset in red. The filled green histogram consists of predicted charge flip events (reweighted OS events), the black points consist of observed charge flip events in data (SS), and the blue points show the observed charge flip events in MC (SS).

## 4.4 Corrections

In addition to corrections associated with JEC, b-tagging, lepton scale factors, and trigger scale factors, mentioned throughout previous sections and chapters, we apply two more dedicated corrections to simulation to bring better agreement between data and simulation. Both corrections deal with  $N_{\text{jets}}$  and  $N_b$  for the  $t\bar{t}W$ ,  $t\bar{t}Z$ , and  $t\bar{t}H$  processes, whose distributions need to be estimated correctly at high multiplicities, which is especially important for the SM  $t\bar{t}t\bar{t}$  analysis, as these are the leading background processes.

### 4.4.1 Gluon splitting

The  $t\bar{t}W$ ,  $t\bar{t}Z$ , and  $t\bar{t}H$  processes need an additional source of b quarks in order to populate the  $N_b \geq 3$  bins of the SM  $t\bar{t}t\bar{t}$  analysis, as they should only have up to 2 hard b jets from the  $t\bar{t}$  decay. If simulation does not model the gluon splitting process  $g \rightarrow b\bar{b}$ , the contributions in these high  $N_b$  bins can be drastically wrong. In fact, Ref. [56] measures that the ratio of cross sections of  $t\bar{t}b\bar{b}$  to  $t\bar{t}jj$  is about  $1.7 \pm 0.6$  times as high in data compared to simulation. As a result, events with additional b quarks in these three background processes are scaled up by a factor of  $1.7 \pm 0.6$  and the uncertainty is translated into a systematic uncertainty affecting analysis results.

#### 4.4.2 ISR/FSR jet multiplicity

Similarly,  $t\bar{t}W$  and  $t\bar{t}Z$  processes need an additional source of jets in order to populate the  $N_{\text{jets}} \geq 4$  bins of the analyses. To improve on the modeling of the multiplicity of additional jets from initial-state radiation (ISR) and final-state radiation (FSR) in MadGraph,  $t\bar{t}W$  and  $t\bar{t}Z$  MC events are reweighted based on the number of ISR or FSR jets ( $N_{\text{jets}}^{\text{ISR/FSR}}$ ). The  $t\bar{t}H$  process is not considered for this reweighting as the  $H \rightarrow WW^*$  decay will result in extra jets from one of the W bosons.

The reweighting method, developed in Ref. [57] for 2016 simulation samples, is based on the Data/MC ratio in the light-flavor jet multiplicity in dilepton  $t\bar{t}$  events (using MadGraph MC), as shown in Figure 4.10 for the 2017 and 2018 simulation samples. The method requires exactly two b-tagged jets, and assumes that all other jets are ISR or FSR. The reweighting factors vary within the range of  $[0.77, 1.46]$  for  $N_{\text{jets}}^{\text{ISR/FSR}}$  between 1 and 4. The corresponding Data/MC ratios are shown in Figure 4.10, where the different plots are based on different number of partons simulated at the matrix element.

We take one half of the deviation from unity as the systematic uncertainty in these reweighting factors. The size of the systematic comes from deviations observed in an orthogonal single-lepton channel. We make a tight single-lepton selection with tight lepton  $p_T > 25\text{GeV}$ ,  $p_T^{\text{miss}} > 50\text{GeV}$ ,  $H_T > 300\text{GeV}$ , and 2 b tagged jets. The simulation is normalized to data to account for trigger and lepton efficiencies. Figure 4.11 shows the jet multiplicity distribution for 2018 data/MC before and after applying the 2018-derived reweighting factors. The systematic uncertainty of half of the deviation from unity covers

variations present in the reweighted single lepton jet multiplicity distributions.

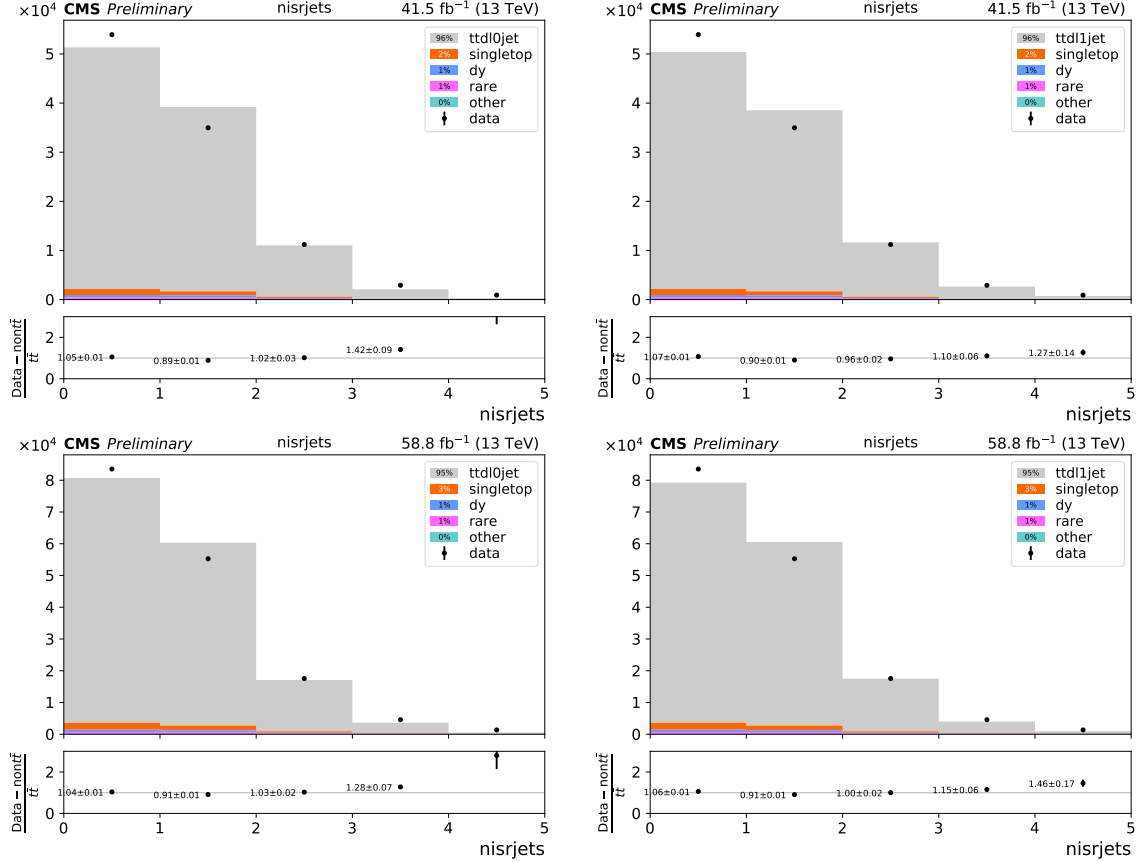


Figure 4.10: Distribution of the number of light jets in a dilepton  $t\bar{t}$  sample with 0 additional partons (left) or 1 additional parton (right) for 2017 data (top) and 2018 data (bottom) compared to their respective MC samples. In the case of 0 additional partons, the reweighting factor in the last bin is taken instead from the previous bin.

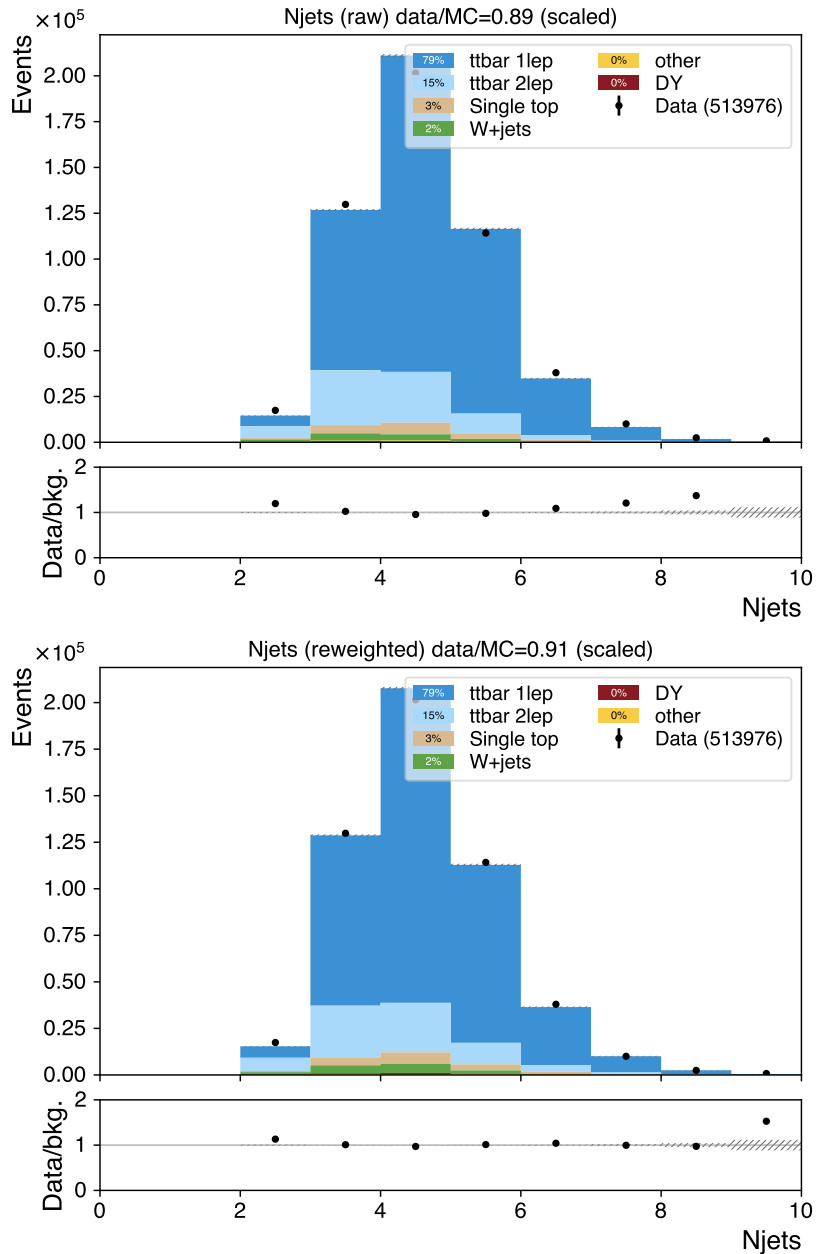


Figure 4.11: Jet multiplicity distribution for 2018 data/MC before (top) and after (bottom) applying the 2018-derived reweighting factors. The “other” category includes leading diboson,  $t\bar{t}W$ , and  $t\bar{t}Z$  contributions.

## 4.5 Control regions

In this section we describe the control regions (CRs) used to validate our background prediction methods with data for the main kinematic variables we use in defining our SRs:  $H_T$ ,  $p_T^{\text{miss}}$ ,  $m_T^{\text{min}}$ ,  $N_{\text{jets}}$ ,  $N_b$ , and for the case of the SM  $t\bar{t}t\bar{t}$  analysis, the input variables to the event-level BDT. In general, we observe good agreement across these CRs.

### 4.5.1 SUSY: OS events

In this CR, the same requirements on  $H_T$ ,  $p_T^{\text{miss}}$  and  $N_{\text{jets}}$  as in the inclusive SUSY analysis baseline selection are applied, except we require two OS tight leptons. This CR thus coincides with the application region used for the data-driven charge flip background estimate. Distributions are shown in Fig. 4.12. The variables are plotted again with a selection that relaxes the baseline  $p_T^{\text{miss}}$  cut in Fig. 4.13.

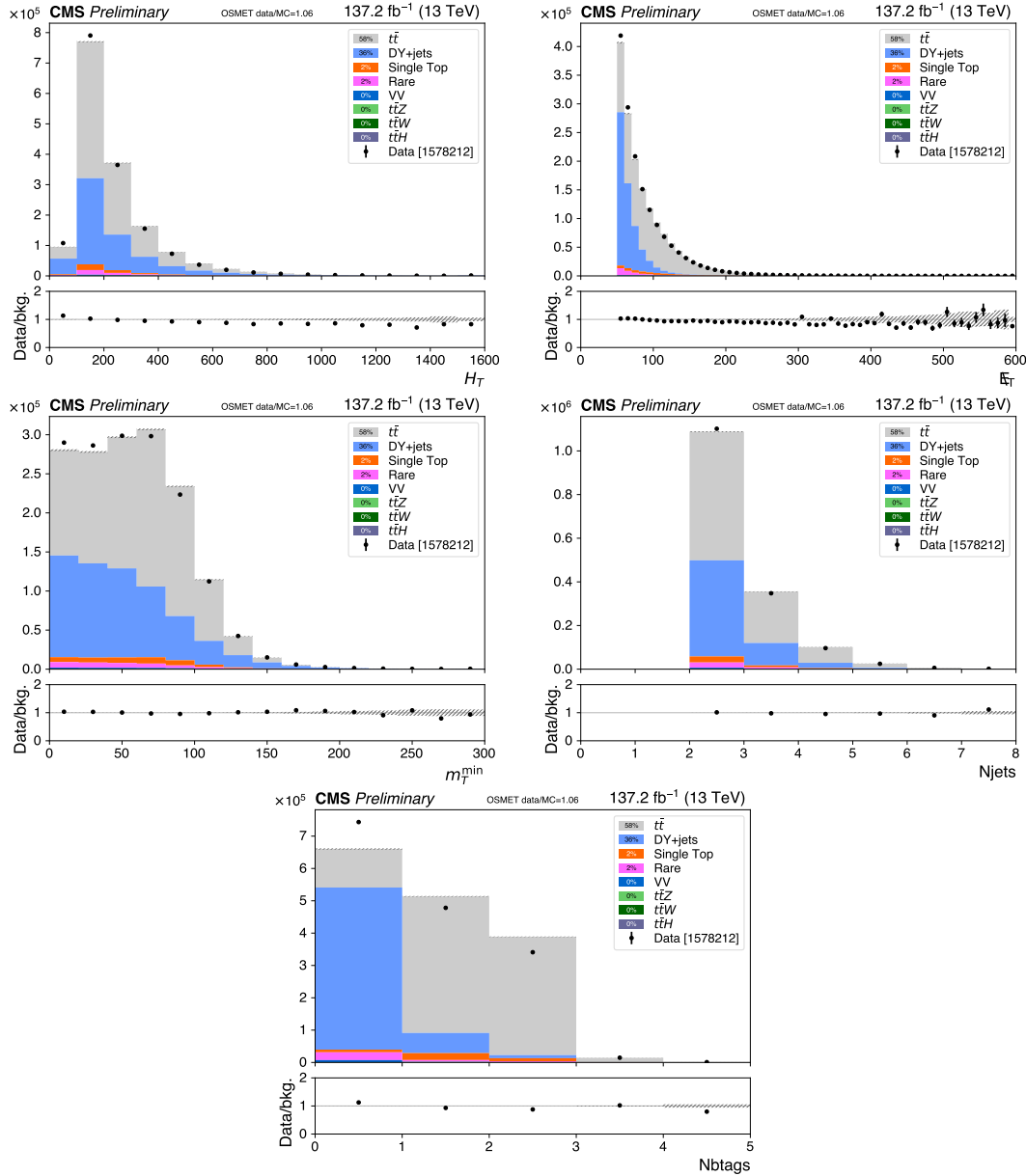


Figure 4.12: Data to simulation comparisons. From left to right and top to bottom, the  $H_T$ ,  $\cancel{E}_T$ ,  $m_T^{\min}$ ,  $N_{\text{jets}}$ ,  $N_{\text{btags}}$  distributions are shown for the OS CR.

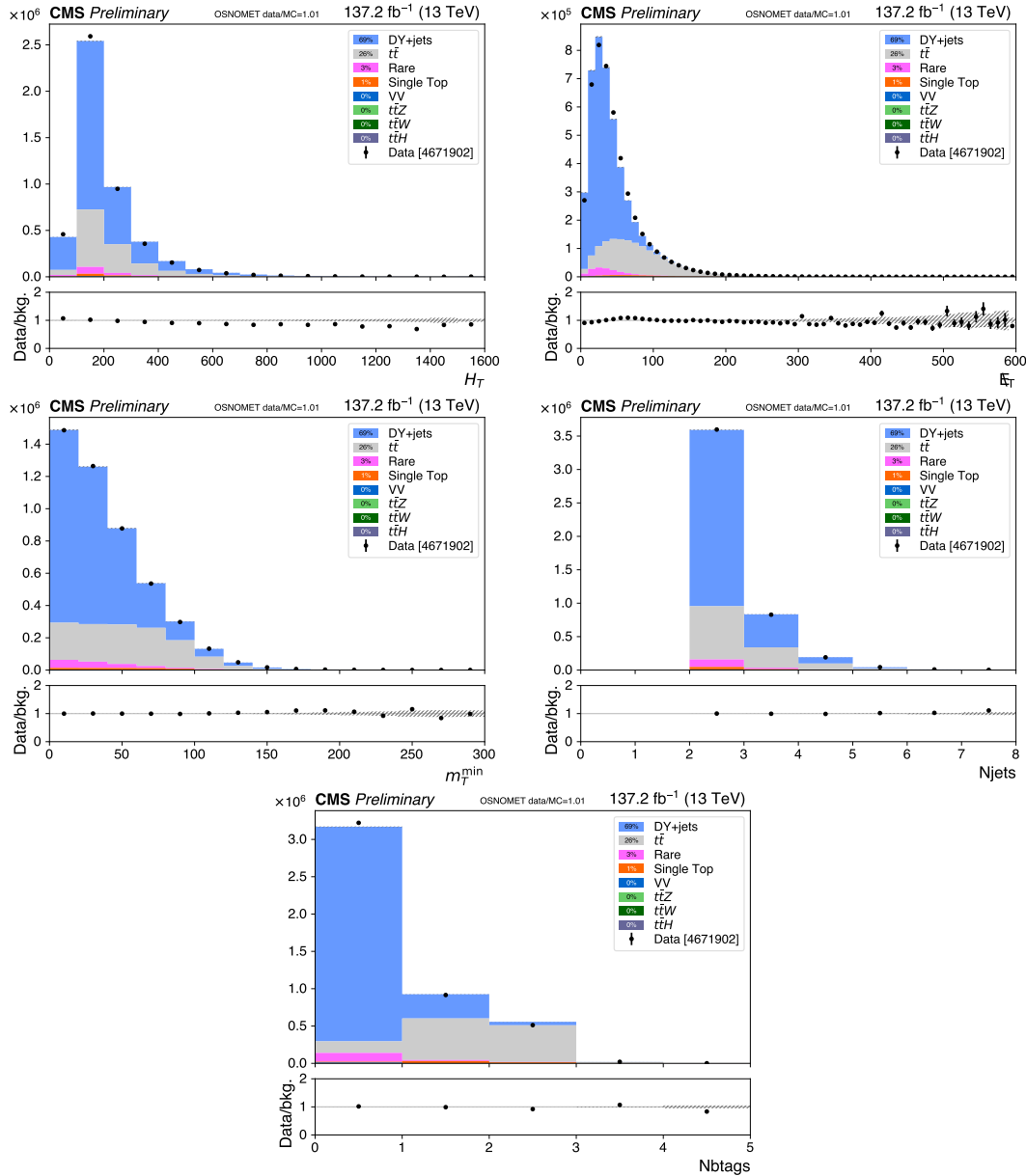


Figure 4.13: Data to simulation comparisons. From left to right and top to bottom, the  $H_T$ ,  $p_T^{\text{miss}}$ ,  $m_T^{\min}$ ,  $N_{\text{jets}}$ ,  $N_b$  distributions are shown for the OS CR, relaxing the  $p_T^{\text{miss}}$  cut.

### 4.5.2 SUSY: SS tight-loose events

This tight-loose (TL) CR has selections coinciding with the inclusive SUSY analysis baseline selection except with one tight lepton and one lepton failing the tight requirements (but passing the loose requirements). This CR roughly corresponds to the application region used for the nonprompt lepton background estimate. The variables are plotted again with a selection that relaxes the baseline  $p_T^{\text{miss}}$  cut in Fig. 4.15.

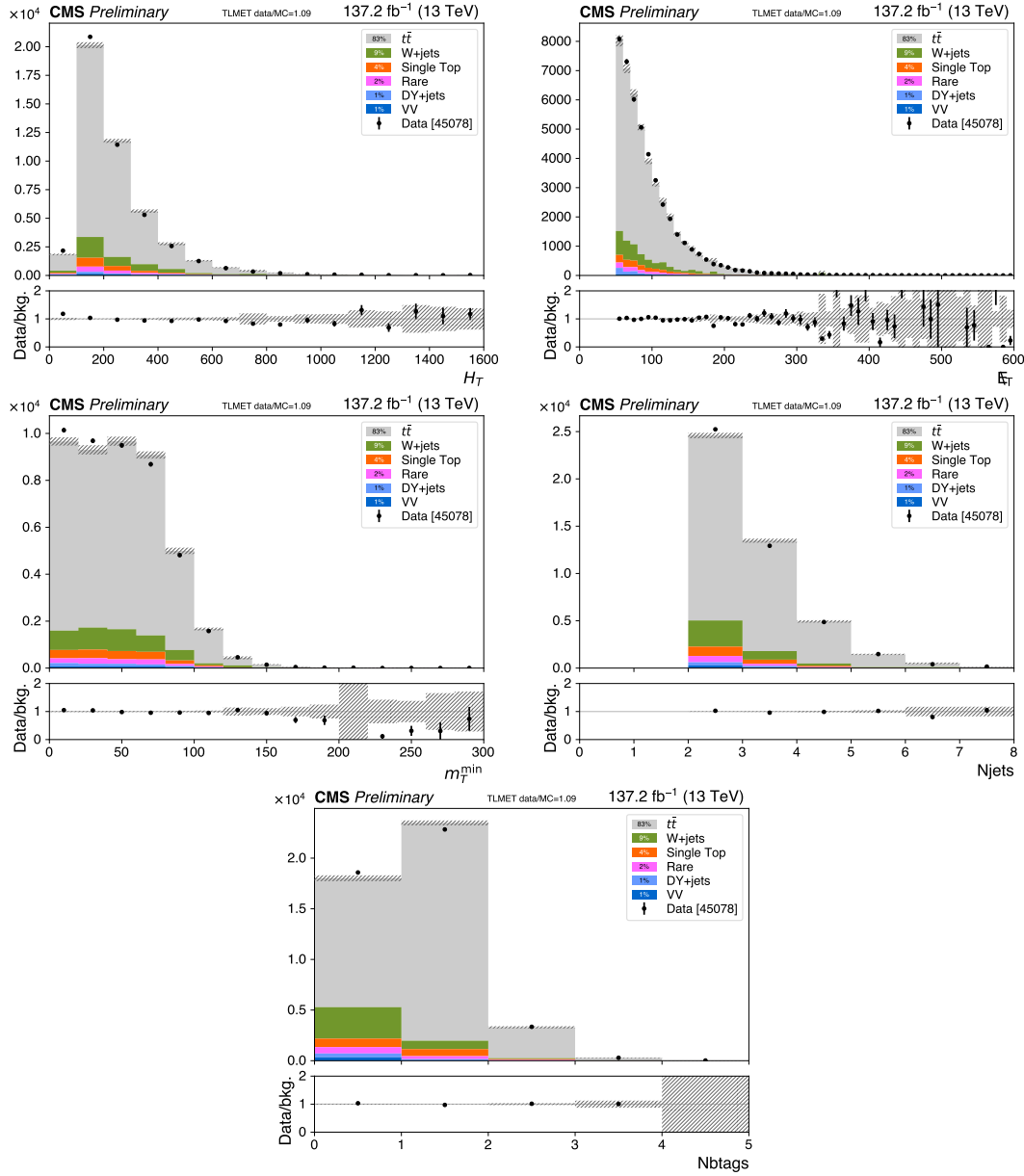


Figure 4.14: Data to simulation comparisons. From left to right and top to bottom, the  $H_T$ ,  $p_T^{\text{miss}}$ ,  $m_T^{\text{min}}$ ,  $N_{\text{jets}}$ ,  $N_{\text{btags}}$  distributions are shown for the TL CR.

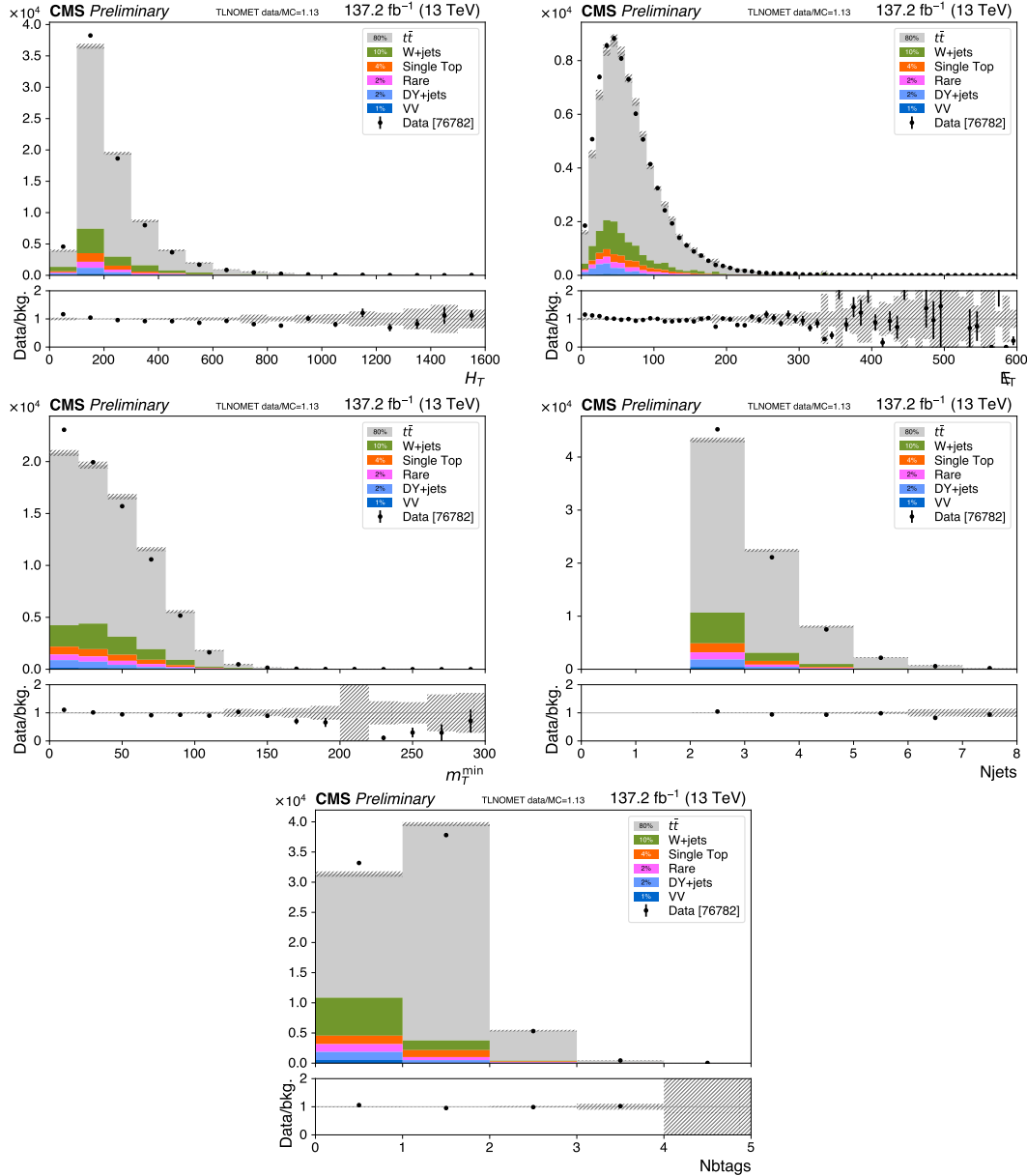


Figure 4.15: Data to simulation comparisons. From left to right and top to bottom, the  $H_T$ ,  $p_T^{\text{miss}}$ ,  $m_T^{\text{min}}$ ,  $N_{\text{jets}}$ ,  $N_b$  distributions are shown for the TL CR, relaxing the  $p_T^{\text{miss}}$  cut.

### 4.5.3 SUSY: Low $p_T^{\text{miss}}$ on-Z multi-lepton events

In this CR, the same requirements on  $H_T$  and  $N_{\text{jets}}$  as in the inclusive SUSY analysis baseline selection are applied, and we also apply the same requirements as for the on-Z multi-lepton kinematic regions, except the  $p_T^{\text{miss}}$  cut is inverted, becoming  $p_T^{\text{miss}} < 50\text{GeV}$ . Distributions are shown in Fig. 4.16.

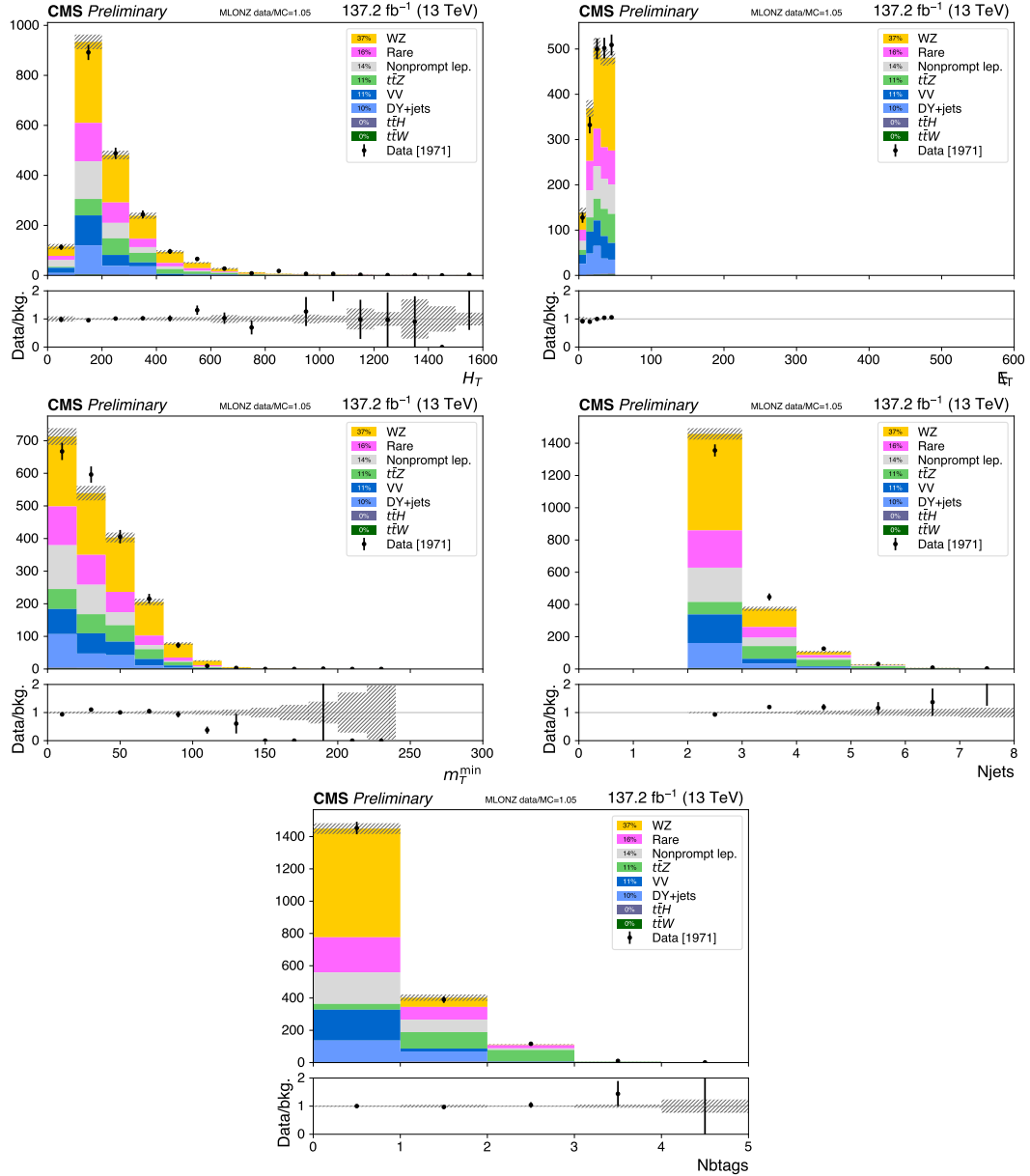


Figure 4.16: Data to simulation comparisons. From left to right and top to bottom, the  $H_T$ ,  $p_T^{\text{miss}}$ ,  $m_T^{\text{min}}$ ,  $N_{\text{jets}}$ ,  $N_b$  distributions are shown for the low  $p_T^{\text{miss}}$  on-Z multi-lepton region

#### 4.5.4 SUSY: Low $p_T^{\text{miss}}$ SS events

This CR is the low- $H_T$  version of the low  $p_T^{\text{miss}}$  inclusive SUSY analysis SRs, so selections are identical except we require  $H_T < 300\text{GeV}$  to be orthogonal to the SR

definitions. Distributions are shown in Fig. 4.17.

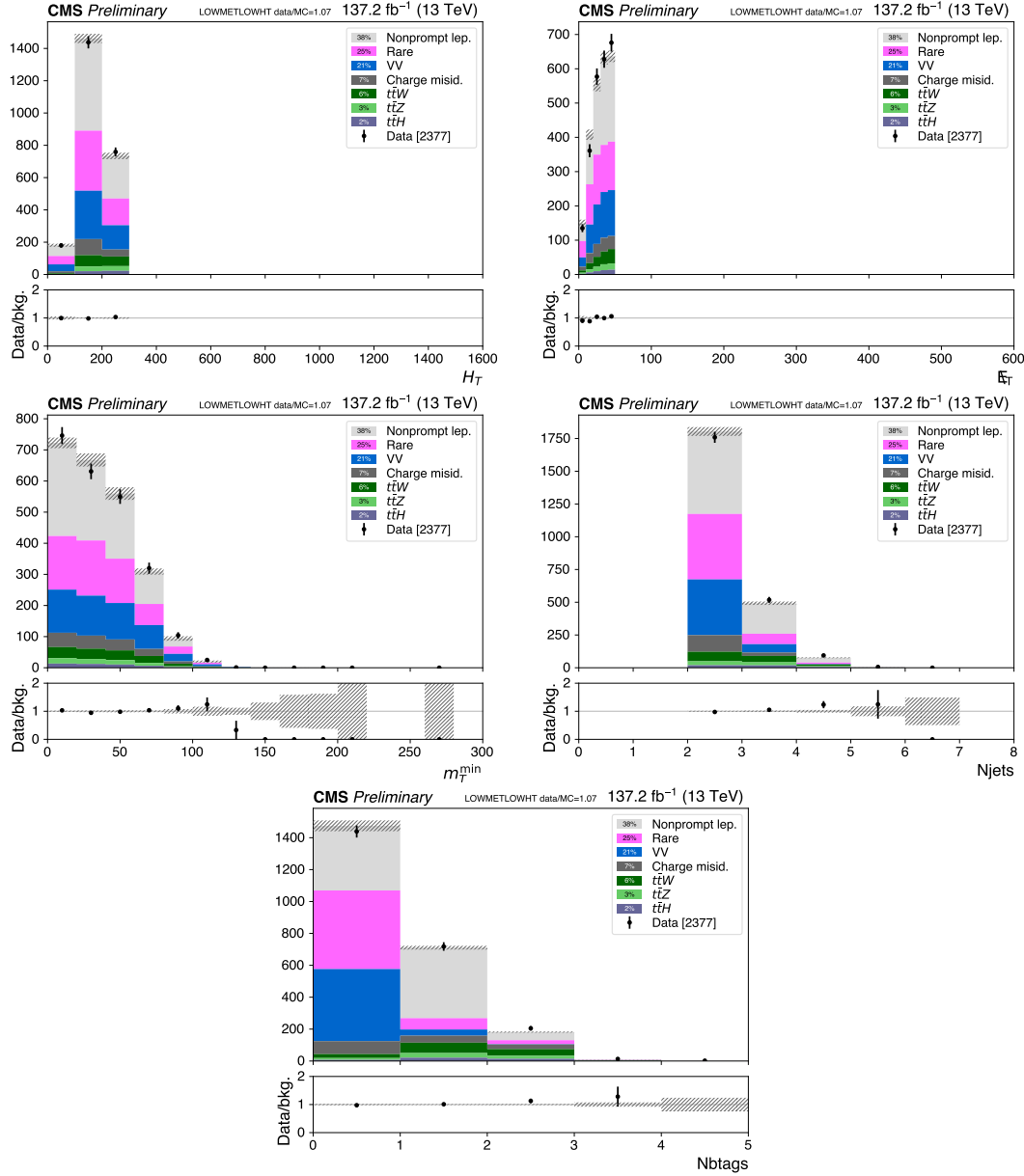


Figure 4.17: Data to simulation comparisons. From left to right and top to bottom, the  $H_T$ ,  $p_T^{\text{miss}}$ ,  $m_T^{\text{min}}$ ,  $N_{\text{jets}}$ ,  $N_{\text{btags}}$  distributions are shown for the low  $p_T^{\text{miss}}$  CR

#### 4.5.5 SM $t\bar{t}t\bar{t}$ : OS events

In this CR, the same requirements on  $H_T$ ,  $p_T^{\text{miss}}$  and  $N_{\text{jets}}$  as in the SM  $t\bar{t}t\bar{t}$  analysis baseline selection are applied, but we require two OS tight leptons and we remove the  $Z/\gamma^*$  veto. This CR coincides with the application region we use for the data-driven method to estimate the charge flips background. Distributions are shown in Fig. 4.18 for the main variables, and Fig. 4.19 for additional variables used in the BDT.

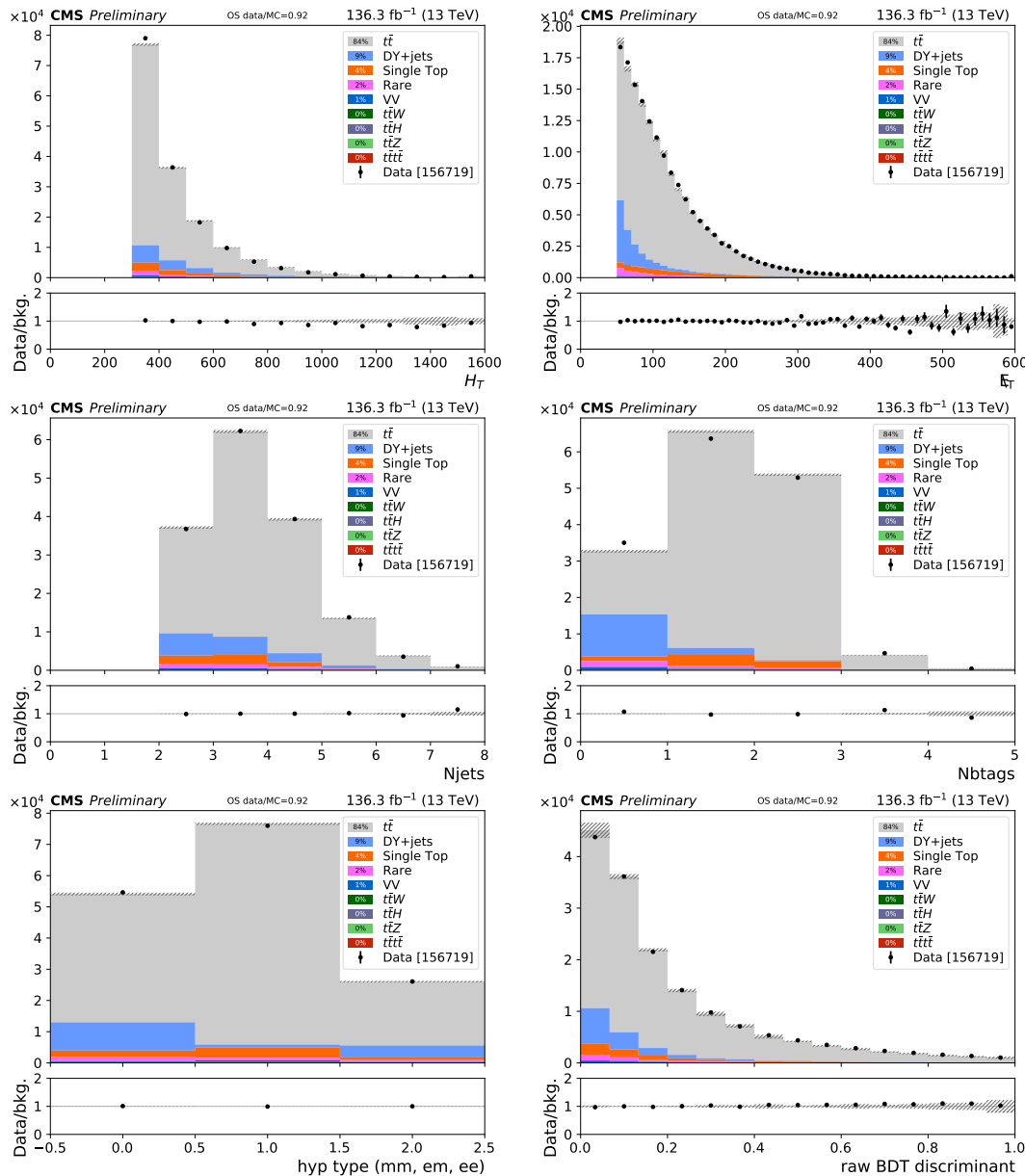


Figure 4.18: Data to simulation comparisons. From left top to right bottom the  $H_T$ ,  $p_T^{\text{miss}}$ ,  $N_{\text{jets}}$ ,  $N_b$ , lepton flavor and raw BDT discriminant distributions are shown for the opposite-sign dilepton baseline region. Shaded band shows MC stat uncertainty, except in the case of the discriminator distribution, where it has been added in quadrature with scale, btag, JEC, and JER variations

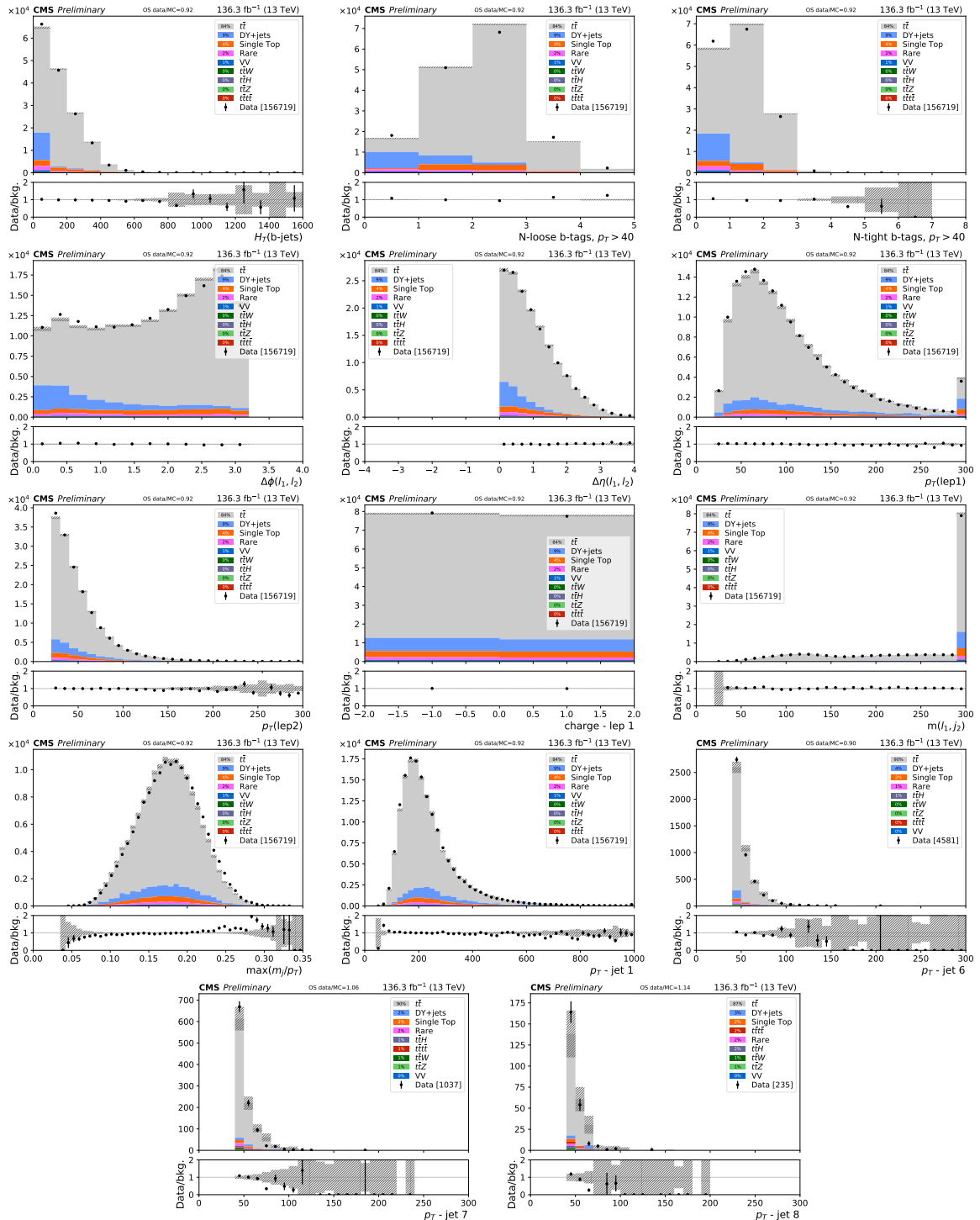


Figure 4.19: Data to simulation comparisons for the additional variables used by the BDT. From left top to right bottom,  $H_T^b$ ,  $N_{\text{loose}}^b$ ,  $N_{\text{tight}}^b$ ,  $\Delta\phi(\ell_1, \ell_2)$ ,  $\Delta\eta(\ell_1, \ell_2)$ ,  $p_T(\ell_1)$ ,  $p_T(\ell_2)$ ,  $p_T(\ell_3)$ ,  $q_1$ ,  $m(\ell_1, j_1)$ ,  $\max(m(j)/p_T(j))$  and the  $p_T$  for jets 1, 6, 7, and 8; shown for the opposite-sign dilepton baseline region.

#### 4.5.6 SM $t\bar{t}t\bar{t}$ : SS tight-loose events

In this CR, the same requirements on  $H_T$ ,  $p_T^{\text{miss}}$  and  $N_{\text{jets}}$  as in the inclusive SM  $t\bar{t}t\bar{t}$  analysis baseline selection are applied, but we require one tight lepton and one same-sign lepton failing the tight requirement. This CR is enriched in events with one fake lepton, and roughly corresponds to the application region for nonprompt lepton background estimate. Distributions are shown in Fig. 4.20 for the main variables, and Fig. 4.21 for additional variables used in the BDT. While there is an overall underestimate, there does not seem to be large trends in the main kinematic variables. Since this background is predicted from data, this underestimate is not an issue with the analysis strategy.

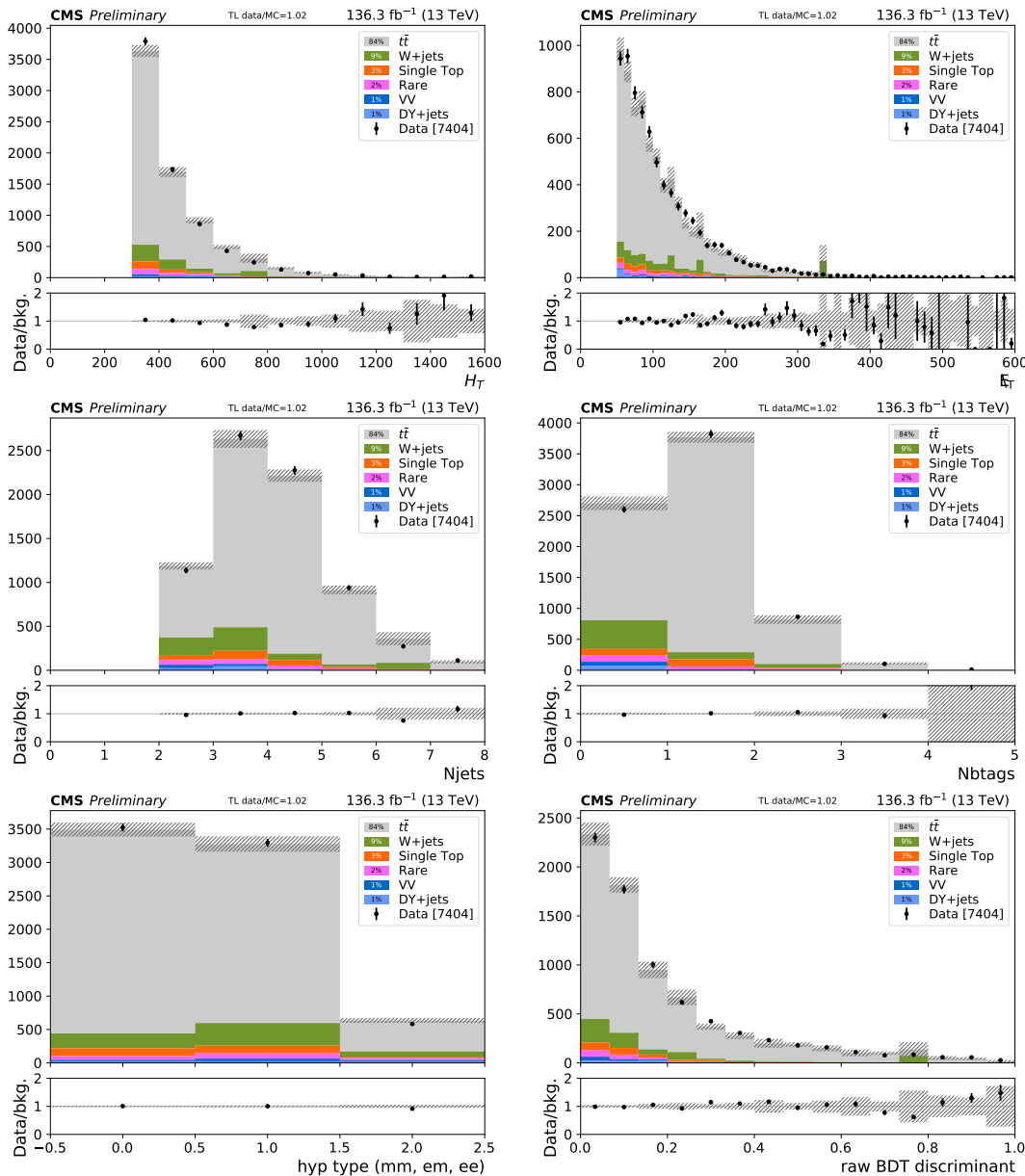


Figure 4.20: Data to simulation comparisons. From left top to right bottom the  $H_T$ ,  $p_T^{\text{miss}}$ ,  $N_{\text{jets}}$ ,  $N_b$ , lepton flavor and raw BDT discriminant distributions are shown for the same-sign tight+fail dilepton baseline region. Shaded band shows MC stat uncertainty, except in the case of the discriminator distribution, where it has been added in quadrature with scale, btag, JEC, and JER variations

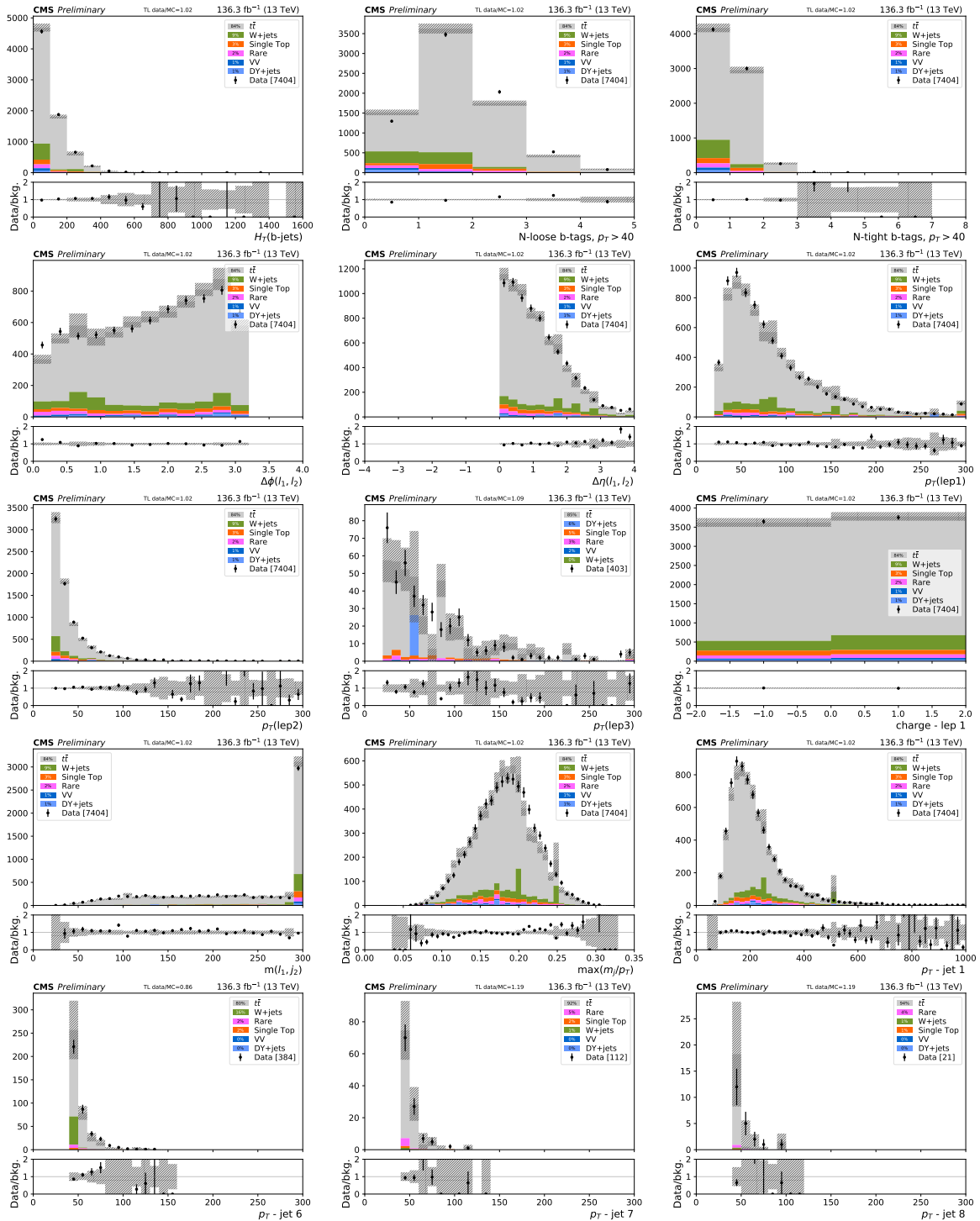


Figure 4.21: Data to simulation comparisons for the additional variables used by the BDT. From left top to right bottom,  $H_T^b$ ,  $N_b^{\text{loose}}$ ,  $N_b^{\text{tight}}$ ,  $\Delta\phi(\ell_1, \ell_2)$ ,  $\Delta\eta(\ell_1, \ell_2)$ ,  $p_T(\ell_1)$ ,  $p_T(\ell_2)$ ,  $p_T(\ell_3)$ ,  $q_1$ ,  $m(\ell_1, j_1)$ ,  $\max(m(j)/p_T(j))$  and the  $p_T$  for jets 1, 6, 7, and 8; shown for the same-sign tight+fail dilepton baseline region.

#### 4.5.7 SM $t\bar{t}t\bar{t}$ : Fake-enriched events

In this CR, the same requirements on  $H_T$ ,  $p_T^{\text{miss}}$  and  $N_{\text{jets}}$  as in the inclusive SM  $t\bar{t}t\bar{t}$  analysis baseline selection are applied, except we relax the  $H_T$  requirement and require  $N_b = 1$ . This region has a significant nonprompt lepton component and allows us to check the overall closure of the method in data. In the plots, the fake background is data-driven. Distributions are shown in Figs. 4.22. As written on the plots, overall data/MC normalization factor in this region is 1.06. If fakes are entirely responsible for this discrepancy, and given that fakes constitute half of the background, this represents a 12% normalization increase of fakes, well within the 30% normalization systematic uncertainty which we take on this process.

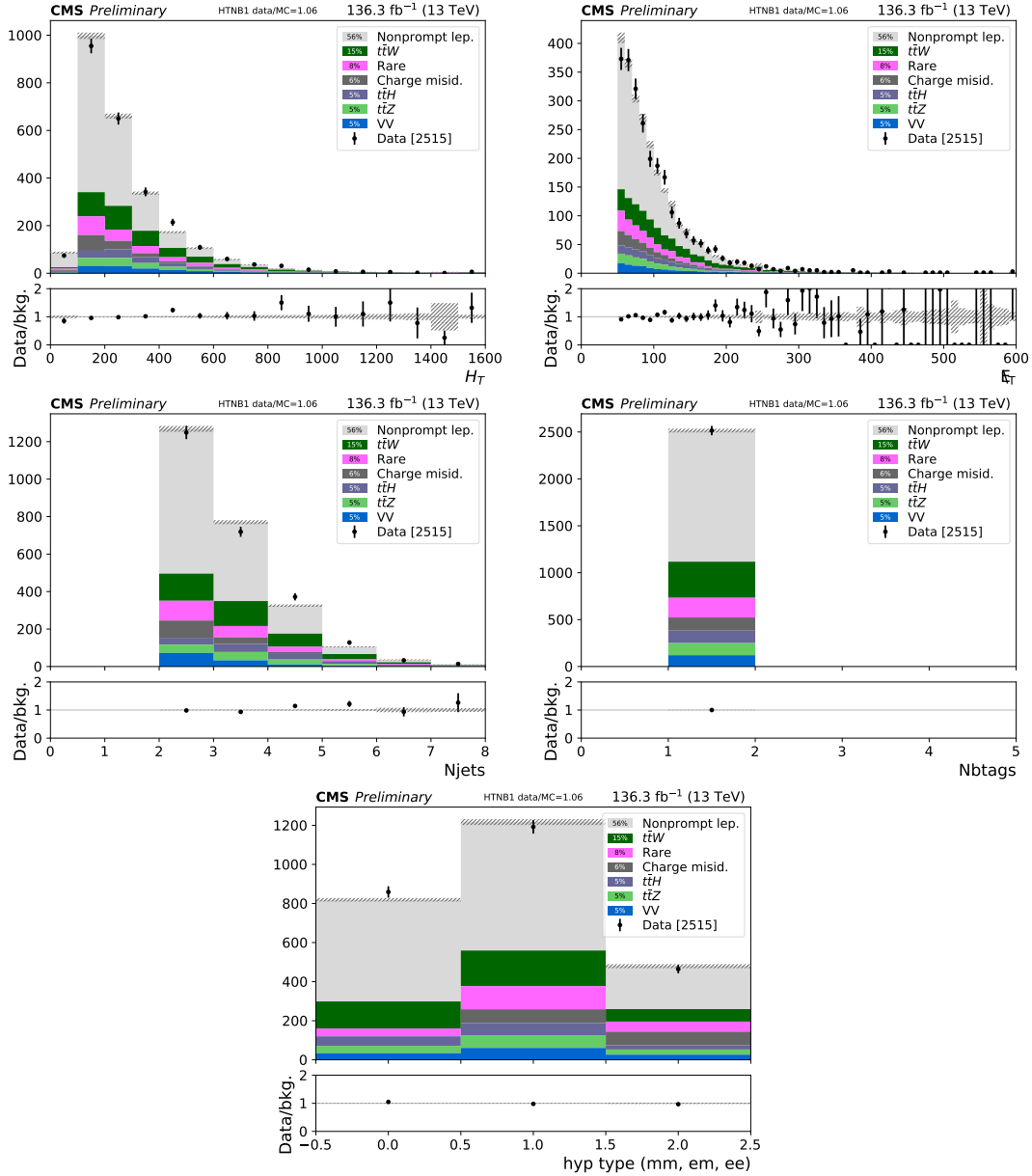


Figure 4.22: Data to simulation comparisons. From left top to right bottom the  $H_T$ ,  $p_T^{\text{miss}}$ ,  $N_{\text{jets}}$ ,  $N_b$ , lepton flavor and raw BDT discriminant distributions are shown for the same-sign dilepton region with  $N_b = 1$ ,  $N_{\text{jets}} \geq 2$ ,  $p_T^{\text{miss}} \geq 50$ . Shaded band shows MC stat uncertainty.

## 4.6 Systematic uncertainties

Sources of systematic uncertainty, many of which are associated with corrections and calibrations discussed previously, are summarized in Tables 4.3 and 4.4, for the inclusive SUSY analysis and SM  $t\bar{t}t\bar{t}$  analysis, respectively.

Uncertainties for processes are considered on the process normalization (number of events), and shape (distribution of events across the SRs). Experimental uncertainties in normalization and shape are treated as fully correlated among the SRs for all signal and background processes.

For the SM  $t\bar{t}t\bar{t}$  analysis, the  $t\bar{t}t\bar{t}$  signal has an unconstrained normalization uncertainty in order to measure its cross section. In this analysis, the largest sources of uncertainty, on the basis of what impacts the measurement of  $t\bar{t}t\bar{t}$  the most, are jet-related, and dominated by the correction that reweights the extra b contribution. However, to put these uncertainties into perspective, less than approximately a quarter of the precision of the  $t\bar{t}t\bar{t}$  measurement comes from systematic uncertainties. The remaining amount comes from statistics. That is, the SM  $t\bar{t}t\bar{t}$  measurement precision primarily benefits from increased luminosity.

Source	Uncertainty (%)	Correlated
Integrated luminosity	2.3–2.5	
Lepton selection	2–10	
Trigger efficiency	2–7	
Pileup	0–6	
Jet energy scale	1–15	
$b$ tagging	1–10	
Simulated sample size	1–20	
Scale and PDF variations	10–20	Yes
Theoretical background cross sections	30–50	Yes
Nonprompt leptons	30	Yes
Charge misidentification	20	
$N_J^{\text{ISR}}$	1–30	

Table 4.3: Summary of the sources of systematic uncertainty and their effect on the yields of different processes in the SRs. The first two groups list experimental and theoretical uncertainties assigned to processes estimated using simulation, while the last group lists uncertainties assigned to processes whose yield is estimated from the data. The uncertainties in the first group also apply to signal samples. Reported values are representative for the most relevant signal regions. The last column indicates if an uncertainty source is treated as fully uncorrelated across the three years of data taking.

Source	Uncertainty (%)	Impact on	
		$\sigma(t\bar{t}t\bar{t})$ (%)	Correlated
Integrated luminosity	2.3–2.5	2	
Pileup	0–5	1	
Trigger efficiency	2–7	2	
Lepton selection	2–10	2	
Jet energy scale	1–15	9	
Jet energy resolution	1–10	6	
$b$ tagging	1–15	6	
Size of simulated sample	1–25	<1	
Scale and PDF variations	10–15	2	Yes
ISR/FSR (signal)	5–15	2	Yes
$t\bar{t}H$ (normalization)	25	5	Yes
Rare, $X\gamma$ , $t\bar{t}VV$ (norm.)	11–20	<1	Yes
$t\bar{t}Z$ , $t\bar{t}W$ (norm.)	40	3–4	Yes
Charge misidentification	20	<1	Yes
Nonprompt leptons	30–60	3	Yes
$N_{\text{jets}}^{\text{ISR/FSR}}$	1–30	2	
$\sigma(t\bar{t}b\bar{b})/\sigma(t\bar{t}jj)$	35	11	Yes

Table 4.4: Summary of the sources of uncertainty, their values, and their impact, defined as the relative change of the measurement of  $\sigma(t\bar{t}t\bar{t})$  induced by one-standard-deviation variations corresponding to each uncertainty source considered separately. The first group lists experimental and theoretical uncertainties in simulated signal and background processes. The second group lists normalization uncertainties in the estimated backgrounds. The last column indicates if an uncertainty source is treated as fully uncorrelated across the three years of data taking.

# Chapter 5

## Results and interpretations

The following sections describe the results of the inclusive SUSY and SM  $t\bar{t}t\bar{t}$  analyses after making the SR selections and performing background estimations. The yields in the SRs are used to draw statistical conclusions about different signal hypotheses with likelihood-based techniques. For example, to exclude certain hypotheses on the basis of the observed data distributions across the SRs, or to quote a statistical significance for an expected signal. While these statistical techniques will be labeled where they are used (and can be quite sophisticated), a toy example illustrating the profile likelihood method with a single nuisance parameter is available in Appendix A.

### 5.1 SUSY results

The distributions of the variables used to define the SRs after the event selection are shown in Fig. 5.1. Background yields shown as stacked histograms in Figs. 5.1, 5.2, and

5.3 are those determined following baseline selections for the inclusive SUSY analysis. The overall data yields exceed expectation by an amount close to the systematic uncertainty. However, there is no trend observed that is beyond the systematic uncertainties. is seen in the distributions, the significance of the excess is of similar magnitude in all categories, with a maximum of around 2 standard deviations (s.d.) in the off-Z ML category.

The results of the search, broken down by kinematic category and SR, are presented in Figs. 5.2 and 5.3. The expected background event yields, total uncertainties, and observed event yields in the SRs used in this search are summarized in Table 5.1. Unfortunately (or fortunately), *no significant deviation with respect to the SM background prediction is observed*. The largest excess of events found by fitting the data with the background-only hypothesis is in HH SR54 with a local significance of 2.6 s.d. However, its neighboring bin, HH SR55, adjacent in kinematic phase space along the  $H_T$  dimension, has a deficit of events in the data corresponding to a significance of 1.8 s.d.

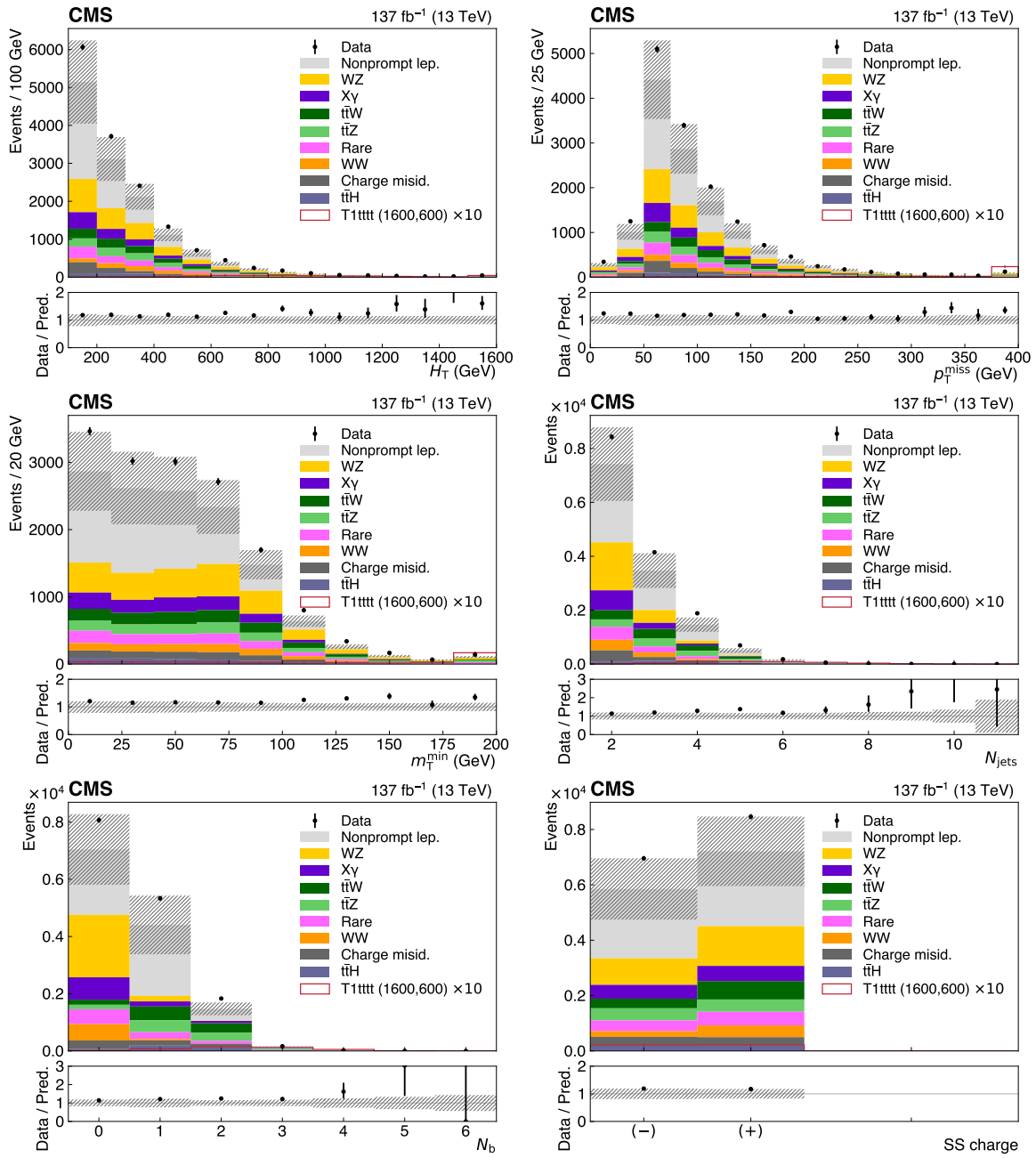


Figure 5.1: Distributions of the main analysis variables after the event selection:  $H_T$ ,  $p_T^{\text{miss}}$ ,  $m_T^{\text{min}}$ ,  $N_{\text{jets}}$ ,  $N_b$ , and the charge of the SS pair, where the last bin includes the overflow (where applicable). The hatched area represents the total statistical and systematic uncertainty in the background prediction. The lower panels show the ratio of the observed event yield to the background prediction. The prediction for the SUSY model T1ttt with  $m_{\tilde{g}} = 1600\text{GeV}$  and  $m_{\tilde{\chi}_1^0} = 600\text{GeV}$  is overlaid.

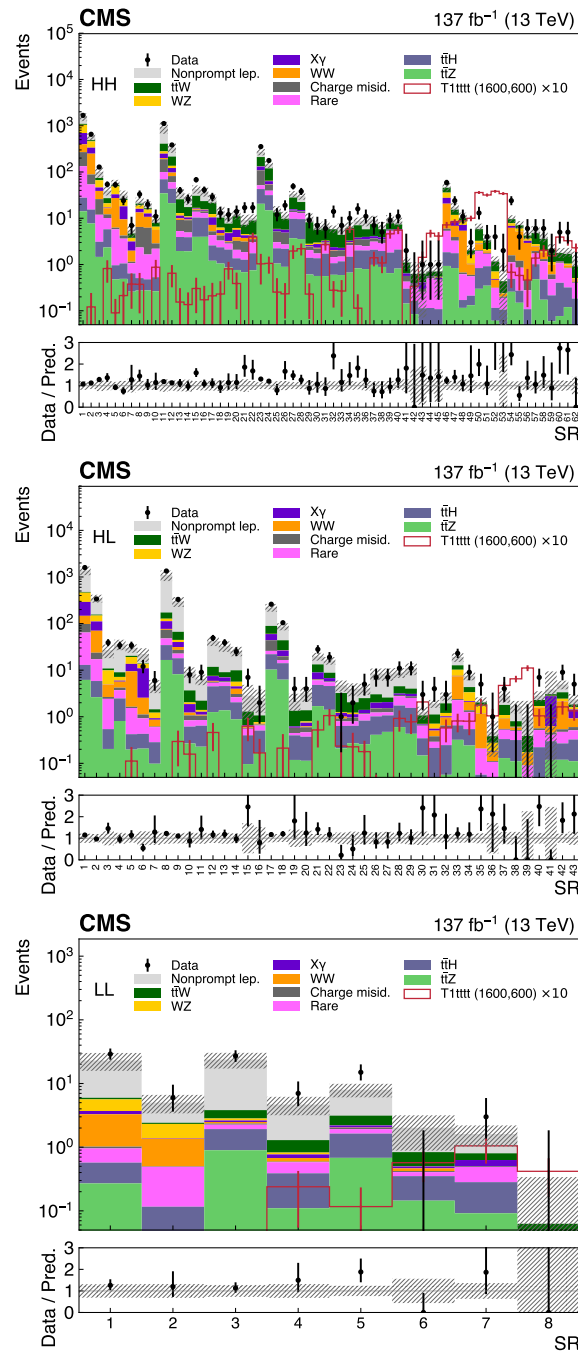


Figure 5.2: Expected and observed SR yields for the HH, HL, LL signal categories. The hatched area represents the total statistical and systematic uncertainty in the background prediction.

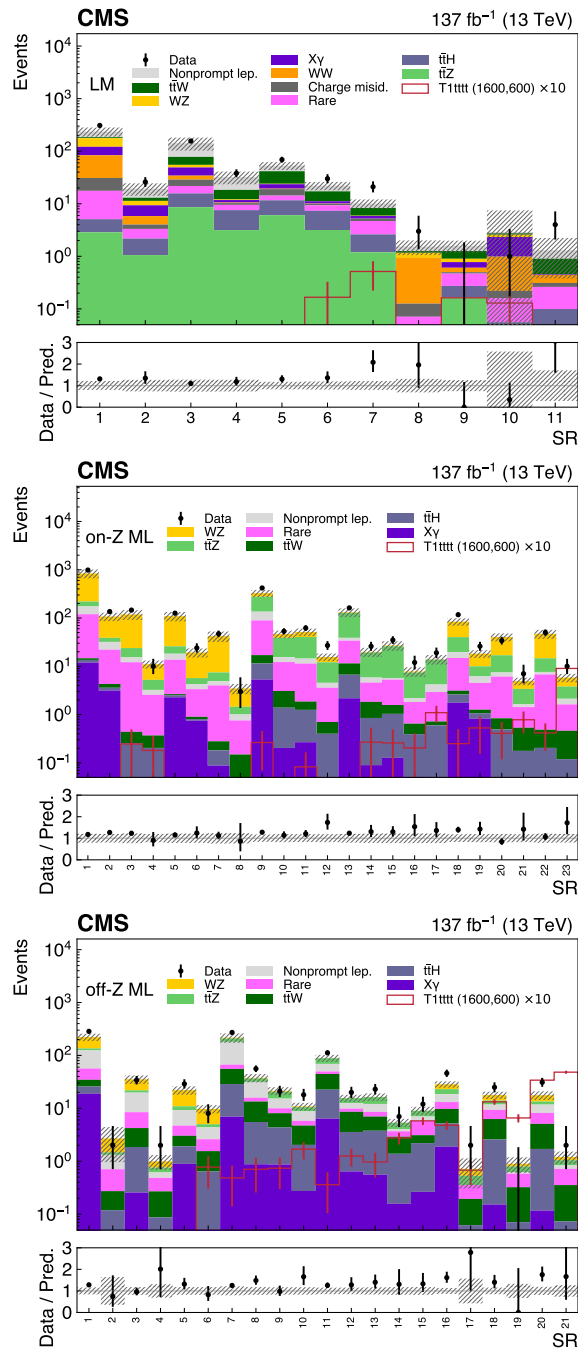


Figure 5.3: Expected and observed SR yields for the LM, on-Z ML, off-Z ML signal categories. The hatched area represents the total statistical and systematic uncertainty in the background prediction.

SR	HH regions		HL regions		LM regions			
	Expected SM	Obs.	Expected SM	Obs.	Expected SM	Obs.		
1	1560 $\pm$ 300	1673	1	1390 $\pm$ 300	1593	1	235 $\pm$ 47	309
2	582 $\pm$ 93	653	2	348 $\pm$ 67	337	2	19.3 $\pm$ 5.2	26
3	100 $\pm$ 25	128	3	26.9 $\pm$ 8.8	39	3	142 $\pm$ 39	156
4	39.5 $\pm$ 8.5	54	4	35.9 $\pm$ 9.1	34	4	32.2 $\pm$ 8.8	38
5	57.7 $\pm$ 9.9	53	5	29.8 $\pm$ 6.0	34	5	53.0 $\pm$ 9.1	69
6	32.5 $\pm$ 7.1	24	6	22.2 $\pm$ 7.2	12	6	22.0 $\pm$ 4.0	30
7	5.5 $\pm$ 1.8	7	7	4.7 $\pm$ 1.4	6	7	10.1 $\pm$ 2.0	21
8	22.9 $\pm$ 5.1	33	8	1100 $\pm$ 280	1342	8	1.53 $\pm$ 0.48	3
9	19.5 $\pm$ 3.9	20	9	299 $\pm$ 71	330	9	1.58 $\pm$ 0.41	0
10	9.6 $\pm$ 1.9	11	10	9.1 $\pm$ 2.3	8	10	2.9 $\pm$ 2.9	1
11	940 $\pm$ 270	1115	11	6.4 $\pm$ 1.6	9	11	1.31 $\pm$ 0.93	4
12	340 $\pm$ 81	384	12	42.1 $\pm$ 9.2	49	on-Z ML regions		
13	36.3 $\pm$ 9.5	40	13	33.0 $\pm$ 8.4	39	SR	Expected SM	Obs.
14	26.8 $\pm$ 7.4	26	14	25.8 $\pm$ 5.9	25	1	840 $\pm$ 170	985
15	42.7 $\pm$ 8.6	68	15	2.8 $\pm$ 2.0	7	2	107 $\pm$ 21	136
16	37.9 $\pm$ 8.6	41	16	2.5 $\pm$ 1.3	2	3	119 $\pm$ 27	146
17	26.5 $\pm$ 6.2	29	17	222 $\pm$ 42	260	4	11.1 $\pm$ 2.1	10
18	14.3 $\pm$ 3.6	13	18	86 $\pm$ 15	104	5	109 $\pm$ 24	126
19	10.6 $\pm$ 2.5	12	19	2.22 $\pm$ 0.90	4	6	19.3 $\pm$ 4.1	24
20	12.3 $\pm$ 2.9	14	20	3.2 $\pm$ 1.1	4	7	42 $\pm$ 10	47
21	9.2 $\pm$ 2.7	17	21	19.8 $\pm$ 3.8	28	8	3.47 $\pm$ 0.84	3
22	10.1 $\pm$ 2.1	17	22	16.1 $\pm$ 3.0	19	9	327 $\pm$ 54	419
23	272 $\pm$ 43	354	23	4.7 $\pm$ 1.3	1	10	46.5 $\pm$ 8.4	53
24	147 $\pm$ 25	177	24	4.0 $\pm$ 1.2	2	11	51.3 $\pm$ 9.1	62
25	15.3 $\pm$ 2.9	12	25	4.0 $\pm$ 1.1	5	12	15.6 $\pm$ 2.8	27
26	11.4 $\pm$ 2.4	19	26	8.5 $\pm$ 2.4	7	13	131 $\pm$ 27	162
27	33.4 $\pm$ 5.4	49	27	8.4 $\pm$ 2.5	7	14	19.9 $\pm$ 4.3	26
28	30.1 $\pm$ 4.9	38	28	8.9 $\pm$ 2.2	11	15	26.9 $\pm$ 6.1	35
29	10.4 $\pm$ 2.2	9	29	10.9 $\pm$ 3.1	11	16	7.8 $\pm$ 1.8	12
30	6.6 $\pm$ 1.3	7	30	1.25 $\pm$ 0.39	3	17	14.0 $\pm$ 3.1	19
31	6.9 $\pm$ 1.5	6	31	1.92 $\pm$ 0.37	4	18	84 $\pm$ 15	117
32	5.9 $\pm$ 1.1	14	32	2.77 $\pm$ 0.56	3	19	18.2 $\pm$ 3.3	26
33	6.1 $\pm$ 1.6	7	33	19.1 $\pm$ 4.1	23	20	40.4 $\pm$ 7.6	34
34	6.8 $\pm$ 1.3	10	34	7.5 $\pm$ 1.5	9	21	4.92 $\pm$ 0.88	7
35	8.8 $\pm$ 1.5	16	35	2.12 $\pm$ 0.49	5	22	46.9 $\pm$ 9.9	50
36	8.7 $\pm$ 2.0	11	36	0.47 $\pm$ 0.33	1	23	5.8 $\pm$ 1.2	10
37	9.4 $\pm$ 1.9	7	37	2.75 $\pm$ 0.77	4	off-Z ML regions		
38	7.0 $\pm$ 1.3	5	38	1.68 $\pm$ 0.50	0	SR	Expected SM	Obs.
39	9.6 $\pm$ 2.1	9	39	0.97 $\pm$ 0.97	0	1	222 $\pm$ 36	285
40	8.6 $\pm$ 1.7	11	40	2.83 $\pm$ 0.70	7	2	2.7 $\pm$ 1.7	2
41	1.10 $\pm$ 0.32	2	41	3.8 $\pm$ 3.8	0	3	35.5 $\pm$ 6.4	34
42	0.63 $\pm$ 0.49	0	42	4.9 $\pm$ 1.0	9	4	0.99 $\pm$ 0.31	2
43	0.67 $\pm$ 0.60	1	43	2.36 $\pm$ 0.72	5	LL regions		
44	0.74 $\pm$ 0.27	1				5	22.1 $\pm$ 4.0	29
45	0.71 $\pm$ 0.53	1	SR	Expected SM	Obs.	6	9.7 $\pm$ 1.7	8
46	47.8 $\pm$ 9.7	59	1	23.0 $\pm$ 7.2	29	7	217 $\pm$ 44	272
47	17.3 $\pm$ 3.8	24	2	5.0 $\pm$ 1.6	6	8	37.7 $\pm$ 6.8	56
48	10.3 $\pm$ 2.9	11	3	23.8 $\pm$ 6.6	27	9	21.4 $\pm$ 3.7	21
49	2.06 $\pm$ 0.49	3	4	4.7 $\pm$ 1.5	7	10	10.9 $\pm$ 1.9	18
50	6.5 $\pm$ 1.1	13	5	8.0 $\pm$ 1.9	15	11	89 $\pm$ 14	112
51	3.72 $\pm$ 0.79	4	6	2.0 $\pm$ 1.1	0	12	15.6 $\pm$ 2.4	20
52	1.21 $\pm$ 0.29	4	7	1.61 $\pm$ 0.59	3	13	16.4 $\pm$ 2.7	23
53	0.44 $\pm$ 0.44	2	8	0.06 $\pm$ 0.06	0	14	5.36 $\pm$ 0.95	7
54	9.8 $\pm$ 1.8	24				15	9.0 $\pm$ 1.6	12
55	7.3 $\pm$ 1.4	4				16	28.4 $\pm$ 3.9	46
56	4.44 $\pm$ 0.98	6				17	0.72 $\pm$ 0.41	2
57	5.7 $\pm$ 1.1	6				18	17.8 $\pm$ 2.8	25
58	4.0 $\pm$ 1.0	6				19	0.89 $\pm$ 0.29	0
59	2.24 $\pm$ 0.53	2				20	17.7 $\pm$ 3.3	31
60	1.83 $\pm$ 0.44	5				21	1.20 $\pm$ 0.32	2
61	1.88 $\pm$ 0.40	5						
62	1.35 $\pm$ 0.56	0						

Table 5.1: Expected background event yields, total uncertainties, and observed event yields in the SRs used in this search.

## 5.2 SUSY interpretations

### 5.2.1 Model-dependent

The results are interpreted as constraints on the cross sections for signal models. Event yields in all SRs are used to obtain exclusion limits on the production cross section of each model at 95% confidence level (CL) with an asymptotic formulation of the modified frequentist  $CL_s$  criterion [58, 59, 60, 61], where uncertainties are incorporated as nuisance parameters and profiled [60]. Since the normalizations of the various backgrounds allowed to vary within their uncertainties in the likelihood fit, several backgrounds (nonprompt lepton,  $t\bar{t}W/Z/H$  and rare processes) are pulled up by around 1 s.d. This is consistent with the latest measurements of  $t\bar{t}W$  and  $t\bar{t}Z$  processes performed by the ATLAS and CMS Collaborations [62, 63].

Figure 5.4 shows observed and expected exclusion limits for simplified models of gluino pair production with each gluino decaying to off- or on-shell third-generation squarks, T1tttt, T5ttbbWW, T5tttt, and T5ttcc. Figs. 5.5 and 5.6 show the corresponding limits for T5qqqqWZ and T5qqqqWW, with two different assumptions on the chargino mass. The T5qqqqWZ model assumes equal probabilities for the decay of the gluino into  $\tilde{\chi}_1^+$ ,  $\tilde{\chi}_1^-$ , and  $\tilde{\chi}_2^0$ . The exclusion limits for T6ttWW and T6ttHZ are displayed in Figs. 5.7 and 5.8, respectively. The three sets of exclusion limits shown in Fig. 5.8 correspond to the branching fraction  $\mathcal{B}(\tilde{t}_2 \rightarrow \tilde{t}_1 Z)$  having values of 0, 50, and 100%.

For the RPV models, Fig. 5.9 shows observed and expected limits on the cross section

of gluino pair production as a function of the gluino masses. Both the observed and expected exclusions on the gluino mass are similar and reach 2.1 and 1.7 TeV for the T1qqqqL and T1tbs models, respectively.

As there are many SRs and many topologically diverse signal models, it can be hard to associate sensitivity and performance with particular SRs or kinematic categories. To help with this, Table 5.2 presents the top five SRs for several representative models, ranked based on the largest values of  $N_{\text{sig.}}/\sqrt{N_{\text{bkg.}} + N_{\text{sig.}}}$ , where  $N_{\text{sig.}}$  and  $N_{\text{bkg.}}$  are the signal and total background yields in each SR, respectively. At a glance, one sees that high  $p_T^{\text{miss}}$  and high  $H_T$  regions in the HH kinematic category provide sensitivity for many high mass splitting topologies, while the LL category provides sensitivity for more compressed topologies.

Compared to previous versions of this analysis [25, 64], limits for the RPC models extend the gluino and squark mass observed and expected exclusions by up to 200 GeV primarily due to the increase in the integrated luminosity ( $35.9 \rightarrow 137\text{fb}^{-1}$ ) and the corresponding re-optimization of SR definitions. These results also complement searches for gluino pair production conducted by CMS in final states with 0 or 1 lepton [65, 66, 67]. The constraints on the two RPV models that were not previously included demonstrate the sensitivity of the analysis to RPV scenarios. The final state is particularly well suited to study the T1qqqqL model as there is no penalty from leptonic branching fraction, which results in exclusion limits on the gluino mass beyond 2.1 TeV, comparable to other results in fully hadronic final states [66, 67]. The limits obtained on the T1tbs

Table 5.2: Top five SRs for several representative models, ranked based on the largest values of  $N_{\text{sig.}}/\sqrt{N_{\text{bkg.}} + N_{\text{sig.}}}$ , where  $N_{\text{sig.}}$  and  $N_{\text{bkg.}}$  are the signal and total background yields in each SR, respectively.

model	mass point	top SRs
T1tttt	$m_{\tilde{g}} = 1400, m_{\tilde{\chi}_1^0} = 400$	off-Z ML21, HH53, HH52, HH51, HH50
T1tttt	$m_{\tilde{g}} = 2000, m_{\tilde{\chi}_1^0} = 100$	HH53, HH52, off-Z ML21, HL39, HH49
T1tttt	$m_{\tilde{g}} = 1800, m_{\tilde{\chi}_1^0} = 100$	HH53, off-Z ML21, HH52, HL39, HH51
T1tttt	$m_{\tilde{g}} = 1800, m_{\tilde{\chi}_1^0} = 1000$	off-Z ML21, HH53, HH52, HH51, HH50
T1tttt	$m_{\tilde{g}} = 1800, m_{\tilde{\chi}_1^0} = 1550$	HH53, HL39, off-Z ML21, HH49, HH52
T6ttWW	$m_{\tilde{b}_1} = 1000, m_{\tilde{\chi}_1^\pm} = 600$	off-Z ML21, HH53, HH51, HH50, HH52
T6ttWW	$m_{\tilde{b}_1} = 900, m_{\tilde{\chi}_1^\pm} = 400$	off-Z ML21, HH51, HH50, HH53, off-Z ML20
T6ttWW	$m_{\tilde{b}_1} = 800, m_{\tilde{\chi}_1^\pm} = 400$	off-Z ML21, HH51, HH50, HH34, off-Z ML20
T5qqqqWZ	$m_{\tilde{g}} = 1400, m_{\tilde{\chi}_1^0} = 1$	on-Z ML23, HH53, HH52, HH51, HH49
T5qqqqWZ	$m_{\tilde{g}} = 900, m_{\tilde{\chi}_1^0} = 600$	on-Z ML4, HH3, HH10, on-Z ML23, HH4
T5qqqqWW	$m_{\tilde{g}} = 1400, m_{\tilde{\chi}_1^0} = 1$	HH53, HH52, HH49, HH51, HH50
T5qqqqWW	$m_{\tilde{g}} = 900, m_{\tilde{\chi}_1^0} = 600$	HH3, HH10, HH4, HH7, HH50
T5qqqqWZ ( $m_{\tilde{\chi}_1^\pm} = m_{\tilde{\chi}_1^0} + 20\text{GeV}$ )	$m_{\tilde{g}} = 1400, m_{\tilde{\chi}_1^0} = 1$	HH59, HH53, HH52, HH62, HH51
T5qqqqWZ ( $m_{\tilde{\chi}_1^\pm} = m_{\tilde{\chi}_1^0} + 20\text{GeV}$ )	$m_{\tilde{g}} = 900, m_{\tilde{\chi}_1^0} = 600$	LL2, LL1, LL4, HL39, HL37
T5qqqqWW ( $m_{\tilde{\chi}_1^\pm} = m_{\tilde{\chi}_1^0} + 20\text{GeV}$ )	$m_{\tilde{g}} = 1400, m_{\tilde{\chi}_1^0} = 1$	HH59, HH53, HH52, HH51, HH62
T5qqqqWW ( $m_{\tilde{\chi}_1^\pm} = m_{\tilde{\chi}_1^0} + 20\text{GeV}$ )	$m_{\tilde{g}} = 900, m_{\tilde{\chi}_1^0} = 600$	LL2, LL4, HL39, LL1, HL37
T6ttHZ ( $\mathcal{B}(\tilde{t}_2 \rightarrow \tilde{t}_1 Z) = 1$ )	$m_{\tilde{t}_2} = 850, m_{\tilde{t}_1} = 625$	on-Z ML23, on-Z ML21, on-Z ML16, on-Z ML14, on-Z ML17
T6ttHZ ( $\mathcal{B}(\tilde{t}_2 \rightarrow \tilde{t}_1 Z) = 0.5$ )	$m_{\tilde{t}_2} = 850, m_{\tilde{t}_1} = 625$	on-Z ML17, on-Z ML23, on-Z ML21, on-Z ML14, on-Z ML16
T6ttHZ ( $\mathcal{B}(\tilde{t}_2 \rightarrow \tilde{t}_1 Z) = 0$ )	$m_{\tilde{t}_2} = 850, m_{\tilde{t}_1} = 625$	off-Z ML15, HH40, HH39, HH45, HH44
T1qqqL	$m_{\tilde{g}} = 1600$	HH62, LM11, HH59, HH61, HH51
T1qqqL	$m_{\tilde{g}} = 2400$	HH62, LM11, HH59, HH53, HH52
T1tbs	$m_{\tilde{g}} = 1200$	HH62, HH50, HH59, HH61, HH58
T1tbs	$m_{\tilde{g}} = 1700$	HH62, HH59, HH50, HH52, LM11

model are stronger than those previously obtained in the one-lepton channel based on the analysis of the 2016 dataset [68].

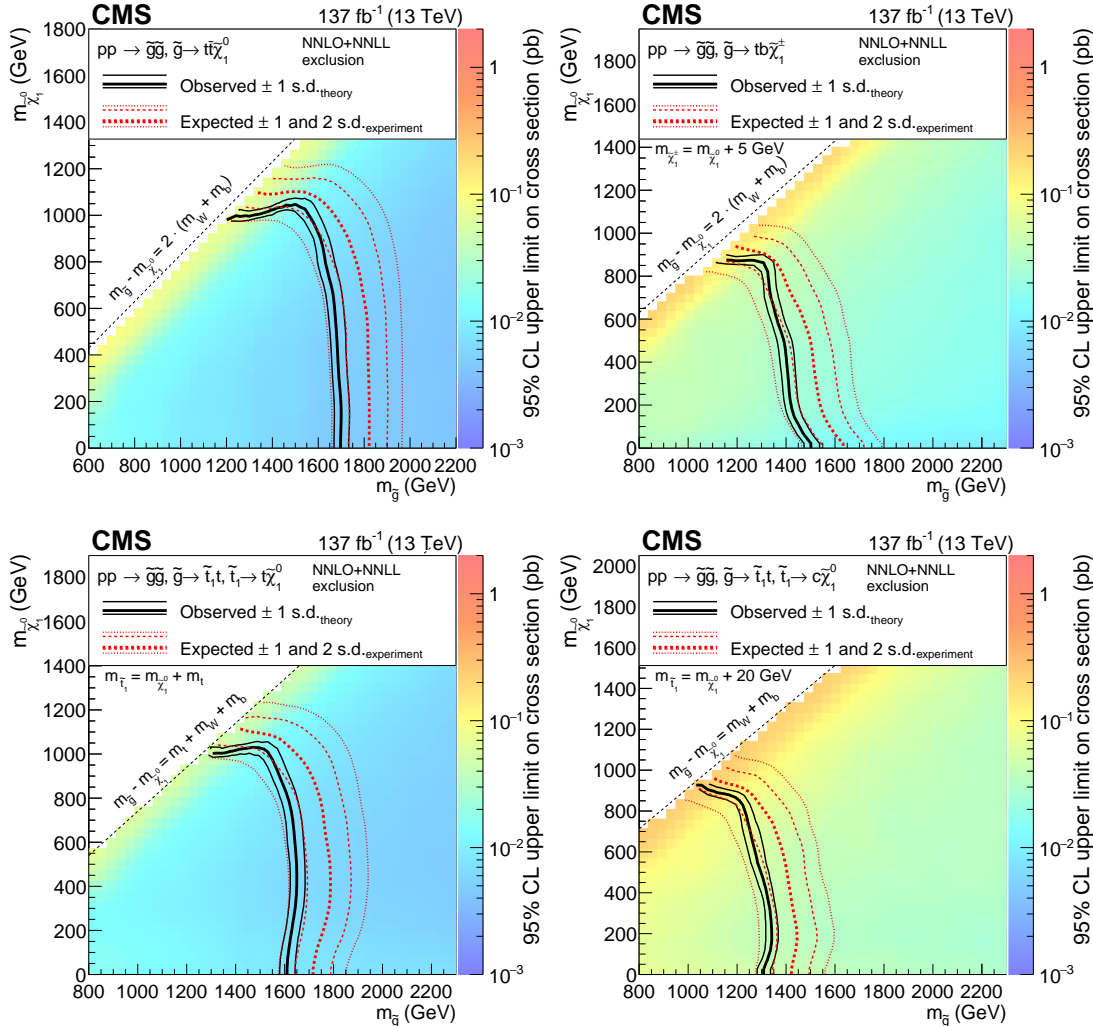


Figure 5.4: Exclusion regions at 95% CL in the  $m_{\tilde{\chi}_1^0}$  versus  $m_{\tilde{g}}$  plane for the T1tttt (upper left) and T5ttbbWW (upper right) models, with off-shell third-generation squarks, and the T5tttt (lower left) and T5ttcc (lower right) models, with on-shell third-generation squarks. For the T5ttbbWW model,  $m_{\tilde{\chi}_1^\pm} = m_{\tilde{\chi}_1^0} + 5 \text{ GeV}$ , for the T5tttt model,  $m_{\tilde{t}} - m_{\tilde{\chi}_1^0} = m_t$ , and for the T5ttcc model,  $m_{\tilde{t}} - m_{\tilde{\chi}_1^0} = 20 \text{ GeV}$  and the decay proceeds through  $\tilde{t} \rightarrow c\tilde{\chi}_1^0$ . The right-hand side color scale indicates the excluded cross section values for a given point in the SUSY particle mass plane. The solid black curves represent the observed exclusion limits assuming the approximate-NNLO+NNLL cross sections (thick line), or their variations of  $\pm 1$  standard deviations (s.d.) (thin lines). The dashed red curves show the expected limits with the corresponding  $\pm 1$  s.d. and  $\pm 2$  s.d. uncertainties. Excluded regions are to the left and below the limit curves.

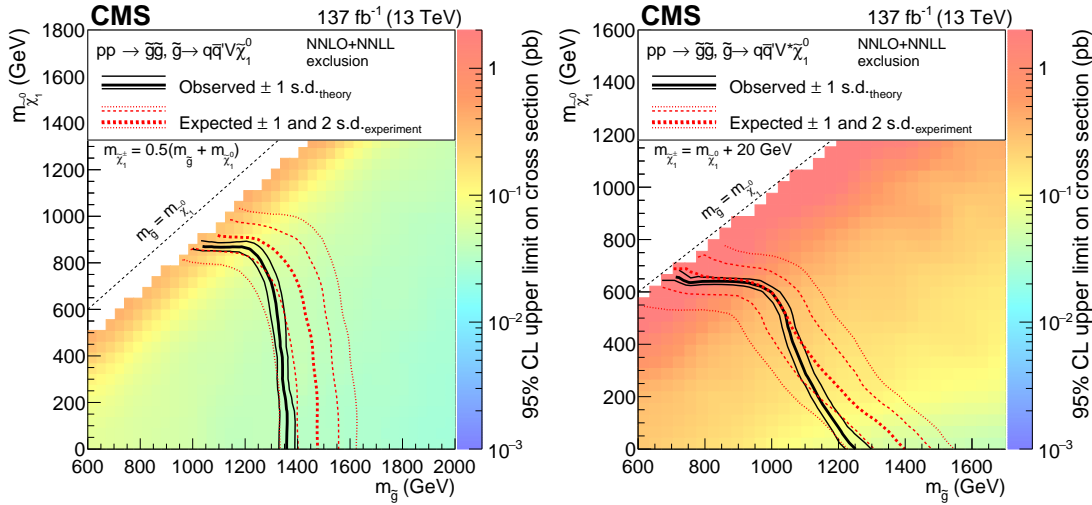


Figure 5.5: Exclusion regions at 95% CL in the plane of  $m_{\tilde{\chi}_1^0}$  versus  $m_{\tilde{g}}$  for the T5qqqqWZ model with  $m_{\tilde{\chi}_1^\pm} = 0.5(m_{\tilde{g}} + m_{\tilde{\chi}_1^0})$  (left) and with  $m_{\tilde{\chi}_1^\pm} = m_{\tilde{\chi}_1^0} + 20 \text{ GeV}$  (right). The notations are as in Fig. 5.4.

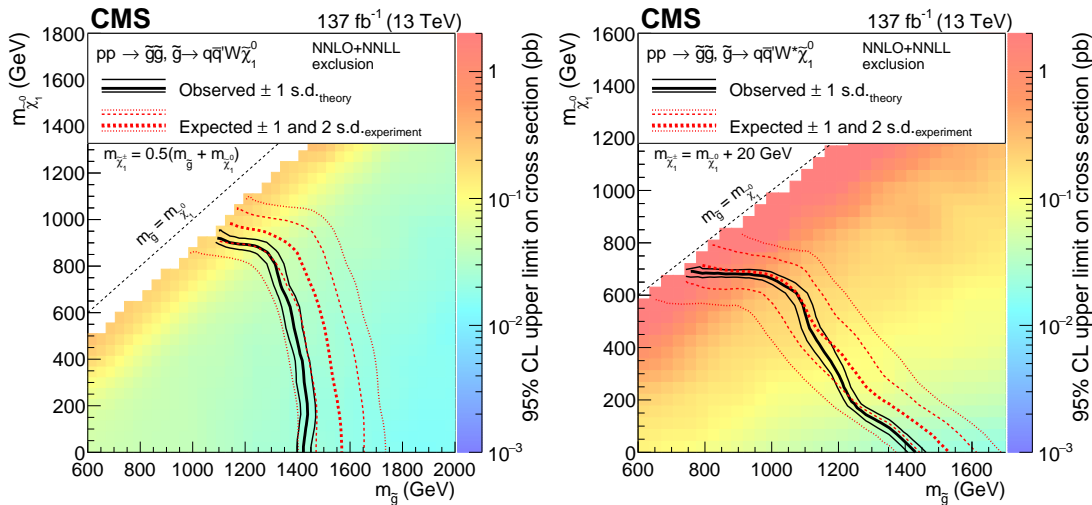


Figure 5.6: Exclusion regions at 95% CL in the plane of  $m_{\tilde{\chi}_1^0}$  versus  $m_{\tilde{g}}$  for the T5qqqqWW model with  $m_{\tilde{\chi}_1^\pm} = 0.5(m_{\tilde{g}} + m_{\tilde{\chi}_1^0})$  (left) and with  $m_{\tilde{\chi}_1^\pm} = m_{\tilde{\chi}_1^0} + 20 \text{ GeV}$  (right). The notations are as in Fig. 5.4.

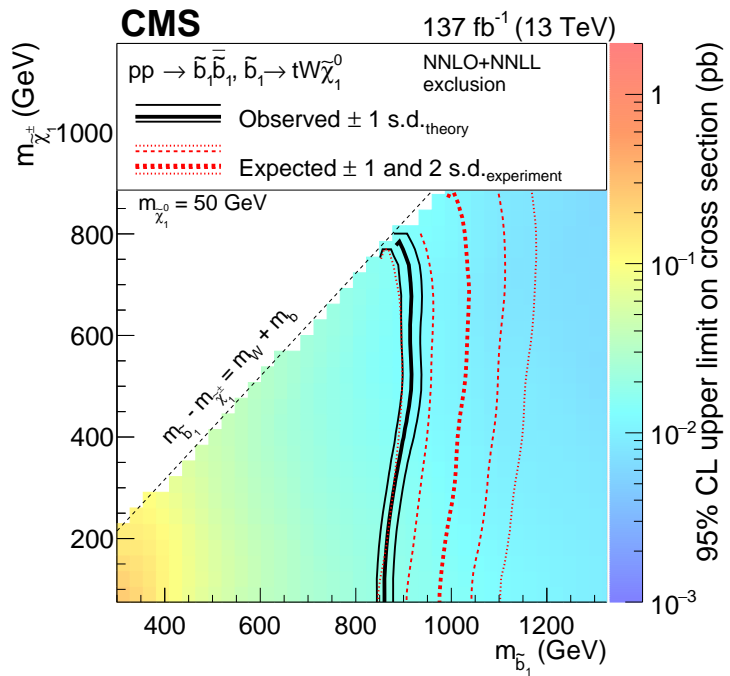


Figure 5.7: Exclusion regions at 95% CL in the plane of  $m_{\tilde{\chi}_1^\pm}$  versus  $m_{\tilde{b}_1}$  for the T6ttWW model with  $m_{\tilde{\chi}_1^0} = 50 \text{ GeV}$ . The notations are as in Fig. 5.4.

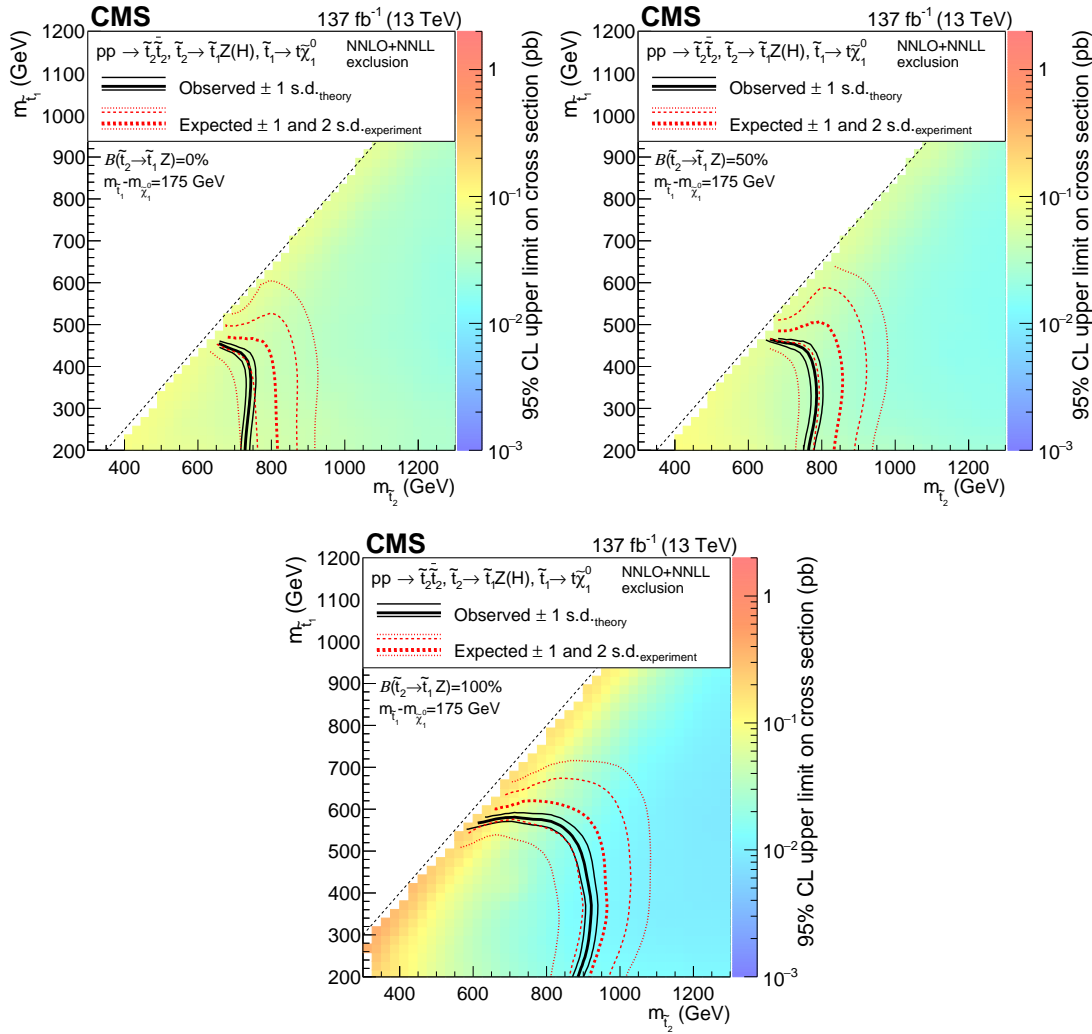


Figure 5.8: Exclusion regions at 95% CL in the plane of  $m(\tilde{t}_1)$  versus  $m(\tilde{t}_2)$  for the T6ttHZ model with  $m(\tilde{t}_1) - m(\tilde{\chi}_1^0) = 175$  GeV. The three exclusions represent  $\mathcal{B}(\tilde{t}_2 \rightarrow \tilde{t}_1 Z)$  of 0, 50, and 100%, respectively. The notations are as in Fig. 5.4.

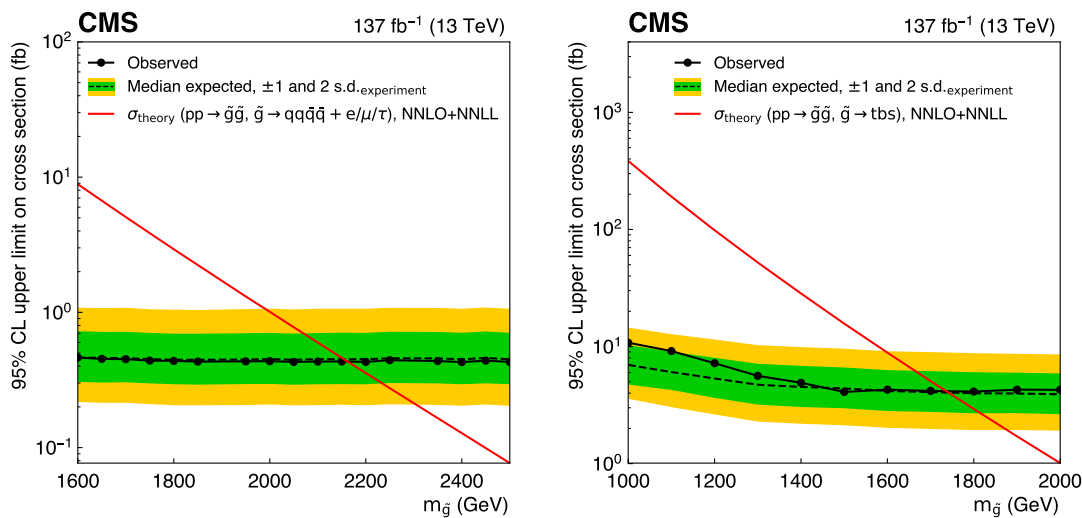


Figure 5.9: Upper limits at 95% CL on the cross section for RPV gluino pair production with each gluino decaying into four quarks and one lepton (T1qqqqL, left), and each gluino decaying into a top, bottom, and strange quarks (T1tbs, right).

### 5.2.2 Model-independent

For the generic production of an SS lepton pair with at least two jets and  $H_T > 300\text{GeV}$ , we set model-independent limits on the product of cross section, branching fraction, detector acceptance, and reconstruction efficiency. To do this, we select events from the HH and LM categories and calculate limits as a function of either the minimum  $p_T^{\text{miss}}$  or  $H_T$  requirements starting at 300 and 1400 GeV, respectively. Because there is an overlap between the two conditions, events that are selected for the limits as a function of  $H_T$  must also have  $p_T^{\text{miss}} < 300\text{GeV}$ . Both sets of limits are shown in Fig. 5.10.

In order to assist with future reinterpretations of the inclusive same-sign search results shown here, we calculated the expected and observed yields for a set of inclusive SRs, shown in Table 5.2.2. The last column in the table indicates the upper limit at 95% CL on the number of BSM events in each SR. The SRs are defined to have on the order of 5 to 10 expected background events, and we focus on events with large  $H_T$ ,  $p_T^{\text{miss}}$ ,  $N_b$ , and/or  $N_{\text{jets}}$ . No uncertainty in the signal acceptance is assumed in calculating the limits in the table.

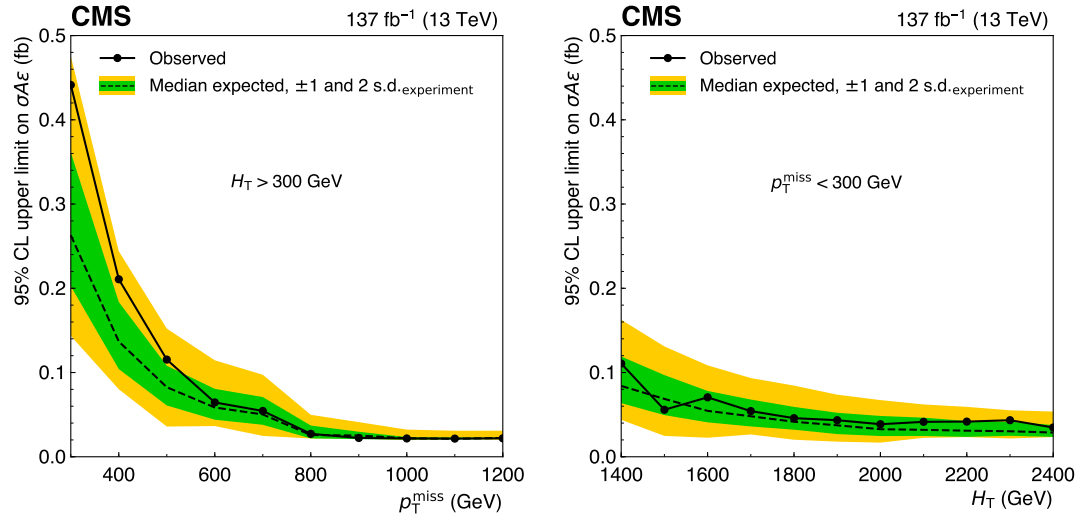


Figure 5.10: Upper limits at 95% CL on the product of cross section, detector acceptance, and selection efficiency,  $\sigma\mathcal{A}\epsilon$ , for the production of an SS lepton pair with at least two jets, as a function of the minimum  $p_T^{\text{miss}}$  threshold, when  $H_T > 300\text{GeV}$  (left), or the minimum  $H_T$  threshold, when  $p_T^{\text{miss}} < 300\text{GeV}$  (right).

SR	Category	$N_{\text{jets}}$	$N_b$	$H_T$ ( GeV)	$p_T^{\text{miss}}$ ( GeV)	$m_T^{\text{min}}$ ( GeV)	SM expected	Obs.	$N_{\text{BSM}}^{\text{max}}(95\% \text{ CL})$
ISR1	HH	$\geq 2$	0	$\geq 1000$	$\geq 250$	–	$12.7 \pm 7.4$	16	12.32
ISR2		$\geq 2$	$\geq 2$	$\geq 1100$	–	–	$11.0 \pm 3.8$	14	11.33
ISR3		$\geq 2$	0	–	$\geq 500$	–	$10.4 \pm 9.7$	13	11.26
ISR4		$\geq 2$	$\geq 2$	–	$\geq 300$	–	$11.4 \pm 3.8$	17	14.22
ISR5		$\geq 2$	0	–	$\geq 250$	$\geq 120$	$6.6 \pm 5.7$	10	10.77
ISR6		$\geq 2$	$\geq 2$	–	$\geq 200$	$\geq 120$	$6.3 \pm 1.3$	8	8.22
ISR7		$\geq 8$	–	–	–	–	$7.0 \pm 2.8$	12	12.17
ISR8		$\geq 6$	–	–	–	$\geq 120$	$6.2 \pm 1.4$	10	10.45
ISR9		$\geq 2$	$\geq 3$	$\geq 800$	–	–	$7.8 \pm 3.5$	8	7.53
ISR10	LL	$\geq 2$	–	$\geq 700$	–	–	$10.4 \pm 9.0$	12	10.37
ISR11		$\geq 2$	–	–	$\geq 200$	–	$12.1 \pm 5.6$	13	9.94
ISR12		$\geq 6$	–	–	–	–	$7.1 \pm 4.3$	7	7.10
ISR13		$\geq 2$	$\geq 3$	–	–	–	$1.61 \pm 0.39$	3	5.70
ISR14	LM	$\geq 2$	0	$\geq 1200$	<50	–	$3.6 \pm 3.6$	3	5.10
ISR15		$\geq 2$	$\geq 2$	$\geq 1000$	<50	–	$2.34 \pm 0.51$	4	6.41
ISR16	ML	$\geq 2$	0	$\geq 1000$	$\geq 300$	–	$5.6 \pm 1.6$	7	7.78
ISR17		$\geq 2$	$\geq 2$	$\geq 1000$	–	–	$5.7 \pm 1.9$	7	7.62

Table 5.3: Inclusive SR definitions, expected background yields and uncertainties, and observed yields, as well as the observed 95% CL upper limits on the number of BSM events contributing to each region. A dash (–) indicates that a particular selection is not required.

### 5.3 SM $t\bar{t}t\bar{t}$ results

Distributions of the main kinematic variables in the SM  $t\bar{t}t\bar{t}$  analysis ( $N_{\text{jets}}$ ,  $N_{\text{b}}$ ,  $H_{\text{T}}$ , and  $p_{\text{T}}^{\text{miss}}$ ) for events passing the baseline selections are shown in Fig. 5.11 and compared to the SM background predictions. The  $N_{\text{jets}}$  and  $N_{\text{b}}$  distributions for the  $t\bar{t}W$  and  $t\bar{t}Z$  control regions, CRW and CRZ, are shown in Fig. 5.12. In both figures, the expected SM  $t\bar{t}t\bar{t}$  signal is normalized to its predicted cross section. Again, fortunately (or unfortunately), *the SM predictions are statistically consistent with the observations.*

The yields from the SRs, CRZ, and CRW (for the cut-based analysis only), incorporating experimental and theoretical uncertainties as “nuisance” parameters, are used to construct a binned likelihood function. The measured cross section for  $t\bar{t}t\bar{t}$  and the statistical significance of the observation relative to the background-only hypothesis are obtained from a profile maximum-likelihood fit, in which the parameter of interest is  $\sigma(pp \rightarrow t\bar{t}t\bar{t})$  and all nuisance parameters are profiled, following the procedures described in Refs. [60, 69]. An upper limit at 95% confidence level (CL) is set on  $\sigma(pp \rightarrow t\bar{t}t\bar{t})$  using the  $\text{CL}_s$  criterion [58, 59], and asymptotic approximation [61]. Alternatively, by considering the SM, including the  $t\bar{t}t\bar{t}$  process with the SM cross section and uncertainty [28], as the null hypothesis, the fit provides cross section upper limits on BSM processes with new scalar and pseudoscalar particles, which will come into play when considering the interpretations in the upcoming sections.

While the values of most nuisance parameters are unchanged by the fit, the ones significantly affected include those corresponding to the  $t\bar{t}W$  and  $t\bar{t}Z$  normalizations,

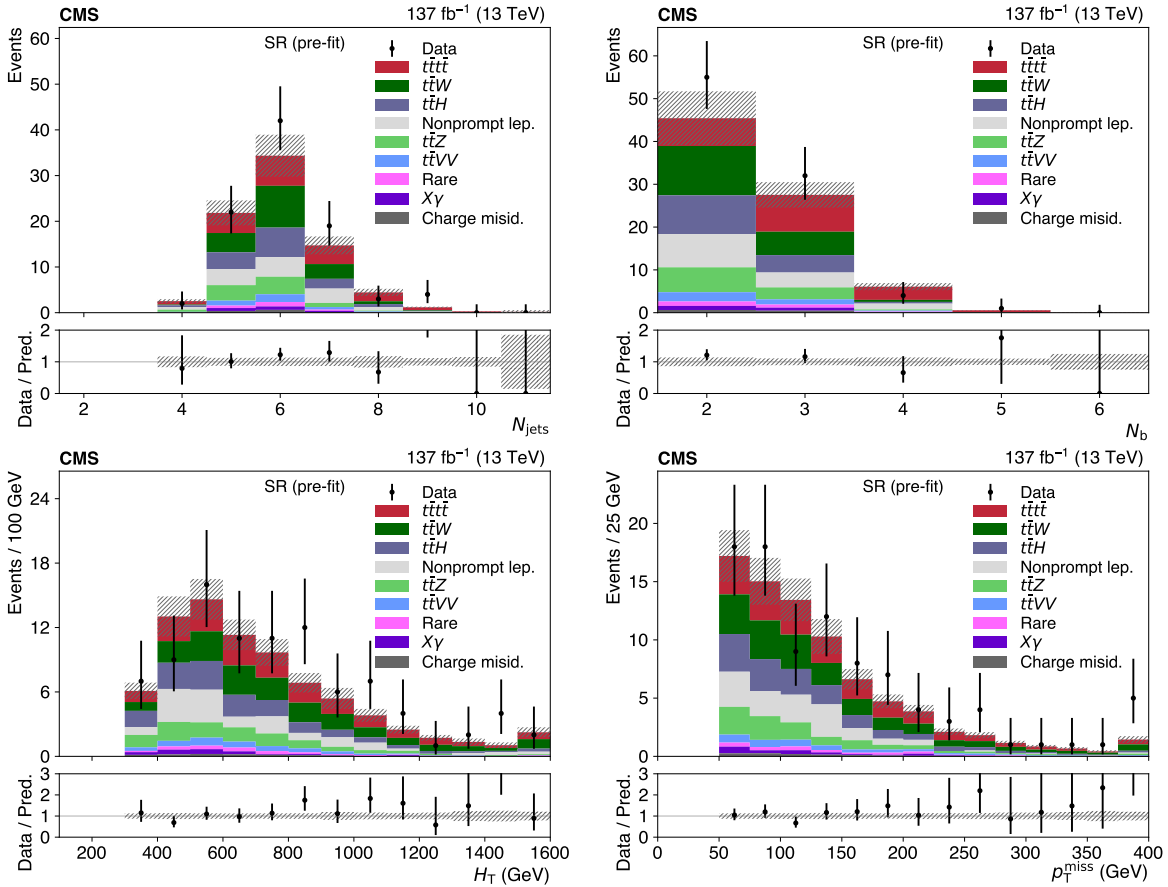


Figure 5.11: Distributions of  $N_{\text{jets}}$  (upper left),  $N_b$  (upper right),  $H_T$  (lower left), and  $p_T^{\text{miss}}$  (lower right) in the summed SRs (1–14), before fitting to data, where the last bins include the overflows. The hatched areas represent the total uncertainties in the SM signal and background predictions. The lower panels show the ratios of the observed event yield to the total prediction of signal plus background.

which are both scaled by  $1.3 \pm 0.2$  by the fit. This is in agreement with recent ATLAS and CMS measurements of these processes [70, 53, 71], which measures an underprediction of  $t\bar{t}W$  and  $t\bar{t}Z$  processes at NLO when compared to data, by approximately 20–30%. The post-fit predicted yields are compared to data in Fig. 5.14 for the cut-based and BDT analyses, where the fitted  $t\bar{t}t\bar{t}$  signal contribution is stacked on to the background predictions. The corresponding yields are shown in Tables 5.3 and 5.3 for the cut-based

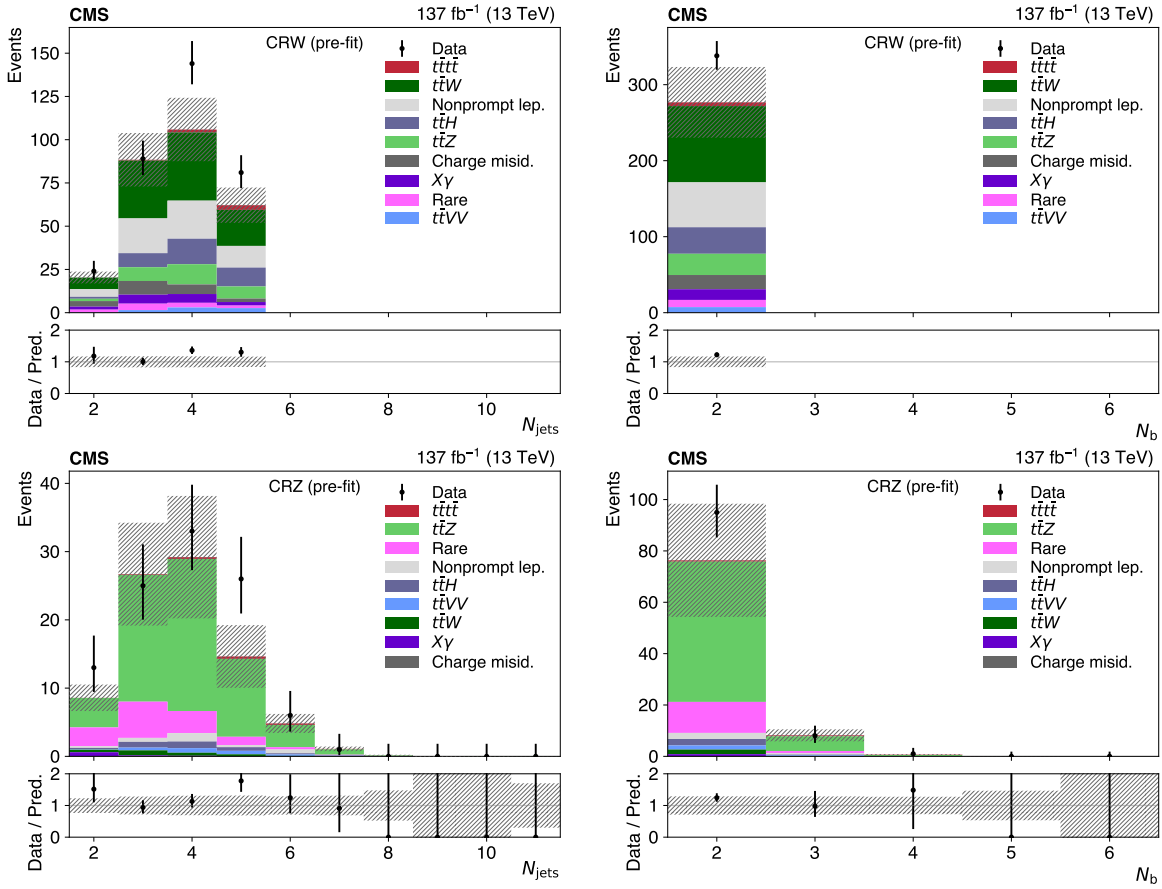


Figure 5.12: Distributions of  $N_{\text{jets}}$  (left) and  $N_b$  (right) in the  $t\bar{t}W$  (upper) and  $t\bar{t}Z$  (lower) CRs, before fitting to data. The hatched areas represent the uncertainties in the SM signal and background predictions. The lower panels show the ratios of the observed event yield to the total prediction of signal plus background.

and BDT analysis, respectively.

The  $t\bar{t}t\bar{t}$  cross section and the 68% CL interval is measured to be  $9.4^{+6.2}_{-5.6}$  fb in the cut-based analysis, and  $12.6^{+5.8}_{-5.2}$  fb in the BDT analysis. The likelihood curves for the latter analysis type are shown in Figure 5.13 Relative to the background-only hypothesis, the observed and expected significances are 1.7 and 2.5 standard deviations, respectively, for the cut-based analysis, and 2.6 and 2.7 standard deviations for the BDT analysis. The observed 95% CL upper limits on the cross section are 20.0 fb in the cut-based

and 22.5 fb in the BDT analyses. The corresponding expected upper limits on the  $t\bar{t}t\bar{t}$  cross section, assuming no SM  $t\bar{t}t\bar{t}$  contribution to the data, are  $9.4^{+4.3}_{-2.9}$  fb (cut-based) and  $8.5^{+3.9}_{-2.6}$  fb (BDT), a significant improvement relative to the value of  $20.8^{+11.2}_{-6.9}$  fb of Ref. [24]. Because it provides a higher expected measurement precision, we consider the BDT analysis as the primary result with which to perform further interpretations.

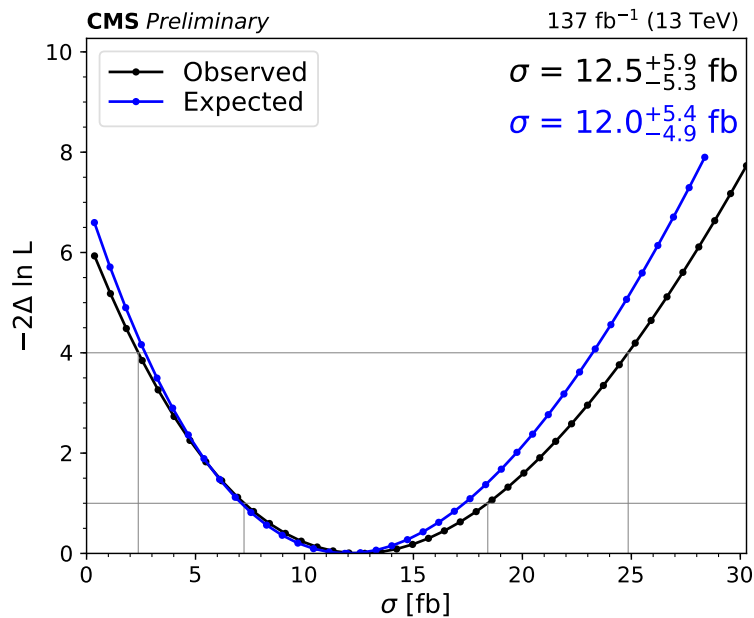


Figure 5.13: Observed/expected log-likelihood curves with the BDT analysis.

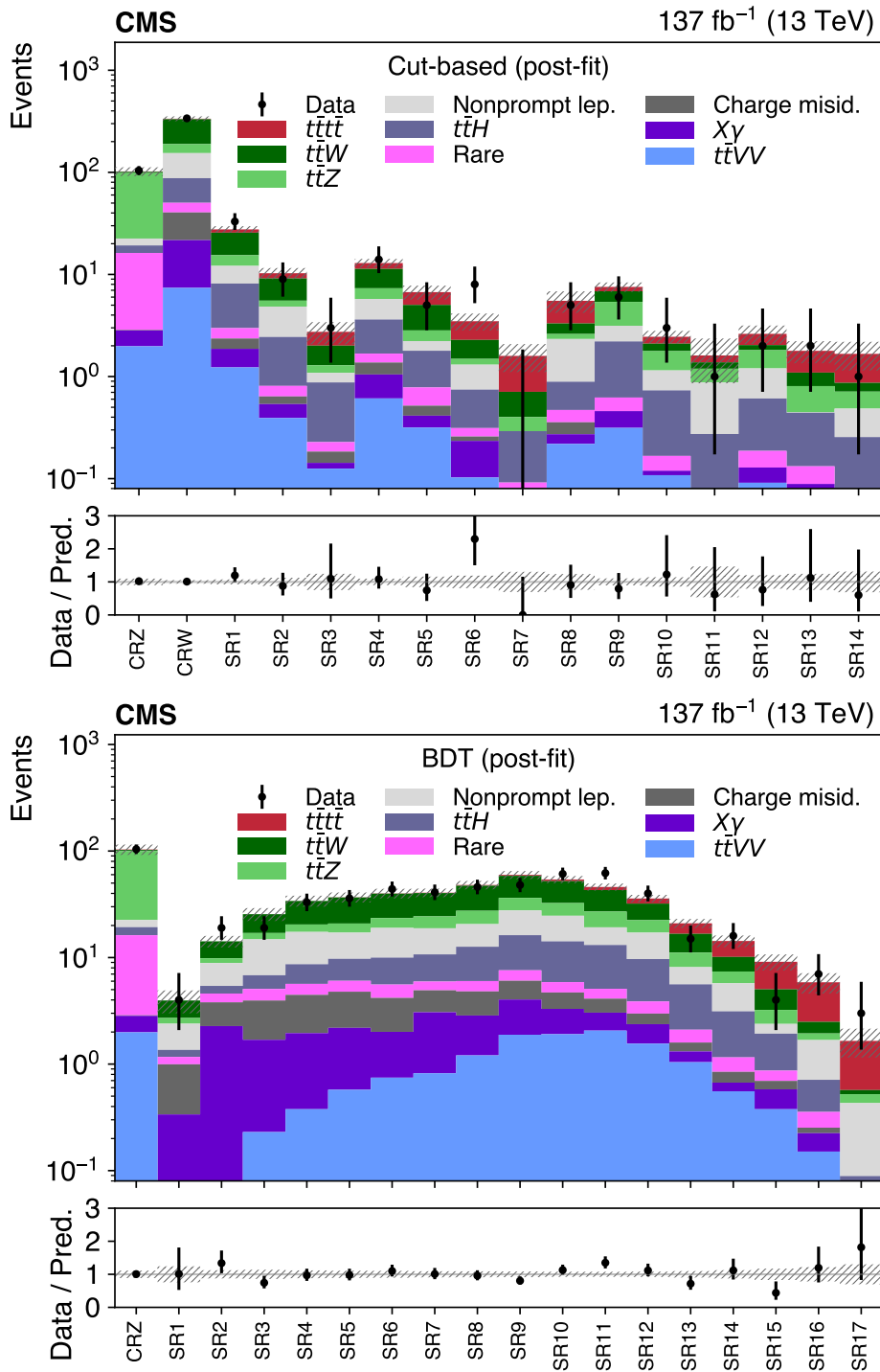


Figure 5.14: Observed yields in the control and signal regions for the cut-based (upper) and BDT (lower) analyses, compared to the post-fit predictions for signal and background processes. The hatched areas represent the total post-fit uncertainties in the signal and background predictions. The lower panels show the ratios of the observed event yield to the total prediction of signal plus background.

	SM background	$t\bar{t}t\bar{t}$	Total	Observed
CRZ	$101 \pm 10$	$0.83 \pm 0.49$	$102 \pm 10$	104
CRW	$331 \pm 19$	$3.9 \pm 2.3$	$335 \pm 18$	338
SR1	$25.6 \pm 2.1$	$2.0 \pm 1.2$	$27.6 \pm 2.1$	33
SR2	$9.1 \pm 1.3$	$1.13 \pm 0.65$	$10.3 \pm 1.3$	9
SR3	$2.01 \pm 0.58$	$0.73 \pm 0.42$	$2.74 \pm 0.67$	3
SR4	$11.3 \pm 1.3$	$1.58 \pm 0.90$	$12.9 \pm 1.3$	14
SR5	$5.03 \pm 0.77$	$1.68 \pm 0.95$	$6.7 \pm 1.1$	5
SR6	$2.29 \pm 0.40$	$1.20 \pm 0.67$	$3.48 \pm 0.66$	8
SR7	$0.71 \pm 0.20$	$0.88 \pm 0.48$	$1.59 \pm 0.49$	0
SR8	$3.31 \pm 0.95$	$2.2 \pm 1.3$	$5.5 \pm 1.3$	5
SR9	$6.84 \pm 0.80$	$0.71 \pm 0.39$	$7.55 \pm 0.80$	6
SR10	$2.10 \pm 0.31$	$0.35 \pm 0.22$	$2.45 \pm 0.35$	3
SR11	$1.38 \pm 0.75$	$0.23 \pm 0.14$	$1.61 \pm 0.75$	1
SR12	$2.03 \pm 0.48$	$0.59 \pm 0.34$	$2.62 \pm 0.54$	2
SR13	$1.09 \pm 0.28$	$0.69 \pm 0.39$	$1.78 \pm 0.44$	2
SR14	$0.87 \pm 0.30$	$0.80 \pm 0.45$	$1.67 \pm 0.52$	1

Table 5.4: The post-fit predicted background,  $t\bar{t}t\bar{t}$  signal, and total yields with their total uncertainties and the observed number of events in the control and signal regions in data for the cut-based analysis.

	SM background	$t\bar{t}t\bar{t}$	Total	Observed
CRZ	$102 \pm 12$	$1.11 \pm 0.43$	$103 \pm 12$	104
SR1	$3.95 \pm 0.96$	$< 0.01$	$3.96 \pm 0.96$	4
SR2	$14.2 \pm 1.8$	$0.01 \pm 0.01$	$14.2 \pm 1.8$	19
SR3	$25.5 \pm 3.5$	$0.04 \pm 0.03$	$25.6 \pm 3.5$	19
SR4	$34.0 \pm 4.0$	$0.08 \pm 0.05$	$34.0 \pm 4.0$	33
SR5	$36.7 \pm 4.0$	$0.15 \pm 0.07$	$36.8 \pm 4.0$	36
SR6	$39.8 \pm 4.2$	$0.23 \pm 0.12$	$40.0 \pm 4.2$	44
SR7	$40.3 \pm 3.7$	$0.31 \pm 0.16$	$40.6 \pm 3.8$	41
SR8	$47.3 \pm 4.3$	$0.72 \pm 0.28$	$48.0 \pm 4.3$	46
SR9	$58.5 \pm 5.2$	$1.18 \pm 0.46$	$59.7 \pm 5.2$	48
SR10	$52.1 \pm 4.3$	$1.91 \pm 0.74$	$54.1 \pm 4.2$	61
SR11	$43.0 \pm 3.5$	$3.0 \pm 1.2$	$46.0 \pm 3.5$	62
SR12	$32.1 \pm 3.0$	$3.7 \pm 1.4$	$35.8 \pm 2.9$	40
SR13	$16.7 \pm 1.6$	$4.3 \pm 1.6$	$21.0 \pm 2.0$	15
SR14	$10.1 \pm 1.2$	$4.2 \pm 1.6$	$14.3 \pm 1.8$	16
SR15	$5.03 \pm 0.77$	$4.1 \pm 1.5$	$9.1 \pm 1.6$	4
SR16	$2.49 \pm 0.61$	$3.4 \pm 1.3$	$5.9 \pm 1.3$	7
SR17	$0.57 \pm 0.36$	$1.08 \pm 0.42$	$1.65 \pm 0.50$	3

Table 5.5: The post-fit predicted background and  $t\bar{t}t\bar{t}$  signal, and total yields with their total uncertainties and the observed number of events in the control and signal regions in data for the BDT analysis.

## 5.4 SM $t\bar{t}t\bar{t}$ interpretations

The BDT-based results are used to constrain SM parameters, as well as production of BSM particles and operators that can affect the  $t\bar{t}t\bar{t}$  production rate. The existence of  $t\bar{t}t\bar{t}$  Feynman diagrams with virtual Higgs bosons allows interpreting the upper limit on  $\sigma(pp \rightarrow t\bar{t}t\bar{t})$  as a constraint on the Yukawa coupling,  $y_t$ , between the top quark and the Higgs boson, as introduced in Section 2.2.2.1. Similarly, the measurement can be interpreted as a constraint on the Higgs boson oblique parameter  $\hat{H}$ , as described in Section 2.2.2.3. Feynman diagrams where the virtual Higgs boson is replaced by a virtual BSM scalar ( $\phi$ ) or vector ( $Z'$ ) particle with mass smaller than twice the top quark mass ( $m < 2m_t$ ), are used to interpret the result as a constraint on the couplings of such new particles, as described in Section 2.2.2.2. In addition, new particles with  $m > 2m_t$ , such as a heavy scalar (H) or pseudoscalar (A), can be produced on-shell in association with top quarks. They can subsequently decay into top quark pairs, generating final states with three or four top quarks. Constraints on the production of such heavy particles can be interpreted in terms of 2HDM parameters (as described in Section 2.2.1.1) or in the framework of simplified models of dark matter (as described in Section 2.2.1.2).

### 5.4.1 Top quark yukawa coupling

When using the  $t\bar{t}t\bar{t}$  results to determine a constraint on  $y_t$ , we take into account the dependence of the backgrounds on  $y_t$  by scaling the  $t\bar{t}H$  cross section by  $|y_t/y_t^{\text{SM}}|^2$  prior to the fit, where  $y_t^{\text{SM}}$  represents the SM value of the top quark Yukawa coupling. As a

result of the  $t\bar{t}H$  background rescaling, the measured  $\sigma(pp \rightarrow t\bar{t}t\bar{t})$  depends on  $|y_t/y_t^{\text{SM}}|$ , as shown in Fig. 5.15, becoming smaller at higher values of  $y_t$ . The measurement is compared to the theoretical prediction obtained from Ref. [37], scaled to the latest NLO cross section for  $t\bar{t}t\bar{t}$ ,  $12.0^{+2.2}_{-2.5}$  fb. Comparing the observed limit on  $\sigma(pp \rightarrow t\bar{t}t\bar{t})$  with the central, upper, and lower values of its theoretical prediction, we obtain 95% CL limits of  $|y_t/y_t^{\text{SM}}| < 1.7$ , 1.4, and 2.0, respectively, improving on the previous CMS  $t\bar{t}t\bar{t}$  result [24]. The  $y_t$  constant affects the Higgs boson production cross section in both the gluon fusion and  $t\bar{t}H$  modes, so constraints can also be obtained from a combination of Higgs boson measurements [72], however, these constraints require assumptions about the total width of the Higgs boson, while the  $t\bar{t}t\bar{t}$ -based limit presented here does not.

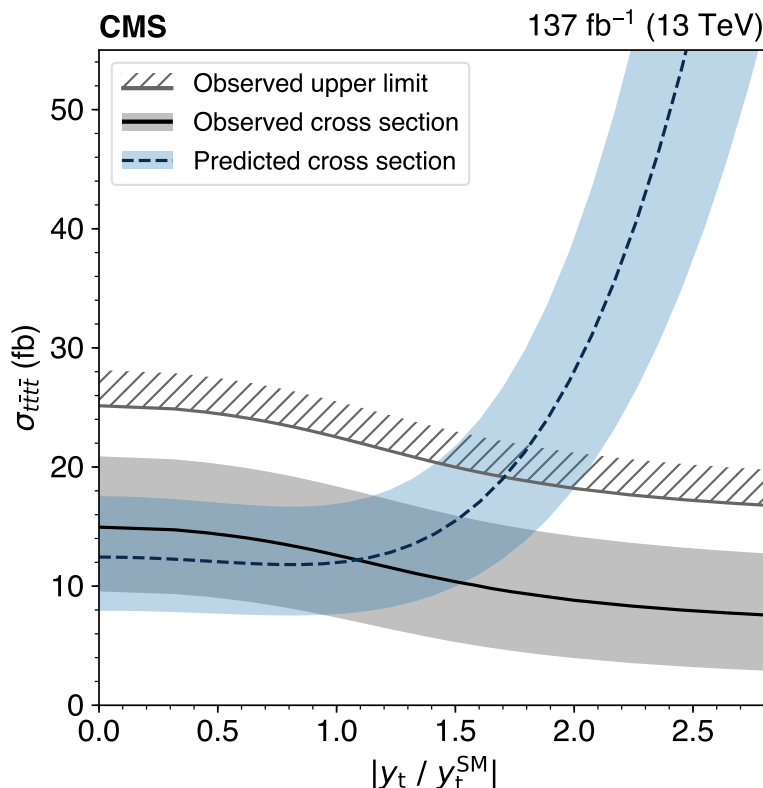


Figure 5.15: The observed  $\sigma(pp \rightarrow t\bar{t}t\bar{t})$  (solid line) and 95% CL upper limit (hatched line) are shown as a function of  $|y_t/y_t^{\text{SM}}|$ . The predicted value (dashed line) [37], calculated at LO and scaled to the calculation from Ref. [28], is also plotted. The shaded band around the measured value gives the total uncertainty, while the shaded band around the predicted curve shows the theoretical uncertainty associated with the renormalization and factorization scales.

### 5.4.2 Oblique Higgs parameter

To calculate an upper limit of  $\hat{H}$ , the BDT analysis is repeated several times using simulated samples of  $t\bar{t}t\bar{t}$  signal events with different values of  $\hat{H}$  to account for small acceptance and kinematic differences. During each fit, we rescale the  $t\bar{t}H$  cross section by  $(1-\hat{H})^2$  due to its  $\hat{H}$  dependency. This results in the 95% CL upper limit of  $\hat{H} < 0.12$ . For reference, using recent LHC on-shell Higgs boson measurements, the authors of Ref. [39] obtained a constraint of  $\hat{H} < 0.16$  at 95% CL.

### 5.4.3 Off-shell particles

In order to study the off-shell effect of new particles with  $m < 2m_t$ , we first consider neutral scalar ( $\phi$ ) and neutral vector ( $Z'$ ) particles that couple to top quarks. Based on simulation, these new particles affect the signal acceptance by less than 10%, so we recalculate the  $\sigma(pp \rightarrow t\bar{t}t\bar{t})$  upper limit of the BDT analysis including an additional 10% uncertainty in the acceptance, and obtain the 95% CL upper limit of 23.0 fb on the total  $t\bar{t}t\bar{t}$  cross section, slightly weaker than the nominal limit of 22.5 fb. Comparing this upper limit to the predicted cross section in models where  $t\bar{t}t\bar{t}$  production includes a  $\phi$  or a  $Z'$  in addition to SM contributions, we set limits on the masses and couplings of these new particles, shown in Fig. 5.16. These two-dimensional limits exclude couplings larger than 1.2 for  $m_\phi$  in the 25–340 GeV range and larger than 0.1 (0.9) for  $m_{Z'} = 25$  (300) GeV.

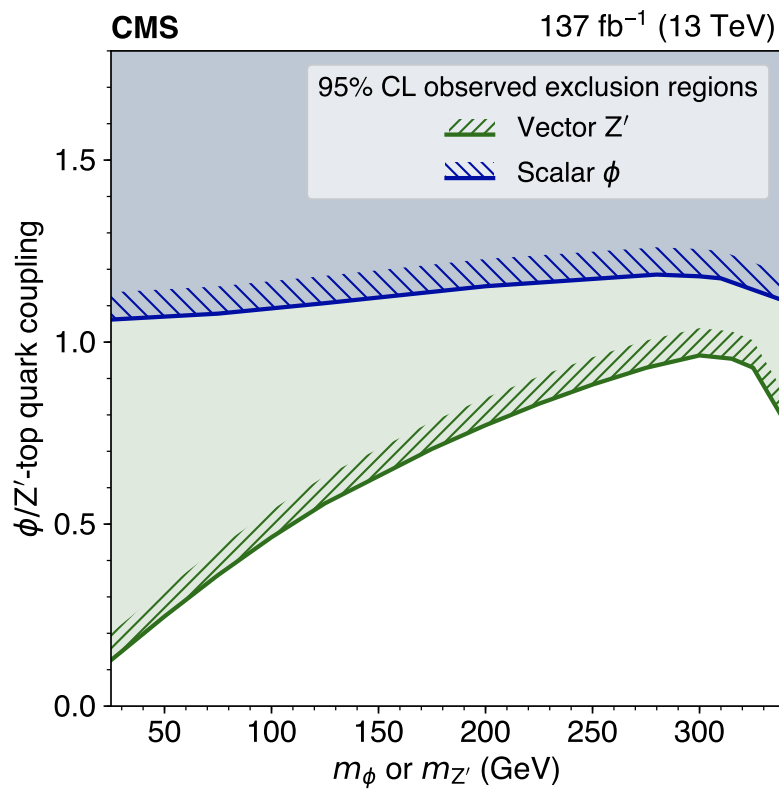


Figure 5.16: The 95% CL exclusion regions in the plane of the  $\phi/Z'$ -top quark coupling versus  $m_\phi$  or  $m_{Z'}$ . The excluded regions are above the hatched lines.

### 5.4.4 On-shell particles

We finally consider on-shell effects from new scalar and pseudoscalar particles with  $m > 2m_t$ . The production rate of these particles in association with a single top quark ( $tqH/A$ ,  $tWH/A$ ) is significant, so we include these processes in addition to  $t\bar{t}H/A$ . These processes also do not suffer significant interference with the SM  $t\bar{t}t\bar{t}$  process. To obtain upper limits on the sum of these processes followed by the decay  $H/A \rightarrow t\bar{t}$ , we use the BDT analysis and treat the SM  $t\bar{t}t\bar{t}$  process as a background. Figure 5.17 shows excluded cross sections as a function of the mass of the scalar and pseudoscalar particles. Comparing these limits with the Type-II 2HDM cross sections with  $\tan\beta = 1$  in the alignment limit, we exclude scalar (pseudoscalar) masses up to 470 (550) GeV, which improves the limits from a previous CMS analysis [25] by more than 100 GeV. Similarly, we consider a simplified model of dark matter which includes a Dirac fermion dark matter candidate,  $\chi$ , in addition to  $H/A$ , and where the couplings of  $H/A$  to SM fermions and  $\chi$  are determined by parameters  $g_{\text{SM}}$  and  $g_{\text{DM}}$ , respectively. Exclusions similar to those from 2HDM are reached by assuming  $g_{\text{SM}} = 1$  and  $g_{\text{DM}} = 1$ , and taking  $m_{H/A} < 2m_\chi$ . Relaxing the 2HDM assumption of  $\tan\beta = 1$ , Fig. 5.18 shows the 2HDM limit as a function of  $H/A$  mass and  $\tan\beta$ , considering one new particle at a time and also including a scenario with  $m_H = m_A$ . Values of  $\tan\beta$  up to 0.8–1.6 are excluded. These exclusions are comparable to those of a recent CMS search for the resonant production of  $H/A$  in the  $p \rightarrow H/A \rightarrow t\bar{t}$  channel [73]. Relaxing the  $m_{H/A} < 2m_\chi$  assumption in the dark matter model, we obtain Fig. 5.19, which shows the limit as a function of the

masses of both  $H/A$  and  $\chi$ , for  $g_{\text{DM}} = 1$  and for two different assumptions of  $g_{\text{SM}}$ . Large sections of the phase space are excluded, which is complementary to that of analyses considering invisible decays of  $H/A$  such as in Refs. [35, 74].

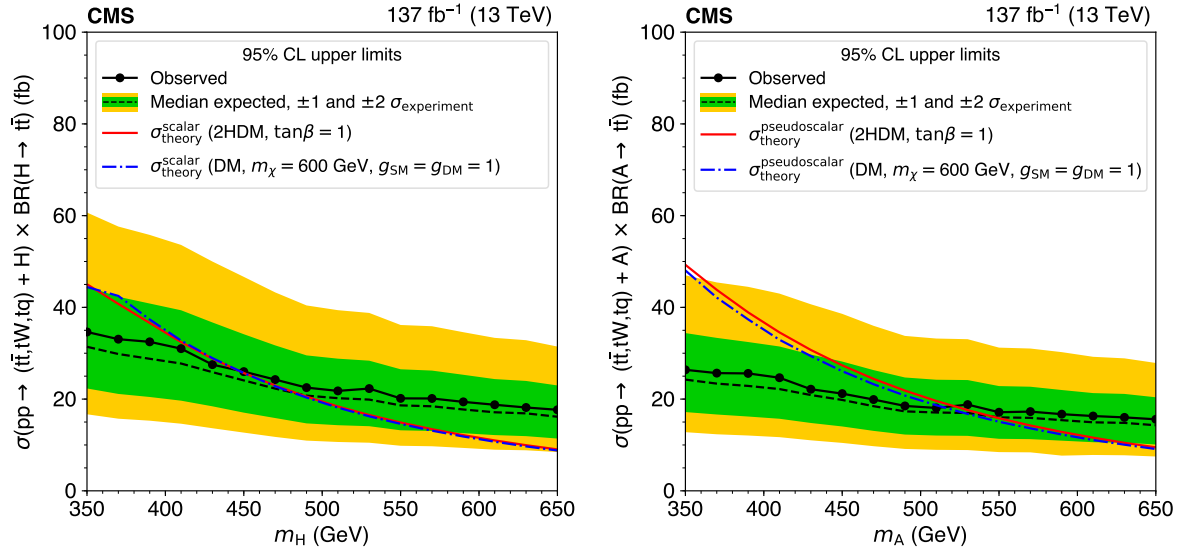


Figure 5.17: The observed (points) and expected (dashed line) 95% CL upper limits on the cross section times branching fraction to  $t\bar{t}$  for the production of a new heavy scalar  $H$  (left) and pseudoscalar  $A$  (right), as a function of mass. The inner and outer bands around the expected limits indicate the regions containing 68 and 95%, respectively, of the distribution of limits under the background-only hypothesis. Theoretical values are shown for Type-II 2HDM in the alignment limit (solid line) and simplified dark matter (dot-dashed line) models.

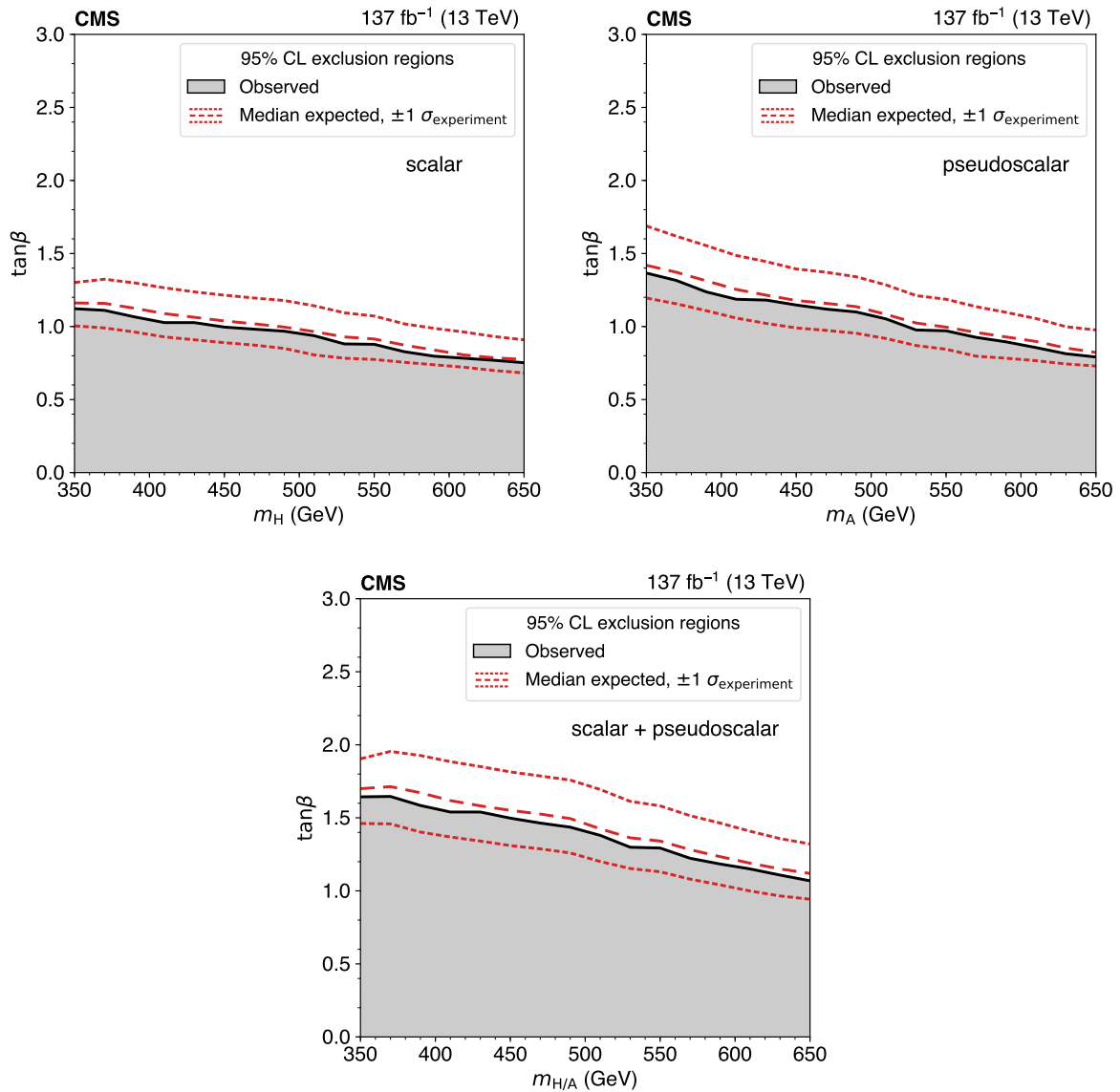


Figure 5.18: The observed (solid curve) and expected (long-dashed curve) 95% CL exclusion regions in the  $\tan\beta$  versus mass plane for Type-II 2HDM models in the alignment limit for a new scalar H (upper left), pseudoscalar A (upper right), and both (lower) particles. The short-dashed curves around the expected limits indicate the region containing 68% of the distribution of limits expected under the background-only hypothesis. The excluded regions are below the curves.

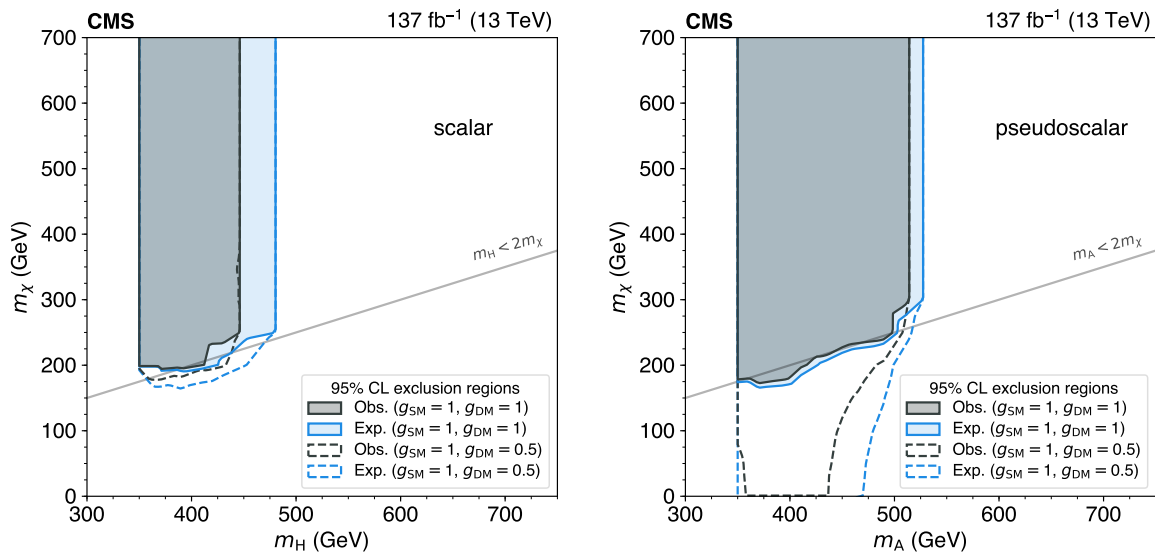


Figure 5.19: Exclusion regions at 95% CL in the plane of  $m_\chi$  vs.  $m_H$  (left) or  $m_A$  (right). The outer lighter and inner darker solid curves show the expected and observed limits, respectively, assuming  $g_{\text{SM}} = g_{\text{DM}} = 1$ . The excluded regions, shaded, are above the limit curves. The dashed lines show the limits assuming a weaker coupling between  $H/A$  and  $\chi$ ,  $g_{\text{DM}} = 0.5$ .

# Chapter 6

## Summary and conclusions

A sample of events with two same-sign or at least three charged leptons produced in association with several jets in proton-proton collisions at 13 TeV, corresponding to an integrated luminosity of  $137\text{fb}^{-1}$ , has been studied to search for physics beyond the standard model, as well as for the standard model (SM) production of four top quarks.

In the inclusive BSM analysis, no significant excesses were found and the results are interpreted as limits on cross sections at 95% confidence level for the production of new particles in simplified supersymmetric models, considering both R parity conserving and violating scenarios. The limits are translated into lower mass limits that are as large as 2.1 TeV for gluinos and 0.9 TeV for top and bottom squarks. To assist with future re-interpretations, model-independent limits are provided as a function of the missing transverse momentum and the scalar sum of jet transverse momenta in an event.

The SM four top quark production search analyzed the dataset using two strategies,

the first relying on a cut-based categorization in lepton multiplicity, jet multiplicity, and jet flavor, and the second taking advantage of a boosted decision tree (BDT) to distinguish the  $t\bar{t}t\bar{t}$  signal from backgrounds. The more precise multivariate strategy yields an observed (expected) significance of 2.6 (2.7) standard deviations relative to the background-only hypothesis, and a measured value for the  $t\bar{t}t\bar{t}$  cross section of  $12.6^{+5.8}_{-5.2}$  fb. The results based on the two strategies are in agreement with the SM prediction of  $12.0^{+2.2}_{-2.5}$  fb. The results of the BDT approach are used to constrain the top quark Yukawa coupling,  $y_t$ , resulting in the 95% confidence level (CL) limit of  $|y_t/y_t^{\text{SM}}| < 1.7$ . The Higgs boson oblique parameter in the effective field theory framework [39] is similarly constrained to  $\hat{H} < 0.12$  at 95% CL. Upper limits between 0.1 and 1.2 are also set on the coupling between the top quark and a new scalar ( $\phi$ ) or vector ( $Z'$ ) particle with mass less than twice that of the top quark ( $m_t$ ) [38]. Considering new scalar or pseudoscalar particles with  $m > 2m_t$ , and decaying to  $t\bar{t}$ , their production in association with one or two top quarks is probed. The resulting cross section upper limit, between 15 and 35 fb at 95% CL, is interpreted in the contexts of Type-II two-Higgs-doublet models and simplified dark matter models.

What a mouthful! In other words, the meta-summary is: the data collected by the CMS detector from 2016 to 2018 did not turn up any interesting hints of new physics in the same-sign final state. However, in the coming years, the High-Luminosity LHC project seeks to at least double the dataset size analyzed here. This will undoubtedly allow SM  $t\bar{t}t\bar{t}$  measurement to pass the  $3-\sigma$  evidence threshold, and maybe we will see

hints of new physics.

# Appendix A

## Statistics

### A.1 Profile likelihood

This section presents an introduction to the profile likelihood method (used for the statistical results of this thesis) with a concrete toy example. The frequentist toy example consists of one signal, one background, and one shape-based nuisance parameter. Complete details of the method are in Reference [61].

#### A.1.1 Terminology

Bayes' theorem can be stated in a more applicable way as

$$p(k|D) = \frac{p(D|k)p(k)}{p(D)} \quad (\text{A.1})$$

where  $p(A|B)$  is the (conditional) probability of A given B. Here,  $k$  represents a model, which consists of a set of parameters (parameters of interest, as well as annoying/nuisance parameters). Typically, the single parameter of interest is a signal “strength”  $\mu$  (how much signal is there actually, compared to what is nominally in the simulation –  $\mu = \mu_{\text{obs}}/\mu_{\text{SM}}$ ), and a set of (many) nuisance parameters technically specified as a vector  $\vec{\theta}$ , but could be just  $\theta$ . The posterior probability distribution function (pdf),  $p(k|D)$  is the distribution of parameters given the observed data D. The **likelihood**  $p(D|k)$  gives the likelihood of getting some data  $D$  given a particular model encoded in  $k$ .  $p(k)$  is a prior distribution of models, often taken to be “flat” in  $\mu$ . Lastly, the overall constant  $p(D)$  is ignorable when dealing with differences in likelihoods.

Analysis observables are typically binned into many regions, and compared with an observed count (data). Integral data event counts ( $N$ ) obey Poisson statistics, where  $\lambda$  governs the underlying rate of a process:  $p(N|\lambda) = e^{-\lambda} \frac{\lambda^N}{N!}$ . (Although, when statistics are large, Gaussian approximations can be made in order to simplify computations.) For independent bins, the likelihood is a product over each of the bins.

This sets the stage for the toy example, which clarifies the meaning of the word **profile**.

### A.1.2 Toy example

Figure A.1 shows a toy distribution of jet multiplicity for background, signal, and data. The background component also contains a systematic uncertainty band corre-

sponding to a shape nuisance parameter. This shape nuisance parameter prefers to increase yields at higher number of jets.

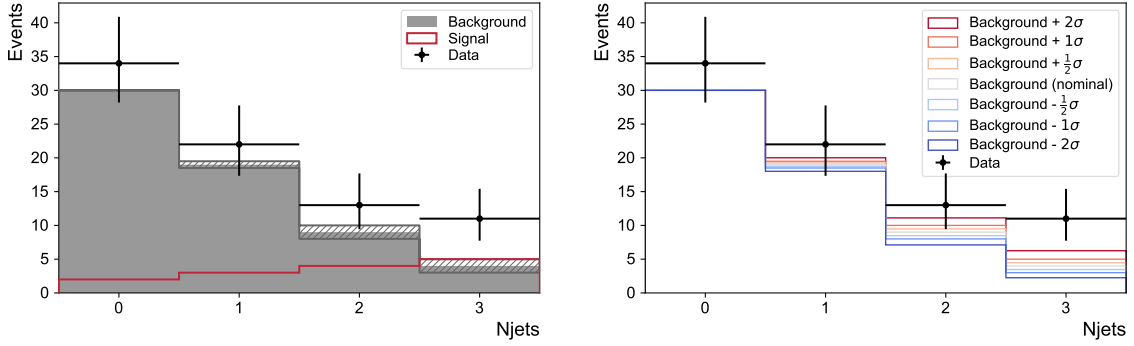


Figure A.1: Toy distribution (left) and single shape nuisance variation on background component (right)

As an intermediate goal to most statistical results/interpretations of the data, we want to compute the likelihood which will be a 2D function of the signal strength  $\mu$  and the value of the systematic variation  $\theta$ .  $\theta = 0$  will give the normal background yields, while  $\theta = -1$  and  $\theta = 1$  will give the  $1\sigma$  down and up variations, respectively. From above,  $\theta = 1$  will absorb the signal, as it increases the background yield at high number of jets.

The likelihood function is the binned probability to get the data from a  $b$  (background-only) or  $s+b$  (background and signal) poisson distribution, accounting for the probability of nuisances  $\theta$  with the pdf  $p(\theta)$ :

$$\mathcal{L}(\text{data}|\mu, \theta) = \prod_{j \in \text{bins}} \frac{(\mu s_j + b_j)^{n_j}}{n_j!} e^{-(\mu s_j + b_j)} p(\theta) \quad (\text{A.2})$$

here  $n_j$  represents the data count in bin  $j$ ,  $b_j$  the background count, and  $s_j$  the signal

count. Technically,  $b_j$  is a function of  $\theta$ ; that is,  $b_j(\theta)$  depends on the value of the systematic variation where  $b_j(0)$  is the nominal background yield.

The goal is find maxima in the likelihood scan. However, numbers can get very large given the factorial and the exponential. Since the  $\ln$  function is monotonically increasing, to make things numerically tractable and simpler, we take the (negative) log since minimization problems are easier than maximization.

$$-\ln \mathcal{L} = -\sum_{j=0}^3 [n_j \ln(\mu s_j + b_j) - \ln(n_j!) - (\mu s_j + b_j) + \ln(p(\theta))] \quad (\text{A.3})$$

Even though it won't matter in the end (since we ultimately care about relative differences in the likelihood) note that  $\ln(n_j!)$  is just  $\sum_{i=0}^3 \ln(i)$  and it is independent of  $\mu$  and  $\theta$ , so it can usually be pre-computed.

We can then calculate likelihood values over the  $\mu$ - $\theta$  plane. Figure A.2 shows this two dimensional likelihood scan as a function of  $\theta$  and  $\mu$ , with contours overlaid, as well as the global maximum log likelihood (the minimum *negative* log likelihood). The plot also shows the maximum likelihood as a function of  $\mu$  with a red line. Equivalently, this gives the nuisance parameter value that maximizes the likelihood for a fixed  $\mu$ .

From the two dimensional scan, we see the maximum global likelihood occurs when the signal strength parameter  $\mu$  is 1.27. This roughly makes sense given the histogram templates which had 5 signal, 4 background, and 11 observed events in the last bin. This bin dominates the result due to the strong signal presence. With the fitted signal strength,  $5 \times 1.27 + 4 \approx 11$ .

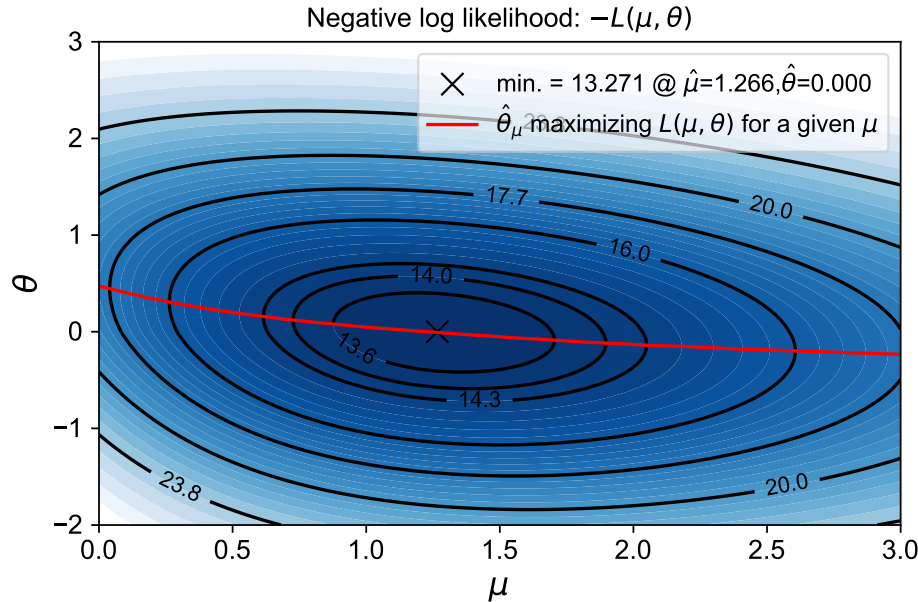


Figure A.2: Two dimensional likelihood scan as a function of  $\theta$  and  $\mu$ . The red line shows the maximum likelihood for a given  $\mu$ .

For lower values of  $\mu$ , the best likelihood values occur for increasing  $\theta$ . This can be understood as a compensatory effect: when signal yields decrease, in order to have background+signal match data, we need to “borrow” some yields from the background nuisance, which pulls up yields at higher number of jets. Of course, there is a likelihood penalty to this due to the  $p(\theta)$  term.

Figure A.3 shows two curves of  $-\ln \mathcal{L}(\mu, \theta)$  for two slices of the scan ( $\mu = \hat{\mu}$ , and  $\mu = 0$ ).

Let’s define the LHC profiled test statistic  $q_\mu$  as

$$q_\mu = q(\mu) = -2 \ln \frac{\mathcal{L}(\mu, \hat{\theta}_\mu)}{\mathcal{L}(\hat{\mu}, \hat{\theta})} \quad (\text{A.4})$$

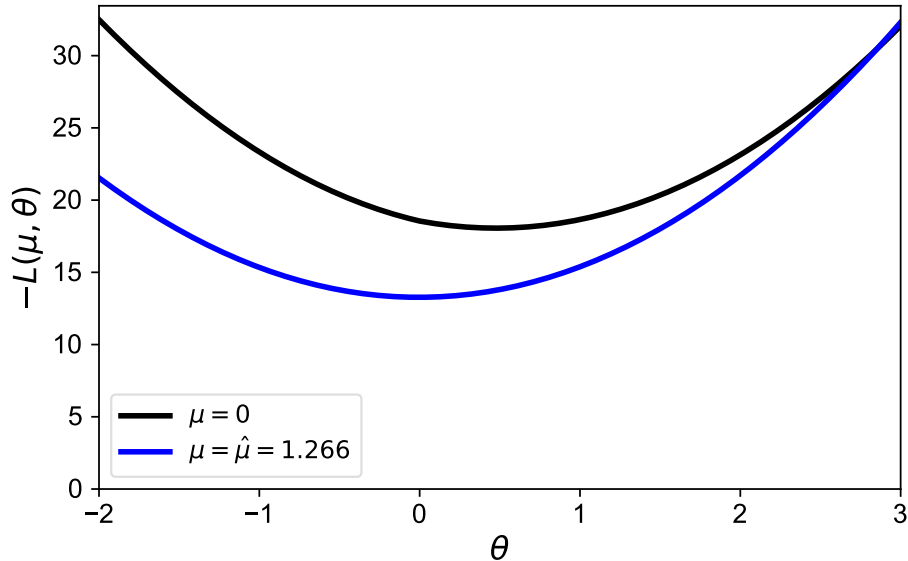


Figure A.3: Negative log likelihood as a function of  $\theta$  for  $\mu$  fixed to 0 and  $\hat{\mu}$

where  $\hat{\theta}_\mu$  is the  $\theta$  that maximizes  $\mathcal{L}$  for a particular  $\mu$ . The pair  $\hat{\mu}$  and  $\hat{\theta}$  are the ones that globally maximize the likelihood. Thus, the denominator is a single number (the global extremum of the 2-dimensional likelihood scan). The numerator is a 1-dimensional function which gives the maximum likelihood as a function of  $\mu$ . We have “profiled out” the nuisance parameter  $\theta$ . Bear in mind the additional minus sign gymnastics we must do when switching between log likelihood and negative log likelihood:

$$q_\mu = 2 \left[ \text{NLL}(\mu, \hat{\theta}_\mu) - \text{NLL}(\hat{\mu}, \hat{\theta}) \right] \quad (\text{A.5})$$

Or,  $q_\mu$  is calculated as twice the difference of the negative log likelihood values along the red curve from the two dimensional scan, and the global minimum negative log likelihood from the same scan. Figure A.4 shows a plot of  $q_\mu = q(\mu)$

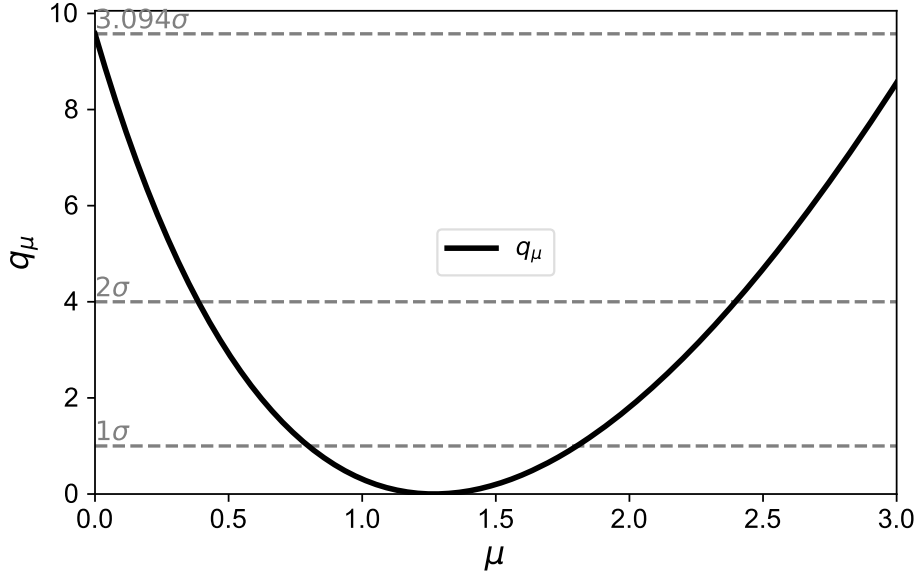


Figure A.4: LHC test statistic as a function of  $\mu$

Before proceeding, we now work with the asymptotic approximation in the case of large background. That is, the test statistic  $q_\mu$  with data containing signal strength  $\mu'$  follows a Gaussian distribution

$$q_\mu = \frac{(\mu - \hat{\mu})^2}{\sigma^2} + \mathcal{O}(1/\sqrt{N}) \quad (\text{A.6})$$

where  $\hat{\mu} \sim \mathcal{N}(\mu', \sigma)$ ,  $N$  is the sample size, and  $\sigma$  is the standard deviation of  $\hat{\mu}$  which is extracted from the covariance matrix of nuisances  $\theta$ . Ultimately, one finds that with this approximation, the test statistic follows a noncentral chi-square distribution for one degree of freedom. See the continuing discussion in Ref. [61]. This is exploited for huge computational gains, especially for SUSY scans which consist of hundreds to a few thousand mass points (number of signal hypotheses to test with the data and background

predictions).

Returning to the curve in Figure A.4, we can identify the significance of the data from one point. That is, how statistically significant would it be if just the background (null hypothesis) fluctuated to look like background+signal:

$$Z_{\text{obs}} = \sqrt{q_0} \quad (\text{A.7})$$

And more generally, we can compute  $1\sigma$ ,  $2\sigma$ ,  $3\sigma$ , etc. confidence bands on the fitted value of  $\hat{\mu}$  by drawing lines at  $q_\mu = 1, 4, 9, \dots$ . Why these values in particular? We turn to a normal distribution with a pdf of

$$f(x|\mu, \sigma) = \frac{1}{\sqrt{2\pi\sigma^2}} e^{-\frac{(x-\mu)^2}{2\sigma^2}} \quad (\text{A.8})$$

Identifying this as a likelihood pdf and ignoring all constant/offset terms independent of  $\sigma$  and  $\mu$ , then

$$q_\mu = -2 \ln(f) = 2 \frac{(x-\mu)^2}{2\sigma^2} \quad (\text{A.9})$$

We want  $x \rightarrow \mu + k \cdot \sigma$  and  $k$  is  $1, 2, 3, \dots$ , so

$$q_\mu \rightarrow \frac{(k\sigma)^2}{\sigma^2} = k^2 \quad (\text{A.10})$$

In this toy example, based on Figure A.4, the observed significance of the result is  $3.09\sigma$  and the fitted signal strength,  $\mu$ , is approximately  $1.3^{+0.4}_{-0.5}$ . For “expected”

quantities, one can consider the **asimov** dataset, which is constructed with background (or signal+background) expectation, incorporating fluctuations due to statistics as well as systematics encoded by the nuisance parameters. This is done to understand analysis results, for example, without looking at the real data.

### A.1.3 Upper limits

For the purposes of setting upper limits on signal strengths, a modified version of Equation A.4 is used as the test statistic:

$$q_\mu = q(\mu) = -2 \ln \frac{\mathcal{L}(\mu, \hat{\theta}_\mu)}{\mathcal{L}(\hat{\mu}, \hat{\theta})} \quad \text{if } \hat{\mu} \leq \mu \quad \text{else} \quad 0 \quad (\text{A.11})$$

This is done so that data where  $\hat{\mu} > \mu$  isn't penalized for representing poorer compatibility with  $\mu$  from actual data. Armed with this modified test statistic, to set upper limits with the CL<sub>s</sub> method [58, 59, 60, 61], we find

$$\text{CL}_s(\mu) = \frac{\text{CL}_{s+b}}{\text{CL}_b} = \frac{p(q_\mu \geq q_\mu^{\text{obs}} | \mu s + b)}{p(q_\mu \geq q_\mu^{\text{obs}} | b)} = \frac{R}{1 - L} \quad (\text{A.12})$$

and scan the quantity over  $\mu$  until  $\text{CL}_s = 5\%$ . The last equality allows the equation to be identified schematically with Figure A.5

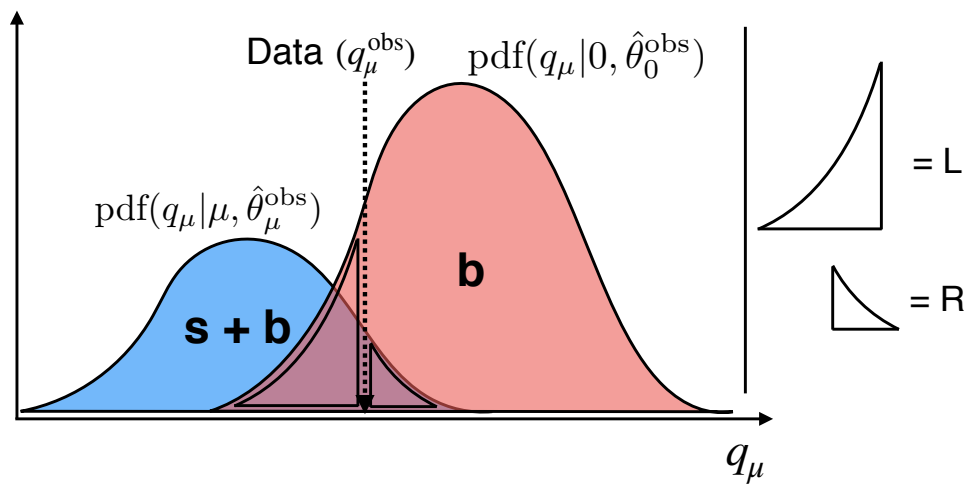


Figure A.5: Schematic diagram illustrating the  $CL_s$  method as described in the text.

# Bibliography

- [1] S. Glashow, *Partial Symmetries of Weak Interactions*, *Nucl. Phys.* **22** (1961) 579–588.
- [2] S. Weinberg, *A Model of Leptons*, *Phys. Rev. Lett.* **19** (1967) 1264–1266.
- [3] A. Salam, *Weak and Electromagnetic Interactions*, *Conf. Proc. C* **680519** (1968) 367–377.
- [4] *Observation of a new particle in the search for the standard model higgs boson with the atlas detector at the lhc*, *Physics Letters B* **716** (2012), no. 1 1 – 29.
- [5] *Observation of a new boson at a mass of 125 gev with the cms experiment at the lhc*, *Physics Letters B* **716** (2012), no. 1 30 – 61.
- [6] <https://www.quantumdiaries.org/2014/03/14/the-standard-model-a-beautiful-but-flawed-theory/>.
- [7] F. Zwicky, *Die Rotverschiebung von extragalaktischen Nebeln*, *Helvetica Physica Acta* **6** (Jan., 1933) 110–127.
- [8] V. Trimble, *Existence and nature of dark matter in the universe.*, .
- [9] S. Hess, F.-S. Kitaura, and S. Gottloeber, *Simulating structure formation of the local universe*, *Monthly Notices of the Royal Astronomical Society* **435** (04, 2013).
- [10] **Super-Kamiokande** Collaboration, Y. Fukuda *et. al.*, *Evidence for oscillation of atmospheric neutrinos*, *Phys. Rev. Lett.* **81** (1998) 1562–1567, [hep-ex/9807003].
- [11] S. P. MARTIN, *A supersymmetry primer*, *Advanced Series on Directions in High Energy Physics* (Jul, 1998) 198.
- [12] R. N. Mohapatra, *Supersymmetry and r-parity: an overview*, 2015.
- [13] L. R. Evans and P. Bryant, *LHC Machine*, *JINST* **3** (2008) S08001. 164 p. This report is an abridged version of the LHC Design Report (CERN-2004-003).
- [14] **CMS** Collaboration, S. Chatrchyan *et. al.*, *The CMS experiment at the CERN LHC*, *JINST* **3** (2008) S08004.

- [15] CMS Collaboration, *CMS technical design report, volume II: Physics performance*, *J. Phys. G* **34** (2007) 995.
- [16] CMS Collaboration, S. Chatrchyan *et. al.*, *Description and performance of track and primary-vertex reconstruction with the CMS tracker*, *JINST* **9** (2014) P10009, [arXiv:1405.6569].
- [17] A. Dominguez, D. Abbaneo, K. Arndt, N. Bacchetta, A. Ball, E. Bartz, W. Bertl, G. M. Bilei, G. Bolla, H. W. K. Cheung, M. Chertok, S. Costa, N. Demaria, D. D. Vazquez, K. Ecklund, W. Erdmann, K. Gill, G. Hall, K. Harder, F. Hartmann, R. Horisberger, W. Johns, H. C. Kaestli, K. Klein, D. Kotlinski, S. Kwan, M. Pesaresi, H. Postema, T. Rohe, C. Schfer, A. Starodumov, S. Streuli, A. Tricomi, P. Tropea, J. Troska, F. Vasey, and W. Zeuner, *CMS Technical Design Report for the Pixel Detector Upgrade*, Tech. Rep. CERN-LHCC-2012-016. CMS-TDR-11, Sep, 2012. Additional contacts: Jeffrey Spalding, Fermilab, Jeffrey.Spalding@cern.ch Didier Contardo, Universite Claude Bernard-Lyon I, didier.claude.contardo@cern.ch.
- [18] CMS Collaboration, V. Khachatryan *et. al.*, *Performance of electron reconstruction and selection with the CMS detector in proton-proton collisions at  $\sqrt{s} = 8 \text{ TeV}$* , *JINST* **10** (2015) P06005, [arXiv:1502.0270].
- [19] CMS Collaboration, A. M. Sirunyan *et. al.*, *Performance of the CMS muon detector and muon reconstruction with proton-proton collisions at  $\sqrt{s} = 13 \text{ TeV}$* , *JINST* **13** (2018) P06015, [arXiv:1804.0452].
- [20] CMS Collaboration, V. Khachatryan *et. al.*, *The CMS trigger system*, *JINST* **12** (2017) P01020, [arXiv:1609.0236].
- [21] CMS Collaboration, A. M. Sirunyan *et. al.*, *Particle-flow reconstruction and global event description with the CMS detector*, *JINST* **12** (2017) P10003, [arXiv:1706.0496].
- [22] CMS Collaboration, A. M. Sirunyan *et. al.*, *Search for production of four top quarks in final states with same-sign or multiple leptons in proton-proton collisions at  $\sqrt{s} = 13 \text{ TeV}$* , *Eur. Phys. J. C* **80** (2020), no. 2 75, [arXiv:1908.0646].
- [23] CMS Collaboration, *Search for physics beyond the standard model in events with two same-sign leptons or at least three leptons and jets in proton-proton collisions at  $\sqrt{s} = 13 \text{ TeV}$ .*, *Eur. Phys. J. C* **80** (2020), no. 8 752, [arXiv:2001.1008].
- [24] CMS Collaboration, *Search for standard model production of four top quarks with same-sign and multilepton final states in proton-proton collisions at  $\sqrt{s} = 13 \text{ TeV}$* , *Eur. Phys. J. C* **78** (2018), no. 2 140, [arXiv:1710.1061].

- [25] CMS Collaboration, *Search for physics beyond the standard model in events with two leptons of same sign, missing transverse momentum, and jets in proton-proton collisions at  $\sqrt{s} = 13$  TeV*, *Eur. Phys. J.* **C77** (2017), no. 9 578, [arXiv:1704.0732].
- [26] <https://twiki.cern.ch/twiki/bin/view/CMSPublic/PhysicsResultsCombined>.
- [27] <https://twiki.cern.ch/twiki/bin/view/LHCPhysics/SUSYCrossSections>.
- [28] R. Frederix, D. Pagani, and M. Zaro, *Large NLO corrections in  $t\bar{t}W^\pm$  and  $t\bar{t}t\bar{t}$  hadroproduction from supposedly subleading EW contributions*, *JHEP* **02** (2018) 031, [arXiv:1711.0211].
- [29] G. C. Branco, P. M. Ferreira, L. Lavoura, M. N. Rebelo, M. Sher, and J. P. Silva, *Theory and phenomenology of two-Higgs-doublet models*, *Phys. Rept.* **516** (2012) 1–102, [arXiv:1106.0034].
- [30] K. J. F. Gaemers and F. Hoogeveen, *Higgs Production and Decay Into Heavy Flavors With the Gluon Fusion Mechanism*, *Phys. Lett.* **B146** (1984) 347–349.
- [31] D. Dicus, A. Stange, and S. Willenbrock, *Higgs decay to top quarks at hadron colliders*, *Phys. Lett. B* **333** (1994) 126, [hep-ph/9404359].
- [32] N. Craig, F. D’Eramo, P. Draper, S. Thomas, and H. Zhang, *The hunt for the rest of the Higgs bosons*, *JHEP* **06** (2015) 137, [arXiv:1504.0463].
- [33] N. Craig, J. Hajar, Y.-Y. Li, T. Liu, and H. Zhang, *Heavy Higgs bosons at low  $\tan\beta$ : from the LHC to 100 TeV*, *JHEP* **01** (2017) 018, [arXiv:1605.0874].
- [34] D. Pinna, A. Zucchetta, M. R. Buckley, and F. Canelli, *Single top quarks and dark matter*, *Phys. Rev. D* **96** (Aug, 2017) 035031.
- [35] CMS Collaboration, A. M. Sirunyan *et. al.*, *Search for dark matter produced in association with a single top quark or a top quark pair in proton-proton collisions at  $\sqrt{s} = 13$  TeV*, *JHEP* **03** (2019) 141, [arXiv:1901.0155].
- [36] CMS Collaboration, C. Collaboration, *Search for Dark Matter Particles Produced in Association with a Top Quark Pair at  $\sqrt{s}=13$  TeV*, *Phys. Rev. Lett.* **122** (Jan, 2019) 011803.
- [37] Q.-H. Cao, S.-L. Chen, and Y. Liu, *Probing Higgs width and top quark Yukawa coupling from  $t\bar{t}H$  and  $t\bar{t}t\bar{t}$  productions*, *Phys. Rev. D* **95** (2017) 053004, [arXiv:1602.0193].
- [38] E. Alvarez, D. A. Faroughy, J. F. Kamenik, R. Morales, and A. Szynkman, *Four tops for LHC*, *Nucl. Phys. B* **915** (2017) 19, [arXiv:1611.0503].

- [39] C. Englert, G. F. Giudice, A. Greljo, and M. Mccullough, “The  $\hat{H}$ -parameter: an oblique Higgs view.” 2019.
- [40] J. Alwall, R. Frederix, S. Frixione, V. Hirschi, F. Maltoni, O. Mattelaer, H. S. Shao, T. Stelzer, P. Torrielli, and M. Zaro, *The automated computation of tree-level and next-to-leading order differential cross sections, and their matching to parton shower simulations*, *JHEP* **07** (2014) 079, [arXiv:1405.0301].
- [41] M. Cacciari, G. P. Salam, and G. Soyez, *The anti- $k_t$  jet clustering algorithm*, *JHEP* **04** (2008) 063, [arXiv:0802.1189].
- [42] M. Cacciari, G. P. Salam, and G. Soyez, *FastJet user manual*, *Eur. Phys. J. C* **72** (2012) 1896, [arXiv:1111.6097].
- [43] CMS Collaboration, V. Khachatryan *et. al.*, *Jet energy scale and resolution in the CMS experiment in pp collisions at 8 TeV*, *JINST* **12** (2016) P02014, [arXiv:1607.0366].
- [44] CMS Collaboration, *Jet algorithms performance in 13 TeV data*, CMS Physics Analysis Summary CMS-PAS-JME-16-003, 2017.
- [45] CMS Collaboration, A. M. Sirunyan *et. al.*, *Identification of heavy-flavour jets with the CMS detector in pp collisions at 13 TeV*, *JINST* **13** (2018) P05011, [arXiv:1712.0715].
- [46] <https://twiki.cern.ch/twiki/bin/viewauth/CMS/BtagRecommendation>.
- [47] CMS Collaboration, A. M. Sirunyan *et. al.*, *Performance of missing transverse momentum reconstruction in proton-proton collisions at  $\sqrt{s} = 13$  TeV using the CMS detector*, *JINST* **14** (2019) P07004, [arXiv:1903.0607].
- [48] <https://twiki.cern.ch/twiki/bin/view/CMS/MissingETOptionalFilters>.
- [49] CMS Collaboration, A. M. Sirunyan *et. al.*, *Performance of the reconstruction and identification of high-momentum muons in proton-proton collisions at  $\sqrt{s} = 13$  TeV*, *JINST* **15** (2020) P02027, [arXiv:1912.0351].
- [50] Baffioni, S. and others, *Electron Charge Identification using 8 TeV data*, *CMS Physics Analysis Note AN-2014/164* (2015).
- [51] <https://twiki.cern.ch/twiki/bin/view/CMS/SUSLeptonSF>.
- [52] T. Chen and C. Guestrin, *Xgboost*, *Proceedings of the 22nd ACM SIGKDD International Conference on Knowledge Discovery and Data Mining* (Aug, 2016).
- [53] CMS Collaboration, A. M. Sirunyan *et. al.*, *Measurement of the cross section for top quark pair production in association with a W or Z boson in proton-proton collisions at  $\sqrt{s} = 13$  TeV*, *JHEP* **08** (2018) 011, [arXiv:1711.0254].

- [54] CMS Collaboration, A. M. Sirunyan *et. al.*, *Observation of  $t\bar{t}H$  production*, *Phys. Rev. Lett.* **120** (2018) 231801, [arXiv:1804.0261].
- [55] CMS SUSY fake-leptons working group, *Studies of methods to estimate the non-prompt lepton background to searches for new physics*, *CMS Physics Analysis Note AN-2014/261* (2015).
- [56] CMS Collaboration, A. M. Sirunyan *et. al.*, *Measurements of  $t\bar{t}$  cross sections in association with  $b$  jets and inclusive jets and their ratio using dilepton final states in  $pp$  collisions at  $\sqrt{s} = 13$  TeV*, *Phys. Lett. B* **776** (2018) 355, [arXiv:1705.1014].
- [57] M. Franco Sevilla and A. Ovcharova, *Isr reweighting recommendations for moriond 2017*, December, 2016.  
[https://indico.cern.ch/event/592621/contributions/2398559/attachments/1383909/2105089/16-12-05\\_ana\\_manuelf\\_isr.pdf](https://indico.cern.ch/event/592621/contributions/2398559/attachments/1383909/2105089/16-12-05_ana_manuelf_isr.pdf).
- [58] T. Junk, *Confidence level computation for combining searches with small statistics*, *Nucl. Instrum. Meth. A* **434** (1999) 435, [hep-ex/9902006].
- [59] A. L. Read, *Presentation of search results: the  $CL_s$  technique*, *J. Phys. G* **28** (2002) 2693.
- [60] ATLAS and CMS Collaborations, *Procedure for the LHC Higgs boson search combination in summer 2011*, ATL-PHYS-PUB-2011-011, CMS NOTE-2011/005, 2011.
- [61] G. Cowan, K. Cranmer, E. Gross, and O. Vitells, *Asymptotic formulae for likelihood-based tests of new physics*, *Eur. Phys. J. C* **71** (2011) 1554, [arXiv:1007.1727]. [Erratum: Eur. Phys. J.C73,2501(2013)].
- [62] ATLAS Collaboration, M. Aaboud *et. al.*, *Measurement of the  $t\bar{t}Z$  and  $t\bar{t}W$  cross sections in proton-proton collisions at  $\sqrt{s} = 13$  TeV with the ATLAS detector*, *Phys. Rev. D* **99** (2019) 072009, [arXiv:1901.0358].
- [63] CMS Collaboration, A. M. Sirunyan *et. al.*, *Measurement of the cross section for top quark pair production in association with a  $W$  or  $Z$  boson in proton-proton collisions at  $\sqrt{s} = 13$  TeV*, *JHEP* **08** (2018) 011, [arXiv:1711.0254].
- [64] CMS Collaboration, A. M. Sirunyan *et. al.*, *Search for supersymmetry in events with at least three electrons or muons, jets, and missing transverse momentum in proton-proton collisions at  $\sqrt{s} = 13$  TeV*, *JHEP* **02** (2018) 067, [arXiv:1710.0915].
- [65] CMS Collaboration, A. M. Sirunyan *et. al.*, *Search for supersymmetry in  $pp$  collisions at  $\sqrt{s} = 13$  TeV with  $137 \text{ fb}^{-1}$  in final states with a single lepton using the sum of masses of large-radius jets*, *Phys. Rev. D* **101** (2020), no. 5 052010, [arXiv:1911.0755].

- [66] **CMS** Collaboration, A. M. Sirunyan *et. al.*, *Search for supersymmetry in proton-proton collisions at 13 TeV in final states with jets and missing transverse momentum*, *JHEP* **10** (2019) 244, [arXiv:1908.0472].
- [67] **CMS** Collaboration, A. M. Sirunyan *et. al.*, *Searches for physics beyond the standard model with the  $M_{T2}$  variable in hadronic final states with and without disappearing tracks in proton-proton collisions at  $\sqrt{s} = 13$  TeV*, *Eur. Phys. J. C* **80** (2020), no. 1 3, [arXiv:1909.0346].
- [68] **CMS** Collaboration, A. M. Sirunyan *et. al.*, *Search for R-parity violating supersymmetry in pp collisions at  $\sqrt{s} = 13$  TeV using b jets in a final state with a single lepton, many jets, and high sum of large-radius jet masses*, *Phys. Lett. B* **783** (2018) 114, [arXiv:1712.0892].
- [69] Particle Data Group, C. Patrignani, *et. al.*, *Review of Particle Physics*, *Chin. Phys. C* **40** (2016) 100001.
- [70] **ATLAS** Collaboration, M. Aaboud *et. al.*, *Measurement of the  $t\bar{t}Z$  and  $t\bar{t}W$  cross sections in proton-proton collisions at  $\sqrt{s} = 13$  TeV with the ATLAS detector*, *Phys. Rev. D* **99** (2019) 072009, [arXiv:1901.0358].
- [71] **CMS** Collaboration, A. M. Sirunyan *et. al.*, *Measurement of top quark pair production in association with a Z boson in proton-proton collisions at  $\sqrt{s} = 13$  TeV*, *JHEP* **03** (2020) 056, [arXiv:1907.1127].
- [72] ATLAS and CMS Collaborations, *Measurements of the Higgs boson production and decay rates and constraints on its couplings from a combined ATLAS and CMS analysis of the LHC pp collision data at  $\sqrt{s} = 7$  and 8 TeV*, *JHEP* **08** (2016) 045, [arXiv:1606.0226].
- [73] **CMS** Collaboration, A. M. Sirunyan *et. al.*, “Search for heavy Higgs bosons decaying to a top quark pair in proton-proton collisions at  $\sqrt{s} = 13$  TeV.” Submitted to JHEP, 2019.
- [74] **ATLAS** Collaboration, M. Aaboud *et. al.*, *Search for dark matter produced in association with bottom or top quarks in  $\sqrt{s} = 13$  TeV pp collisions with the ATLAS detector*, *Eur. Phys. J. C* **78** (2018) 18, [arXiv:1710.1141].